# Deformation of sandstones under cyclic loading

## Relevant for underground energy storage

E. Hernandez

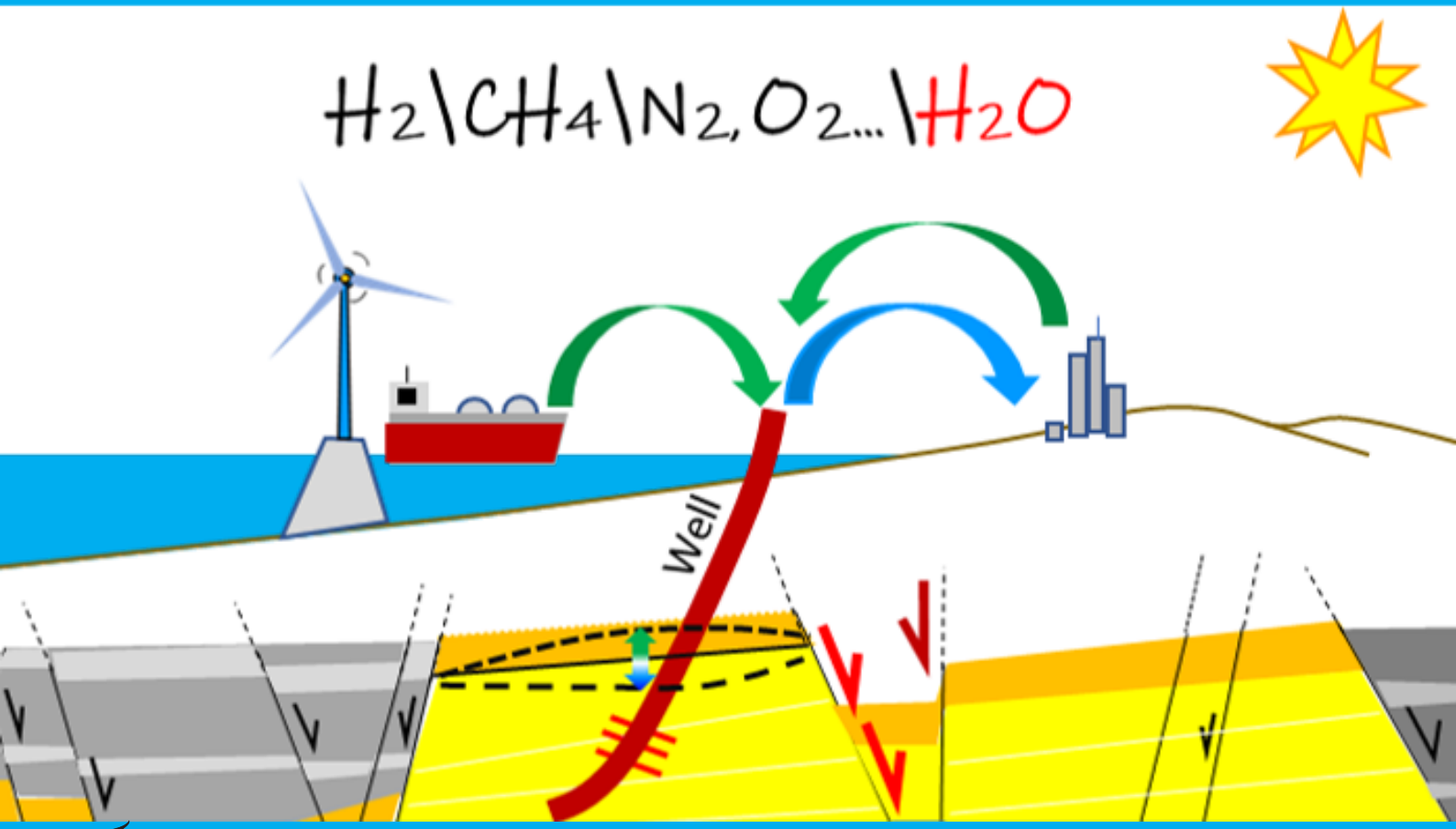


TU Delft

# Deformation of sandstones under cyclic loading

## Relevant for underground energy storage

by

E. Hernandez

to obtain the degree of Master Applied Earth Sciences
at the Delft University of Technology,
to be defended publicly on Friday August 29, 2022 at 10:00 AM.


| | | |
|---|---|---|
| Student number: | 5391377 | |
| Project duration: | November 4, 2021 – August 29, 2022 | |
| Thesis committee: | Dr. H. Hajibeygi | TU Delft, supervisor |
| | Dr. A. Barnhoorn | TU Delft, supervisor |
| | Ir. K. Ramesh Kumar | TU Delft, co-supervisor |
| | M. Naderloo | TU Delft, co-supervisor |
| | Dr. S. Geiger | TU Delft |




TU Delft

# Abstract

Underground energy storage (UES) in porous and cavity reservoirs can be used to balance the mismatch between the production and demand of renewable energy, as well as for securing gas and oil supply during shortage or high demand periods. Understanding the geomechanical behavior of these reservoirs under different storage conditions, i.e., storage frequency and fluid pressure, is key in defining their capacity and effective lifetime. This thesis work presents a rigorous analysis performed on sandstones to unravel their geomechanical response under cyclic loading. This study includes, importantly, both experimental and numerical investigations under several conditions which are relevant to UES. The rock response was studied considering cyclic stress states above and below the onset of dilatant cracking, under different frequencies and amplitudes. Within the number of cycles studied, measurements of axial strains and acoustic emissions indicated that inelastic strains accumulated cycle after cycle following an exponentially decreasing rate. Five types of deformations were interpreted: elastic, plastic, viscoelastic, cyclic-plastic and brittle creep. Based on these novel experimental results and observations, Nishihara's constitutive model was used for simulating viscoelastic and brittle creep deformations, while dilatant plastic strains were modeled using a Hardening-Softening model. Finally, an extension of the Modified Cam-Clay model was proposed to account for cyclic-plastic compaction. This approach can be extended and improved to study cyclic sandstone deformation's implications on subsidence, fault reactivation and cap rock flexure, among other physical phenomena impacting a reservoir's storage capacity.

# Acknowledgements

*My journey back to academia has come to an end with the conclusion of this thesis. It was a very fruitful experience of friendship and knowledge. I would like to thanks my supervisors Hadi and Auke for their support, guidance and freedom given.*

*I also want to thank my co-supervisors Milad and Kishan for their advice, corrections, time, and great conversations. I really enjoyed the time in the lab with Marc as well as listening Anne's insightful comments. Also thanks to the extended PrESCO team and all my friends from the MSc class of entering 2020.*

*Last but not least, I want to thank Anais and Andrea for their support, understanding and time sacrificed, as well as my parents Edgar and Neira and all my family who supported me from a distance.*

*Delft/Paris, August 2022*

*E. Hernandez*

# List of Figures

# List of Tables

# Contents

# 1

# Overview

## 1.1. Problem statement

Society has realized since its beginning that storage of water, energy or other fundamental resources is required to face periods of shortage and/or high demands. This is because storage offers a medium to stabilize systems that are intermittent in nature (Mahmoud et al., 2021). For example, in the energy context and before the advent of fossil fuels, people living in temperate climate regions used to log trees during the summer to have dry wood for heating during the winter. Nowadays, it has partially evolved to the use of a technology called underground gas storage “UGS” (Tek, 1987), where imported gas is stored in subsurface reservoirs during the summer, when prices and demand are low, for heating during winter. Consequently, it can be seen that energy storage plays an important role in the development of our societies. In fact, it is currently relevant, due to the rising global population, economic growth, the breakthrough of electric vehicles, climate change, depletion of fossil fuels and the emergence of renewable energy resources.

There are different mechanisms to store energy (electric, thermal) or energy-rich fluids (hydrocarbons, hydrogen, hot water). These mechanisms include mechanical, which are based on pumping, compression, expansion and acceleration (kinetic and potential energy), chemical and electrochemical, which uses reversible chemical reactions, thermal (relies on thermodynamic changes and material heat capacities) and finally those that exploit electric potential energy through the creation of electric and magnetic fields (Gallo et al., 2016 and Matos et al., 2018). Of interest to the geoscience area are those applications related mainly with mechanical and thermal mechanisms such as compressed air energy storage “CAES”, underground gas and hydrogen storage “UGS”/“UHS”, and aquifer thermal energy storage “ATES” (Allen et al., 1983,Tek, 1987, Heinemann et al., 2021, Kabuth et al., 2017, Matos et al., 2018). All these applications are based on the injection of energy-rich fluids in underground reservoirs (porous-permeable rocks, salt caverns and abandoned mines) that will be produced back when the

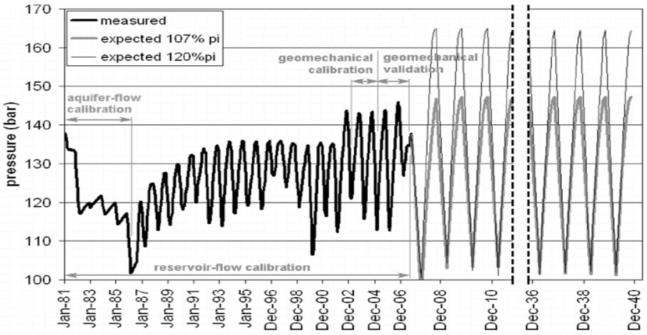


Figure 1.1: Pore pressure during depletion (1981 - 1986), gas storage (1987 - 2006) and future storage scenarios to increase capacity (2006 - 2040) in a depleted hydrocarbon reservoir (from Teatini et al., 2011 under AGU permissions policy).

market needs them. As a consequence of this injection and production scheme, the resulting fluid pressure condition in the underground reservoir is cyclic, as shown in figure 1.1. For porous storage systems, these porous pressure fluctuations induce cyclic changes in the normal effective stresses of the reservoir rock, i.e. 'cyclic loading conditions'. These loading conditions do not only affect the deformation of the reservoir rock but also the surrounding elements, such as caprock, faults and wells. On top of that, the reservoir could experience cyclic changes in temperature, fluid composition, rock composition and biota due to this injection-production cyclic scheme (Heinemann et al., 2021).

The underground storage capacity is directly proportional to the fluid pressure. Thus, a question arises: Are there limits for the induced pressure fluctuations in order to safely store fluids? This question can be scientifically answered by looking at the elements that form the underground energy storage "UES" and its response to the pressure fluctuations. For instance, the reservoir rock (storage medium) and cap rock (sealing medium) around the wells, can be fractured by tension if excessive pressure is applied during injection, which could lead to fluid leakage. Therefore, the fracture rock pressure defines a maximum possible limit for pressure fluctuations during storage. In addition, these fluctuations can induce subsidence and uplifting as shown in figure 1.2, which could be severe depending on its magnitude and spatial gradient. Furthermore, this decrease or increase in pore pressure can also induce fault reactivation if the corresponding stress path on the fault plane intersects the failure envelope (Orlic et al., 2013, Silverii et al., 2021). This intersection point, known as threshold pressure, defines the limit to avoid fault reactivation and possible seismic events, which are possible consequences during UES.

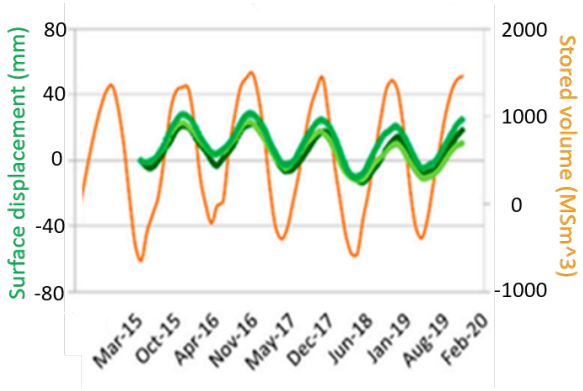


Figure 1.2: Uplifting and subsidence at 3 different spatial positions (green curves) as a response to gas storage volumes (orange) in an Italian depleted gas reservoir. Figure edited from Benetatos et al., 2020 under MDPI permission terms.

Thus, there are pressure limits during underground energy storage. These limits are expected to remain constant over time and over the number of storage cycles if the rock behaves elastic. Nevertheless, rocks under cyclic loading can experience accumulation of inelastic deformations cycle after cycle (Cerfontaine and Collin, 2018) that could affect the stress paths in the reservoir, caprock, fault planes and near welbore area (Haghighat et al., 2020). Therefore, pressure limits could change as the number of storage cycles increases. On top of that, inelastic strains can affect compaction and subsidence. In fact, it has been documented in field storage applications that subsidence has not been totally recovered during underground gas storage (N.A.M., 2016, Fenix-Consulting-Delft-BV, 2018), which is an indication of inelastic strains. This behavior has been associated with reservoir inelastic compaction (Allen et al., 1983,Benetatos et al., 2020,Heinemann et al., 2021 and Pijnenburg et al., 2018).

Based on what came above, the study of inelastic deformations generated under cyclic loading conditions in sandstone reservoirs is of interest for underground energy storage. Nevertheless, most of the studies in the literature have been performed in the framework of high-stress amplitude and high-frequency applications related with civil works (piles installation), mining and drilling. These studies are generally focused on rock fatigue (failure of rock at stresses below the peak rock strength after a certain number of cycles) and instantaneous deformations as mentioned by Burdine, 1963, Wichtmann, 2005 and Cerfontaine et al., 2017,Cerfontaine and Collin, 2018). Nevertheless, there are few studies intended to understand and model low-frequency deformation cyclic loading in sandstones (< 0.1 Hz

after Liu and Dai, 2021), which is relevant for UES. For instance, Gatelier et al., 2002 identified that depending on the stress level with respect to the onset of dilatant cracking, compaction and microcracking are the mechanisms in sandstones under damage cyclic loading conditions. Dietl et al., 2019 performed tests at a frequency of 7E-5 Hz and constant pore pressure amplitudes on sandstone samples. It was found that the sandstone did not experience fatigue within the number of studied cycles. Nevertheless, the strain results showed that time-dependent volumetric inelastic strains took place.

Regarding modeling, instantaneous cyclic-plastic brittle deformations have been modeled using constitutive models based on boundary surface concept, like the one developed by Cerfontaine et al., 2017 and Vermeer and de Borst, 1984. On the other hand, time-dependent deformations in sandstones have been modeled with power-law creep models as shown by Kumar and Hajibeygi, 2021. This creep model has also been used to model low-frequency cyclic loading on shales (Rassouli and Zoback, 2015). Rheological models like the Nishihara's constitutive model that considered elastic, viscoelastic and creep deformations were used to model long-term stress stepping tests in sandstones (X. Wang et al., 2018, X. Li and Yin, 2021). A detailed description of modeling approaches for rocks under cyclic loading can be found in the work of LI et al., 2021. Nevertheless, integrated models that take into account both instantaneous and time-dependent elastic and inelastic deformations during cyclic loading are not that common. It was found one proposal by Haghighat et al., 2020 that combines the Modified Cam-clay model and Perzyna-type model to account for plasticity and creep in shales. A combination of models could be an approach to model low-frequency cyclic loading of sandstones where both instantaneous and time-dependent deformations are important.

This thesis aims to explore experimentally and theoretically the effects of low frequencies cyclic loading on sandstone deformation. These effects are tested under stress conditions above and below the onset of dilatant cracking (brittle yield point). It is expected that the results obtained in this thesis could be used in future projects to understand the impact of cyclic loading on fluid pressure limits, storage capacity and the life span of underground energy storage facilities.

## 1.2. Research questions

- What is the current research status of cyclic loading studies on underground energy storage elements?
- What deformation mechanisms could be present during cyclic loading of sandstone reservoirs: elastic, inelastic, instantaneous or time-dependent?
- Do frequency, amplitude and mean stress affect the deformation during cyclic loading?
- How could cyclic deformation be modeled?
- What are the possible implications of cyclic loading on underground energy storage applications?

## 1.3. Project goals

- Perform an extensive literature review on cyclic loading in rocks to define the current experimental research status on: the storage reservoir's elements, type of tests, deformation mechanism, properties behavior and field experiences
- Design, plan and execute a test program for cyclic loading on sandstone samples, able to measure axial strains at different amplitudes, mean stresses and frequencies
- Identify pertinent constitutive models and evaluate them against experimental data
- Analyze the possible implications of cyclic loading on underground energy storage in sandstone reservoirs based on the measured experimental data, modeling results and referential information

## 1.4. Scope

For the execution of this master's thesis, it was planned to use a triaxial loading machine and a triaxial cell equipped with acoustic sensors, located at the Faculty of CiTG, TUDELFT. This machine

allows to measured axial strain and acoustic emissions. Lateral strains cannot be recorded. The selected sandstone was the Red Felser, which can be considered an analog in lithology and time of deposition to reservoir sandstones used for gas storage in The Netherlands (Slochteren sandstone). The maximum duration of a test was defined to be one business day because the operator must be present during the execution of the tests. In these tests, the effect of cyclic frequency, amplitude, and mean stress were considered. The experimental results were used to determine pertinent constitutive models for modeling cyclic loading of sandstones. The experiments were scheduled for a period of up to 4 months while modeling was defined to take place for 3 months.

## 1.5. Structure of the thesis report

The second chapter ”Literature review” is dedicated to the analysis of previous studies about cyclic loading on the underground reservoir’s elements. It defines what elements have been studied more and which less, what type of tests has been performed, what objective has been pursued and what results have been found. This analysis always establishes links with underground energy storage.

The third chapter ”Theoretical basis” describes the basic concepts needed to perform the research from both experimental and theoretical points of view.

The fourth chapter ”Cyclic loading experiments” describes the test program and results regarding axial elastic and inelastic deformations and acoustic under different frequencies, amplitudes and mean stress of the imposed loading waveform.
The fifth chapter ”Modeling of cyclic loading experiments” looks for defining the pertinent constitutive models for reproducing test results.

The sixth chapter analyses the possible implication of induced cyclic loading deformation on underground energy storage operations.

# 2

# Literature review on cyclic loading

In order to determine the current experimental/theoretical research status on cyclic loading relevant to underground energy storage, a database was created and analyzed. The database can be seen in appendix A. This includes information about the type of rock, cyclic loading test type and objective that was used for the analysis. It is important to mention that more publications and reports could be available but it is expected that the result of the analysis can provide a trend of the current research.

### 2.0.1. Cyclic loading

Cyclic loading of materials, which consists of the application of time-dependent repetitive stress conditions on objects, is a subject of interest in different applications. Figure 2.1 shows that the cyclic loading phenomena range from high-frequency oscillation of aircraft wings and highways to low- and ultra-low-frequency situations, such as underground energy storage and glacial to inter-glacial cycles. Under these cyclic conditions, it is of interest to understand the material behavior in terms of strength, material properties and stress redistribution as loading conditions are applied in a wave fashion over time.

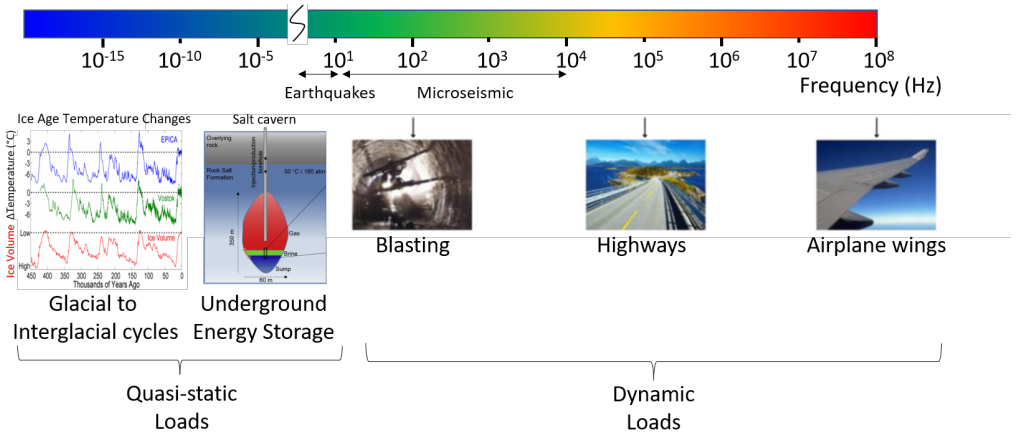


Figure 2.1: Examples of application under different cyclic loading frequencies (modified from Liu and Dai, 2021, Hemme and van Berk, 2017 and Rohde, n.d. Figures used under Creative Commons CC-BY-NC-ND 4.0 license and Creative Commons CC-BY-SA 3.0 license).

Cyclic loading can be divided into quasi-static and dynamic loading according to the applied frequency (Wichtmann, 2005). Dynamic cyclic loading (frequency > 5Hz) refers to the existence of inertial forces comparable with the applied forces during the cyclic process (the reversal of displacement is not instantaneous at the moment the load is changed). Quasi-static cyclic loading (frequency $\leq$ 5Hz) indicates that inertial forces can be ignored because there is sufficient time for the material to recover its shape and follow instantaneously the change in displacement direction. Thus, cyclic loading caused

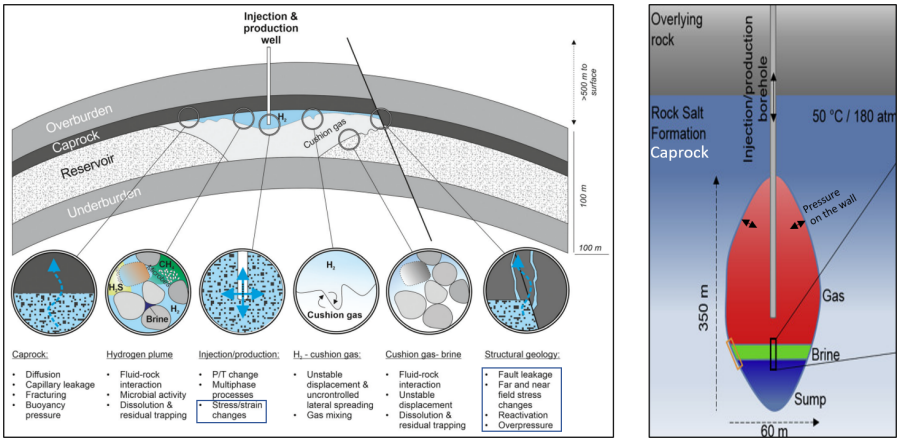


Figure 2.2: Elements of an underground hydrogen porous storage reservoir from Heinemann et al., 2021 (left) and the corresponding elements of a salt cavern storage system from Hemme and van Berk, 2017 (right). Figures used under Creative Commons CC-BY-NC 3.0 license and Creative Commons CC-BY-NC-ND 4.0 license.

by injection-production cycles in UES can be considered quasi-static loading. Next, it is presented a brief analysis of the studies reported in the literature about cyclic loading on the elements conforming the underground energy storage reservoir. For a detailed discussion of cyclic loading in rocks and soils please refer to the next authors: Cerfontaine and Collin, 2018, Liu and Dai, 2021 and Wichtmann, 2005.

### 2.0.2. Elements of the underground energy storage reservoir affected by cyclic loading

Energy-rich fluids (Hydrogen, Methane, Compressed Air, Hot Water) can be stored in underground reservoirs like porous rocks, abandoned mines and salt caverns (excluding Hot Water). In addition to a sufficient continuous volume, these reservoirs must be vertically bounded by sealing formations and have wells with sufficient rock transmissibility to allow the injection and production of the energy-rich fluids, among other conditions.

Thus, for storage in porous rocks (depleted hydrocarbon reservoirs or aquifers), a reservoir trap (structural or stratigraphical) is required to store and contain the energy-rich fluids as shown in figure 2.2. Nevertheless, this is not mandatory for aquifer thermal energy storage 'ATES' applications, where the most important condition is aquifer low velocity (to minimize heat losses by advection). The main elements of porous reservoirs affected by pressure changes during storage operations are:

· **The reservoir rock:** usually permeable sandstones and carbonates.

· **The caprock:** usually ultra-low permeability shales and evaporites but also igneous and metamorphic rocks like Dolerite and Marble could be caprock, as the system found at Native Hydrogen reservoir in Mali Prinzhofer et al., 2018.

· **The faults:** regularly normal or inverse faults. The Damage zone (ensemble of fractures) of the fault can also experience pressure changes.

· **The well:** this includes the reservoir near wellbore region, cement sheath and casing/liners.

During storage, these elements are exposed to cyclic loading. Thus, their response to this type of loading is of interest for design of underground energy storage systems. It is important to mention that in the case of salt caverns, there is not reservoir rock but a leached cavity and the faults are not common, because the deformation in rock salts is accommodated mainly in a ductile way.

### 2.0.3. Experimental studies on underground energy storage elements

The elements of the underground energy storage system have been studied since the '60s (Burdine, 1963). Nevertheless, this does not mean that the studies were intended for underground energy

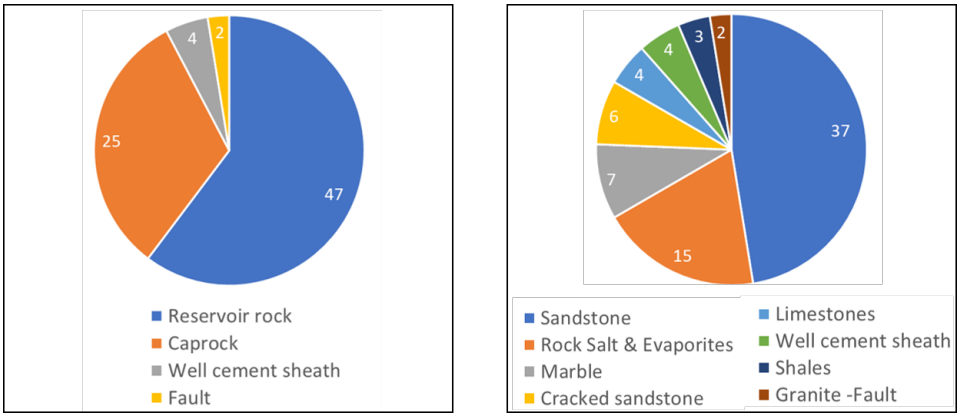


Figure 2.3: Cyclic loading tests publications by reservoir's elements (left) and by lithology (right) of underground energy storage systems after analysis of databases from Cerfontaine and Collin, 2018, Liu and Dai, 2021 and this thesis.

storage "UES". Only recently, experimental studies have been motivated by UES, most of them being related to storage in salt caverns. Figure 2.3-left shows the number of publications and reports found for each element of the underground energy storage system. On one hand, It can be seen that most of the experimental studies have been carried out on reservoir rocks, sandstone being the most studied, as shown in figure 2.3-right. Nevertheless, only five of these studies are motivated by UES (Dietl et al., 2019, K. de-Kloe, 2008, LI et al., 2021, H. L. Wang et al., 2017 and Le et al., 2014). The remaining publications are mainly related with mining (for exampleTaheri et al., 2016 and Peng et al., 2019a), well drilling (Burdine, 1963),civil works (Wichtmann, 2005) and studies on the fundamental mechanisms that lead to fatigue (Burdine, 1963 and Taheri et al., 2016). On the other hand, the faults are apparently the element less studied, with only two publications found (Ji, Zhuang, et al., 2021,Ji, Yoon, et al., 2021). Nevertheless, interest in cyclic loading in faults could soar if cyclic water injection proves to be positive in mitigating seismic risks during fracking operations (Ji, Zhuang, et al., 2021).

In addition, it is also shown in figure 2.3-left, that the caprock is the second most studied element. Within the caprocks, the rock salt has been the most studied (2.3-right). Contrary to sandstones, these studies are motivated by underground energy storage in salt caverns (Fuenkajorn and Phueakphum, 2010, Bauer et al., 2010, Liang et al., 2012 and Ma et al., 2013a). Marbles, which can also work as caprock, have been also studied, while the least studied caprock is the shale, even though this rock is the most common seal in sedimentary basins.

Regarding the wells, well cement sheath, used to avoid the fluid leakage behind the casing, has been studied (Shadravan et al., 2015, He et al., 2021 and J. Li et al., 2021). In fact, it is probably one of the elements most prone to fatigue (rock failure below the static rock strength due to cyclic loading) in a relatively small number of cycles as shown by Shadravan et al., 2015. On the positive side, the cement slurry formulation can be tuned to improve its fatigue strength.

### 2.0.4. Methods to induce cyclic loading during experiments

There are two options to induce cyclic loading on rocks:

· **External cyclic loading:** It consists of applying external cyclic stress (tension, compression and shear) on the rock sample as shown in figure 2.4-left. Here, $S_1$ and $S_3$ are the maximum and minimum principal total stresses respectively.

· **Pore pressure cycles:** In this method at least one external stress is held constant and the pore pressure '$P_p$' is cycled. Thus, changes in effective stress take place (Dietl et al., 2019,K. de-Kloe, 2008,H. L. Wang et al., 2017) as shown in figure 2.4-right.

As can be seen, pore pressure cycles are a closer condition to underground energy storage. Nevertheless, it can be more complicated to apply as an additional pump and control loop are required.

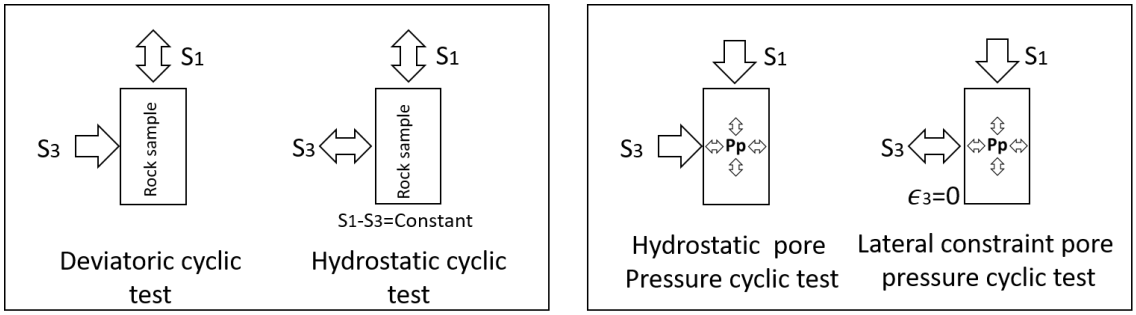


Figure 2.4: Type of cyclic loading and tests on rock samples. External loading tests (left), Pore pressure cycles (right). Where $S_1$ and $S_3$:Maximum and minimum stresses, Pp:pore pressure and e3:strain in the direction of the minimum stress.

In addition, concepts of poroelasticity need to be included for test interpretation. For this research, external loading is considered for simplicity.

### 2.0.5. Stress waveform and time dependent stress path

Different stress waveforms have been studied, with triangular and rectangular waveforms being the most popular. Nevertheless, there has been the application of sinusoidal and trapezoidal waveforms (Cerfontaine and Collin, 2018). The latter has been implemented in the laboratory to mimic underground energy storage conditions (Jiang et al., 2016). Figure 2.5 describes the mentioned waveforms as well as their main attributes: mean stress, amplitude, frequency and shape.

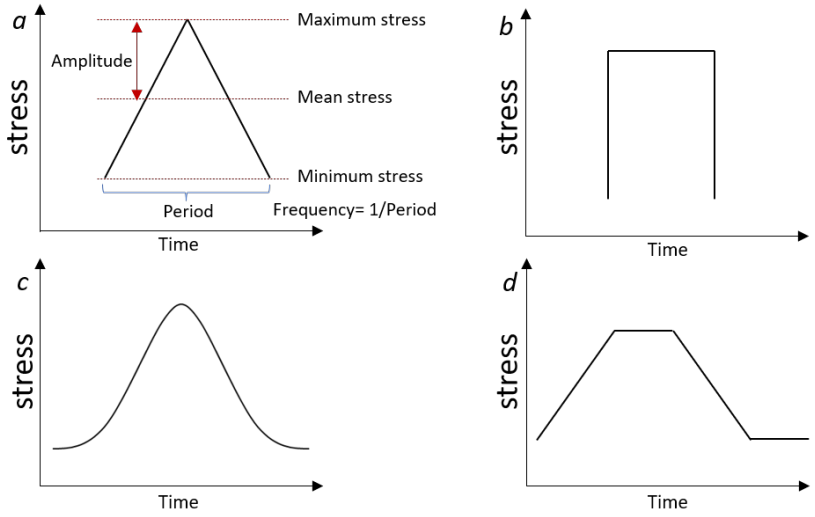


Figure 2.5: Main applied waveforms during cyclic loading experiments. a) Triangular b) Rectangular c) Sinusoidal d) Trapezoidal.

In addition to the waveform, the stress cycles can be applied following different stress paths as shown in figure 2.6. Constant amplitude is usually used to study fatigue of the material while damage control tests characterize the inelastic deformation presented during monotonic increasing stress tests (Cerfontaine and Collin, 2018,Pijnenburg et al., 2019). For underground energy storage, the stress paths of interest are constant amplitude and multilevel amplitude, because they mimic the conditions of constant volume storage and increasing volume storage respectively. The latter is becoming common in field applications due to the demand for higher storage capacity.

### 2.0.6. Most common cyclic loading tests

Regarding the conditions applied during cyclic testing, figure 2.7-left describes the type and number of cyclic loading tests found in the literature. On one hand, it can be seen that the most common are deviatoric cyclic tests, which include uniaxial and triaxial cyclic tests. In these tests, the axial stress

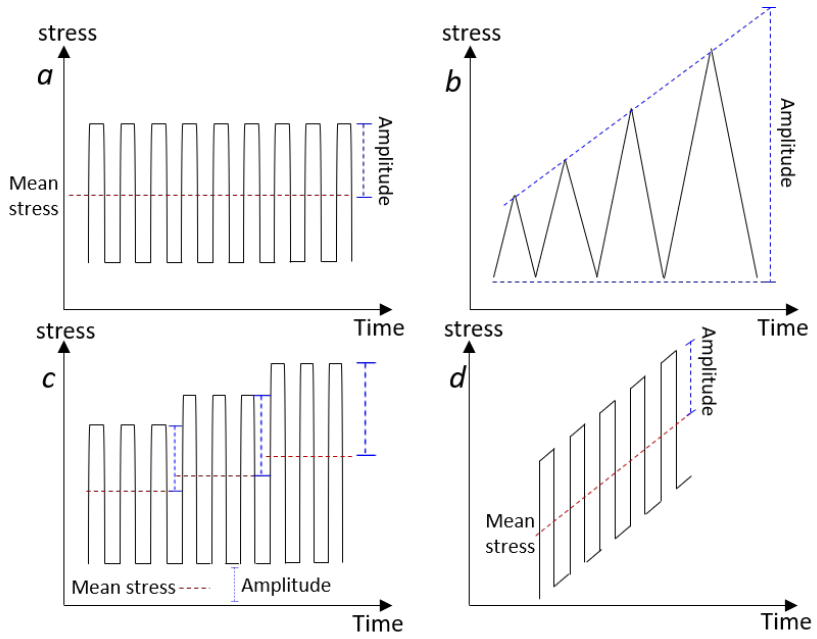


Figure 2.6: Stress path options: a) Constant amplitude b) Damage-controlled c) Multilevel amplitude d) ramp.

is cycled while the confining stress is kept constant as shown previously in figure 2.4-left. These conditions could be similar to those experienced by the reservoir rock in the near wellbore region during storage, where lateral strain at the wellbore's wall is allowed.

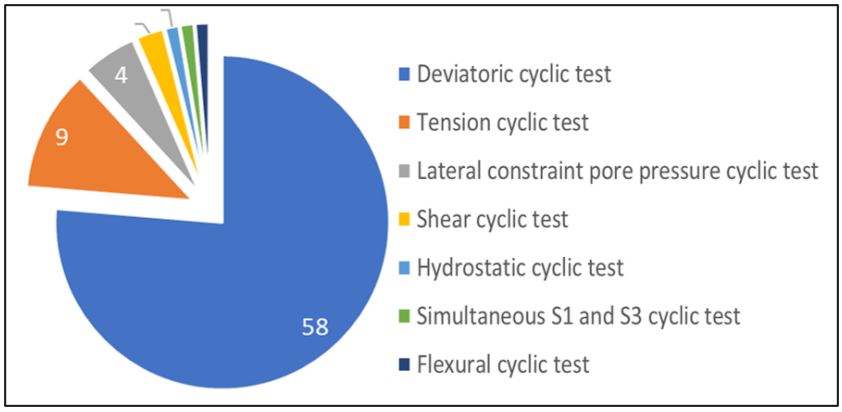


Figure 2.7: Type of cyclic tests after analysis of databases from Cerfontaine and Collin, 2018, Liu and Dai, 2021 and this thesis.

Tension cyclic tests follows the deviatoric tests. Most of them are Brazilian type, where a disk of rock is transversely loaded in indentation points located at the top and bottom of the disk. This kind of test could be of interest for the study caprock's flexure during cyclic loading.

On the other hand, the less popular tests are shear, hydrostatic, flexural and lateral constraint pore pressure cyclic tests. The latter have been developed to mimic the stress storage conditions experienced by a reservoir located in a sedimentary basin, where lateral strains can be considered zero (Dietl et al., 2019 and K. de-Kloe, 2008).

### 2.0.7. Comparison of stress paths between field conditions and cyclic loading tests

It is important to understand what type of cyclic test, in terms of stress path and waveform, offers the closest condition to field condition. Figure 2.8 shows the comparison between stress paths of storage field experiences and those corresponding to the most popular cyclic loading tests. It is possible to see that lateral constraint pore pressure cyclic tests represent closer the stress path of field storage experiences than any other test. However, these tests are not common as shown in figure 2.7. This is probably because the research has been mainly motivated by mines and civil activities and second because these tests are complex and require special equipment able to provide pore pressure oscillations and lateral constraint conditions. Deviatoric cyclic tests follow second, these tests have a higher contribution of deviatoric stress than field experience. Finally, hydraulic cyclic tests only offer a variation of pressure stress. The present research tried to mimic the stress path at field conditions as much as possible using deviatoric cyclic tests (as described in Chapter 4).

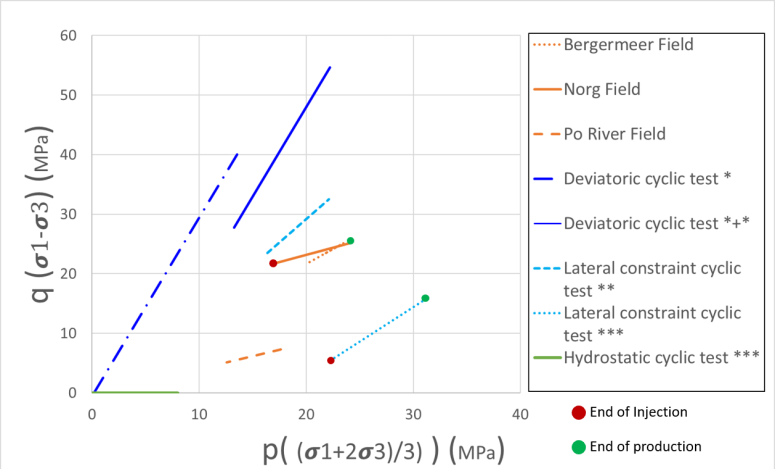


Figure 2.8: Comparison of stress path between underground gas storage field experiences and most popular cyclic loading tests. Path stresses are expressed with invariants 'p' and 'q', considering axisymmetric conditions ($\sigma_2 = \sigma_3$). *Burdine, 1963, *+* Taheri et al., 2016, **K. de-Kloe, 2008,***Dietl et al., 2019, Norg field from N.A.M., 2016, Bergermeer Field from Muntendam-Bos et al., 2008 and Po River Field from Teatini et al., 2011.

| Project name or location | Reservoir type | Reservoir rock | Cap rock | Stored Fluid | $\sigma_1$ / $\sigma_3$ max. (MPa) | $\sigma_1$ / $\sigma_3$ min. (MPa) | $P_p$ mean / fluctuation (MPa) | Period (days)/ Frequency (Hz) |
|---|---|---|---|---|---|---|---|---|
| Bergemeer* | Depleted gas | Sandstone | Salt rock | Gas | 40.3 /15.12 | 34.7 / 12.9 | 10.5/ 5.6 | 365 / 3.17e-8 |
| Norg** | Depleted gas | Sandstone | Salt rock | Gas | 39.8 / 16.3 | 28.0 / 11.8 | 27.2 / 11.8 | 365 / 3.17e-8 |
| Po River basin*' | Depleted gas | Sandstone | Shale | Gas | 10.7 / 3.5 | 7.6 / 2.5 | 12.8 / 3.1 | 365 / 3.17e-8 |
| Southern Europe*'* | Aquifer | Dolomite & carbonate | Anhydrite | Gas | - - | - - | 24 / 4 | 365 / 3.17e-8 |

Table 2.1: Description of storage conditions during underground energy storage field projects. $\sigma_1$ and $\sigma_3$ stand for effective maximum and minimum stresses. Data from Muntendam-Bos et al., 2008*,N.A.M., 2016**,Teatini et al., 2011*' and Silverii et al., 2021*'*

### 2.0.8. Inelastic deformation during cyclic loading

Accumulation of inelastic deformation over cycles is the most notorious effect recorded when a rock is subjected to cyclic stresses as shown in figures 2.9 and 2.10. For constant amplitude tests in porous

rocks, its behavior is characterized by large inelastic deformations in the first cycles followed by a period with small variations in inelastic deformation and finally a period with a sudden increase in inelastic deformation that indicates the proximity of Fatigue failure (Song et al., 2013, Cerfontaine and Collin, 2018 and Royer-Carfagni and Salvatore, 2000). The inelastic deformations have been interpreted to be the result of fatigue damage caused initially by intergranular micro-cracking and finally by transgranular micro-cracking when the rock is close to failure Royer-Carfagni and Salvatore, 2000, irreversible closure of micro-cracks Cerfontaine and Collin, 2018 and brittle creep Haihong, 1990. The latter is likely to happen in low-frequency tests with appropriate ambient conditions, like the presence of water that promotes stress corrosion (Cerfontaine and Collin, 2018). Depending on the stress magnitude these inelastic strains can be related with compaction or dilation deformation behaviors (Gatelier et al., 2002). In addition, it has been shown experimentally by Dietl et al., 2019, that inelastic strains are also manifested as a stress response during lateral constraint pore pressure cyclic tests. In these tests, the total radial stress ($S_3$) decreases as the number of cycles increases due to inelastic behavior (2.10-left).

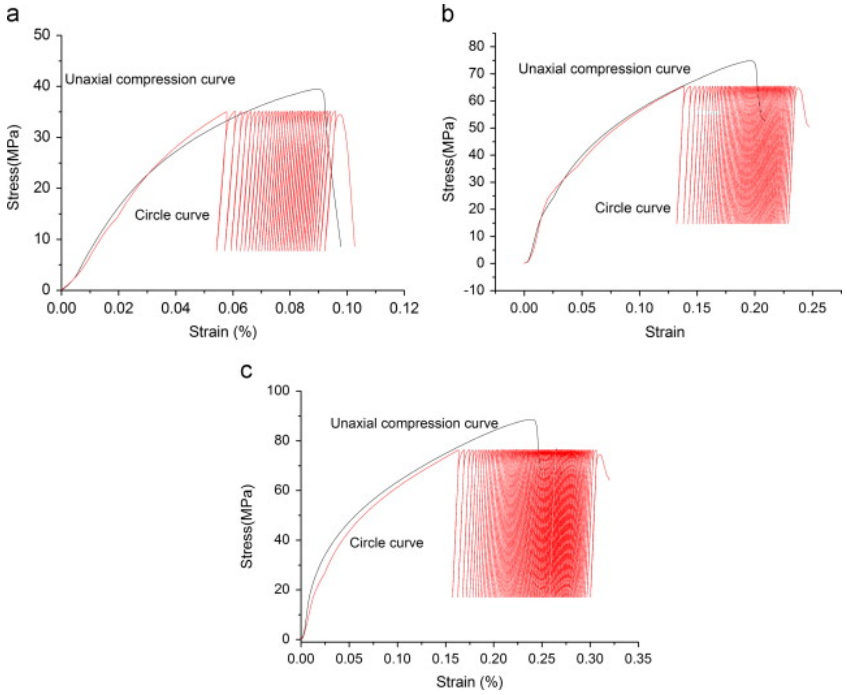


Figure 2.9: Accumulation of axial inelastic deformation during deviatoric cyclic tests in a salt rock for three confining pressure: a= 0 MPa, b= 3 MPa, c= 5 MPa Song et al., 2013. Figure used under Elsevier's licence number 5374180467963.

## 2.0.9. Objective of cyclic experimental studies on rocks

To understand the research status on cyclic loading in rocks, it was studied the general goal behind the published studies. These goals and the corresponding proportion of publications are shown in figure 2.11 and are described below.

In figure 2.11, it can be seen that **fatigue**, which is rock failure at stress levels lower than the static strength when cyclic loading is applied on a rock sample(Attewell and Farmer, 1973), has been by far the most studied topic due to its implication in the lifetime of rocks. The main results have been the generation of S-N curves (S: maximum cyclic stress or peak stress, N: number of cycles to reach failures) for different lithologies, which are used for engineering designs. Fatigue behavior can be classified in two types: Low-cycle fatigue, when the number of cycles to reach failure is between ten to hundreds, it usually takes place when the peak stress to rock compressive strength ratio is above 0.75 to 0.9 (Cerfontaine and Collin, 2018). The other group is high-cycle fatigue, where the number of cycles to reach failure is higher than $10^6$. Underground storage field application may mostly be in the latter group of fatigue behavior because the peak stresses are much lower than the rock peak strength.

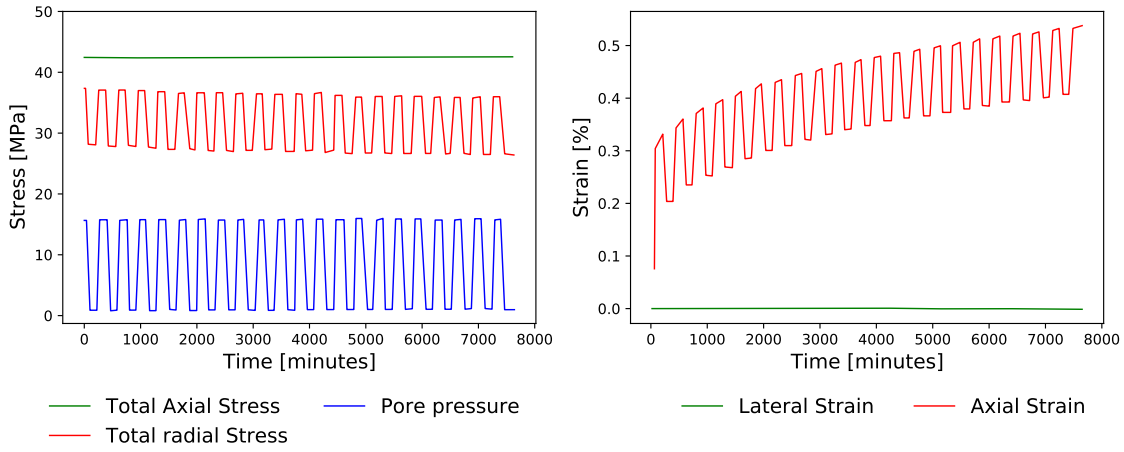


Figure 2.10: Results of lateral constraint pore pressure cyclic test in a sandstone. Accumulation of axial inelastic deformation (right). Decrease of the total radial stress as the number of cycles increases (left). Redrawn after Dietl et al., 2018. This figure is used under AAPG ©[2018] copyrights terms, reprinted by permission of the AAPG whose permission is required for further use.

Following fatigue, it comes **fatigue damage of the rock** as the topic more studied. Fatigue damage is the breaking of the bonds of the molecules that make the material, which at macroscale is exhibited as microcracks in the rock grains. This process has different stages such as ”nucleation, growth, and propagation of microcracks and microdefects in the grains of the rock” and evolves cycle after cycle (Y. Yang et al., 2018). The fatigue damage process is the reason behind inelastic strains accumulation cycle after cycle, fatigue failure and variation of mechanical and hydraulic properties of the rock (Gatelier et al., 2002). Researchers have been trying to correlate the damage process with macroscopic measurements like inelastic strains and elastic properties in order to build damage models that could be used for modeling purposes (Y. Yang et al., 2018 and Royer-Carfagni and Salvatore, 2000).

The third most popular objective of cyclic loading tests is the study of the **evolution of elastic properties**, known as Young’s modulus and Poisson’s ratio, over cycles. It’s been reported that these properties could change with the application of large amplitude cyclic stresses as a result of the damage process (Heap and Faulkner, 2008). For instance, tangent Young’s modulus has shown a behavior as followed: first increasing, second stabilization and finally degradation. While Poisson’s ratio tends to increase faster at initial cycles, then the increment slowdown and finally it increases sharply as the rock approaches fatigue failure. This behavior has been recorded for different lithologies (granite by Heap and Faulkner, 2008, rock salt by Ma et al., 2013b and sandstones by Peng et al., 2019b). It is of interest for underground energy storage applications to determine if these changes can take place under stress storage conditions, which usually are of low amplitude loading cycles in the elastic region with confining pressure higher than zero. The variation of these properties can impact subsidence and stress path on the faults.

Other properties of the rock, important for underground energy storage, can also be deteriorated or modified by cyclic loading like **porosity, permeability** as mentioned by S. Q. Yang and Hu, 2018, H. L. Wang et al., 2017 and LI et al., 2021. These properties affect directly the storage capacity and well injectivity. The study of **Kaiser effect**, which is the emission of acoustic signal when the stress applied on the rock is higher than previous stresses, has been studied with damage-controlled cycle tests by the analysis of acoustic emissions (Lavrov, 2001).

### 2.0.10. Conditions affecting cyclic loading rock deformation

The effects on rocks induced during cyclic loading like accumulation of inelastic deformation, fatigue and variation of mechanical and petrophysical properties of the rock are affected by different conditions

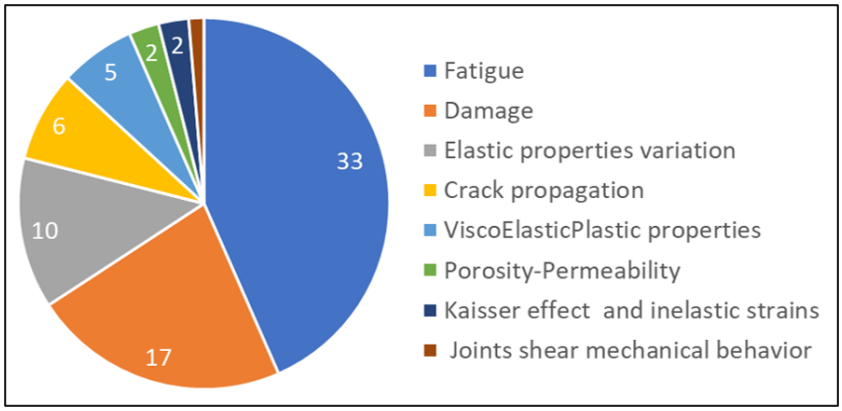


Figure 2.11: Main objective of the cyclic tests in rocks.

that can slow down or catalyze the deformation processes behind (fatigue damage, elastic deformation and creep), hence are of interest when analyzing field application or lab experiments. These conditions are listed below:

**Cyclic peak stress** : When peak stress of the cyclic loading is within the dilatant region and close to the peak strength of the rock, the fatigue damage develops fast (driven by crack nucleation and growth (Y. Yang et al., 2018) leading to fatigue failure. Nevertheless, It is possible that the rock never experiences fatigue failure for certain peak stress, at least for the patience of the observer(Cerfontaine and Collin, 2018). In fact, it has been reported that the rock could strengthen if the peak stress is not high enough as mentioned by Taheri et al., 2016 and Ray et al., 1999.

**Confining pressure** : It has been seen that fatigue life increases as the confining pressure is increased for the same peak stress -rock compressive strength ratio (Burdine, 1963, Song et al., 2013). This is because confining stress makes the rock behave more ductile. It has been observed than the higher the confining pressure the lower the changes of the elastic properties(Ma et al., 2013a).

**Saturating fluid** : Chemical reactive fluids can weaken the rock, which can catalyze the damage process, making the rock experience sub-critical crack growth. This can lead to a shorter fatigue life than the same sample in a dry condition (Cerfontaine and Collin, 2018).

**Mean Stress** : Fatigue life decreases as mean stress increases(Guo et al., 2012). Its magnitude defines the main deformation mechanisms during cyclic loading.

**Stress amplitude** : Higher the stress amplitude higher the damage (Haihong, 1990 and Fuenkajorn and Phueakphum, 2010). Stress amplitude defines the value of the peak stress.

**Waveform** : Rectangular waveform accumulates larger deformation than sinusoidal and triangular waveforms for the same number of cycles. This is partly due to the time brittle creep is acting in the peak and valleys of the waveform (Haihong, 1990 and Liu and Dai, 2021).

**Frequency** : for the same amplitude and mean stress of the waveform the higher the frequency the higher the fatigue life (Fuenkajorn and Phueakphum, 2010, Ma et al., 2013a, Attewell and Farmer, 1973) because there is lower contribution of creep. As mentioned by Cerfontaine and Collin, 2018) "Low frequencies are more likely to enable delayed crack propagation at high stress due to stress corrosion, while high frequencies are more favorable to fatigue mechanisms". This means that creep is of more importance during low-frequency conditions than fatigue damage.

**Time-dependent deformation properties** : In addition to the instantaneous inelastic deformation accumulated during every cycle, rocks may experience visco-elastic and brittle creep, which also contributes to the total deformation of the rock during cyclic loading (Haihong, 1990).Hence, creep properties are of interest and may be affected by cyclic stress condition (Fuenkajorn and Phueakphum, 2010). When comparing brittle creep tests with cyclic tests, the latter has a shorter lifetime than the former due to fatigue damage contribution.

**Presence of cracks** : The existence of initial cracks before cyclic loading catalyze the damage process and shorten the time to reach failure during cyclic loading.

**Lithology and anisotropy** : The more brittle the material, the shorter the fatigue life (Nejati and Ghazvinian, 2014). Depending on the orientation of the cycle stress applied with respect to the rock anisotropic the number of cycles to reach failure can change (Rassouli and Zoback, 2015).

**Grain shape** Each grain acts as an indenter during cyclic loading, then its geometrical shape is important in stress concentration within the grains, which can promote crack growth faster or slower Cerfontaine and Collin, 2018. Grain characteristics are also important for stress corrosion and brittle creep Cerfontaine and Collin, 2018.

### 2.0.11. Constitutive models for simulation of cyclic loading on rocks

As mentioned previously, depending on the cyclic loading conditions: frequency, lithology of the rock, stress and temperature conditions; instantaneous plastic deformation or/and time-dependent plastic deformation could take place or be predominant. These conditions have led to the derivation or proposal of different constitutive models to model cyclic deformations.

On one hand, creep models have been proposed for low-frequency cyclic loading (< 0.1 Hz) . For instance, Haghighat et al., 2020 combined a visco-plastic model (Perzyna-type) with an elasto-plastic model (Modified Cambribge Clay "MCC") to capture time-dependent deformation in clay-rich and carbonate-rich shales subjected to variable frequency cyclic loading. No cyclic plastic deformations were reported for the experiments used to test this model (Rassouli and Zoback, 2015). Kumar and Hajibeygi, 2021 used a power model from Xu et al., 2018 to model cyclic loading on a red sandstone. Results show the model is able to reproduce the loading and unloading deformations. Nevertheless, as the number of cycles increases, the model does not forecast as much deformation as recorded in the experiment. It could be the result of model coefficient characterization or the effect of time-independent inelastic deformations induced by cyclic loading.

On the other hand, the inelastic cyclic deformations in sandstones and clay-soils have been modeled with the use of elasto-plastic constitutive models based. For clay-soils the MCC model was extended for cyclic conditions (Carter et al., 1979). It was proposed a decrease of the pre-consolidation parameter of the yield surface during every downloading to reproduce the increase in inelastic strain per cycle seen in cyclic triaxial experiments. For sandstones, Cerfontaine et al., 2017 used a constitutive model called SANISAND, which is based on the bounding surface plasticity concept, to model inelastic strain evolution until failure.

# 3

# Theoretical basis

## 3.1. Stresses and strains

### 3.1.1. Stresses

The rocks that make up the earth's crust are subjected to stresses during the diagenetic and tectonic processes but also during human activities as shown in Figure 3.1.

Given that stress is a tensorial quantity and rocks have a porosity that can be filled with pressurized fluids, multiple stress definitions and nomenclatures are found in the literature. Here, those stress definitions used throughout this thesis are defined.

The total stress "$S_{ij}$" is a tensor variable that is usually split in two ways. The first way is recognizing that there are normal and shear stresses as shown in equation 3.1 that act on an infinitesimal cube of the rock. Where subindex "i" and "j" indicate the direction of the vector normal to the plane subjected to the stress and the stress direction respectively. It is a convention in rock mechanics that compression is positive as well as clockwise shear. In addition, for the system to be in equilibrium (no rotation of the solid), the stress matrix is said to be symmetric, then $S_{ij} = S_{ji}$.

$$S_{ij} = \begin{pmatrix} S_{1,1} & S_{1,2} & S_{1,3} \\ S_{2,1} & S_{2,2} & S_{2,3} \\ S_{3,1} & S_{3,2} & S_{3,3} \end{pmatrix} = \underbrace{\begin{pmatrix} S_{1,1} & 0 & 0 \\ 0 & S_{2,2} & 0 \\ 0 & 0 & S_{3,3} \end{pmatrix}}_{\text{normal stresses}} + \underbrace{\begin{pmatrix} 0 & S_{1,2} & S_{1,3} \\ S_{2,1} & 0 & S_{2,3} \\ S_{3,1} & S_{3,2} & 0 \end{pmatrix}}_{\text{shear stresses}} \tag{3.1}$$

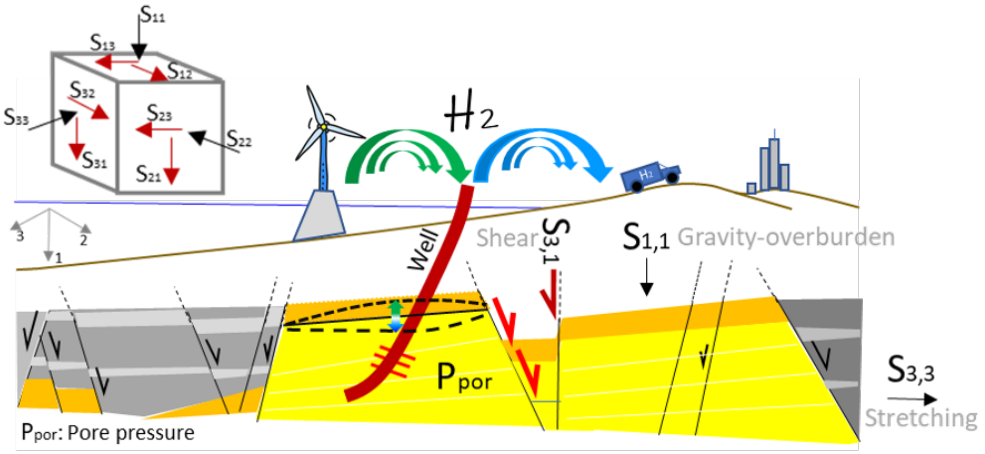


Figure 3.1: Geometric description of the stress state at the subsurface.

A second way of representing the stress matrix is splitting the stress tensor into a tensor called pressure "P" in which diagonal and non-zero components are the average of the total normal stresses. The other tensor is called deviatoric stress as shown in equation 3.2. This expression is shown in matrix and index notation in equations 3.2 and 3.3 respectively. It is important to mention that if there's no deviatoric stress, then there's no shear stress. This decomposition is useful to distinguish between the different strains as will be described later on.

$$S_{ij} = \underbrace{\begin{pmatrix} P & 0 & 0 \\ 0 & P & 0 \\ 0 & 0 & P \end{pmatrix}}_{\text{Pressure stresses}} + \underbrace{\begin{pmatrix} S_{1,1}-P & S_{1,2} & S_{1,3} \\ S_{2,1} & S_{2,2}-P & S_{2,3} \\ S_{3,1} & S_{3,2} & S_{3,3}-P \end{pmatrix}}_{\text{Deviatoric stresses}}, \; P = \frac{S_{1,1}+S_{2,2}+S_{3,3}}{3} \tag{3.2}$$

$$S_{ij} = \frac{1}{3}\delta_{ij}S_{kk} + D_{ij} \tag{3.3}$$

As mentioned previously, rocks are porous media filled with fluids. The pore pressure "$P_{por}$" exerted by these fluids makes the rock matrix experience differential stress, which is called effective stress "$\sigma$" and only affects the normal stresses. Equation 3.4 shows its mathematical representation in both index notation and explicit, where "$\alpha$" is the Biot coefficient from poroelasticity theory.

$$\sigma_{ij} = S_{ij} - \alpha * \delta_{ij} * P_{por} \;\rightarrow \sigma_{11} = S_{11} - \alpha * P_{por} \tag{3.4}$$

For any stress state, there is a certain rotation of the coordinate system that makes the diagonal terms of the total and effective stress tensors the only non-zero elements. These diagonal terms are called principal stresses and are denoted as follows:

- $\sigma_1 = \sigma_{1,1}$ and $S_1 = S_{1,1}$ 'Maximum principal effective and total stress respectively'
- $\sigma_2 = \sigma_{2,2}$ and $S_2 = S_{2,2}$ ' principal effective and total stress respectively'
- $\sigma_3 = \sigma_{3,3}$ and $S_3 = S_{3,3}$ 'Minimum principal effective and total stress respectively'

Another important stress concept is the Invariants. These expressions are stress-derived quantities that do not change with the rotation of the coordinate system. Thus, they are useful for the definition of a stress state and stress paths. The invariants 'p' and 'q', indicated by equations 3.5 and 3.6 for axisymmetric stress conditions ($\sigma_2 = \sigma_3$), known also as pressure and deviatoric stresses respectively, are used throughout this thesis.

$$p = \frac{(\sigma_1 + 2\sigma_3)}{3} \tag{3.5}$$

$$q = (\sigma_1 - \sigma_3) \tag{3.6}$$

### 3.1.2. Strain

The strain refers to the fractional change in size, shape or volume of a material as a result of an applied stress field. Figure 3.2 describes the strains based on the displacement of a solid subjected to a force. The strain, in 3 dimensions, is a tensor quantity as represented by equation 3.7. In triaxial conditions, it can be simplified up to three components, $\epsilon_1$ represents the strain in the direction of the maximum stress.

$$\epsilon_{ij} = \begin{pmatrix} \epsilon_{1,1} & \epsilon_{1,2} & \epsilon_{1,3} \\ \epsilon_{2,1} & \epsilon_{2,2} & \epsilon_{2,3} \\ \epsilon_{3,1} & \epsilon_{3,1} & \epsilon_{3,3} \end{pmatrix}, \text{ Triaxial convention: } \epsilon_{1,1} = \epsilon_1, \epsilon_{2,2} = \epsilon_2, \epsilon_{3,3} = \epsilon_3 \tag{3.7}$$

Strain can be divided into elastic '$\epsilon^{elastic}$' and inelastic '$\epsilon^{inelastic}$'. Elastic strains are those that can be recovered once the applied stress field is removed while inelastic strains cannot be recovered. In terms of energy, instantaneous elastic deformations do not lose energy while inelastic deformations do. In the current research, the term plastic strain is used to for instantaneous inelastic strains.

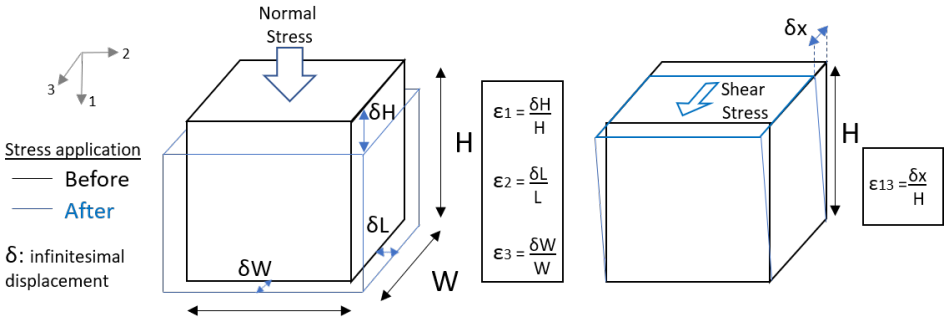


Figure 3.2: Illustration of normal (left) and shear (right) displacements and strains.

### 3.1.3. Cyclic loading strain - stress path

For cyclic loading, strain and stress follow different paths. This depends on the prescribed condition as shown in figure 3.3 from Wichtmann, 2005. On one hand, if stress is imposed as in figure 3.3-a, the strain shows hysteresis and accumulation. On the other hand, if the strain is prescribed, the stress will accumulate over the cycles as shown in figure 3.3-b. These behaviors are the result of inelastic strain accumulation and elastic properties changes.

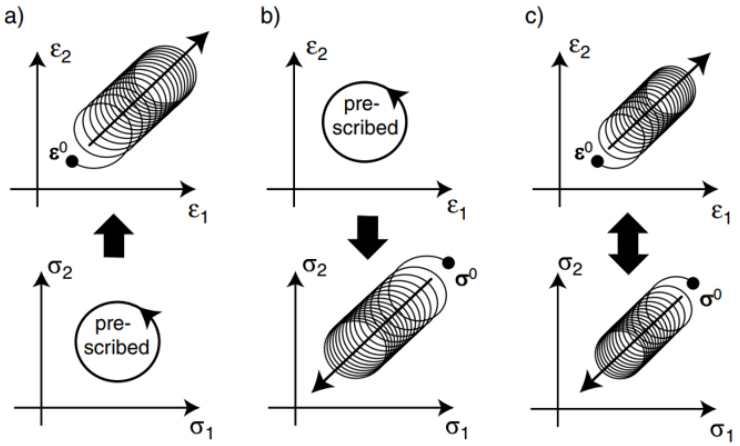


Figure 3.3: Illustration of strain (a), stress (b) and simultaneous strain-stress (c) accumulation during cyclic loading and deformation from Wichtmann, 2005.

## 3.2. Deformation of rocks

### 3.2.1. Elastic regime

When a rock can recover its original shape after the applied stress is removed, it is said to behave elastically. The elastic deformation regime for a sandstone (porous rock) corresponds to a straight line in a strain-stress curve from triaxial tests as shown in figure 3.4 . This regime is limited in the lower bound by the end of the closure of pre-existing cracks and at the upper bound by the brittle yield point or onset of dilatant cracking indicated by the letter **C** in figure 3.4. During the elastic regime, as the rock is compressed, there is a reduction of the porous volume, which is called elastic compaction. Nevertheless, sandstone and other porous rocks could show inelastic deformation at stress levels lower than the brittle yield point as discussed by Pijnenburg et al., 2018 and Gatelier et al., 2002, which leads to rock irreversible compaction. In fact, there could be another critical stress from which inelastic strains are triggered. This critical stress is called here compaction yield point. These inelastic strains are caused by intergranular fracturing, clay crushing and grain sliding (Pijnenburg et al., 2018 and Vermeer and de Borst, 1984). Thus, there is not necessarily a pure elastic regime in porous rocks.

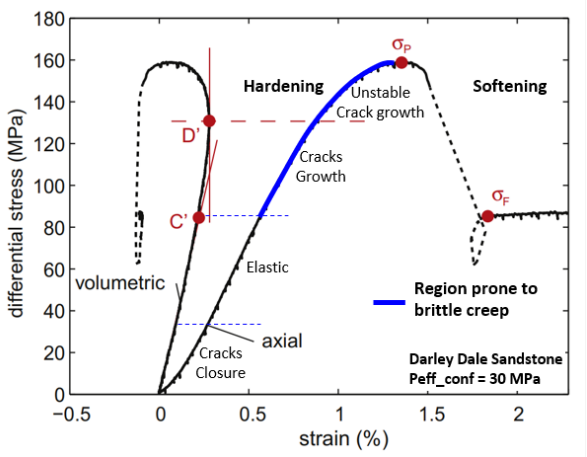


Figure 3.4: Stres-strain curve from a triaxial test on a sandstone sample. The deformation regimes and mechanisms before failure are indicated.$\sigma_p$:peak strength $\sigma_f$:fault sliding stress, C': Yield point and D':maximum volumetric contraction. Modified from Brantut et al., 2013. Figure used under Elsevier's licence number 5374250445271.

### 3.2.2. Brittle and ductile deformation regimes

Rocks can deform predominantly either under brittle or ductile behavior when stresses exceed its elastic limit **C** as shown in figure 3.4. This will depend on the temperature, confining stresses, strain rate and the characteristics of the rock itself.

On one hand, brittle deformation regime is the permanent breaking of the grain chemical bonds when stresses are higher than Brittle yield point **C** and the strain rate is so fast (from $10^{-3}sec^{-1}$ in an earthquake to $10^{-14}sec^{-1}$ during tectonic loading Brantut et al., 2014) that the deformation cannot be accommodated by plasticity. This behavior is manifested by the generation of fractures (joints and faults) at macroscale level and grain cracks at microscale level Shuguang Song, 2021. These cracks allow the grains to rotate and slide, which induce inelastic strain and dilation. Low confining pressure is the most important condition for brittle behavior. In a triaxial test, the brittle behavior can be identified when the tests lead to failure (i.e. localization of fractures in a shearing plane) as shown in figure 3.4

On the other hand, ductile deformation behavior is the process at which the rock changes its shape through bending or flowing. During this process, the chemical bonds could be broken but subsequently reformed into new bonds. It requires slow strain rates, so that molecular processes can take place and no fractures are generated. It involves creep mechanism as: diffusion creep, dislocation creep, mechanical twining, grain boundary sliding and diffusion rigid rotation Shuguang Song, 2021. For sandstones, ductile deformation is presented at high confining pressure and it is controlled by diffuse micro-cracking, also known as cataclastic flow that leads to a generalized fracturing deformation, i.e. there is not localization (Brantut et al., 2013). In ductile conditions, the most important parameters are temperature and strain rate.

### 3.2.3. Time-dependent deformation

Rock deformations and corresponding strains (elastic and inelastic) are usually thought to be instantaneous, such as elastic and plastic deformations. Nevertheless, rocks could also show that strain can change over time. For instance, when a stress condition is suddenly imposed and held, it could be seen that the strain builds up as time increases as shown in figure 3.5.

On one hand, If the stress condition is below the yield point, this may be the result of visco-elasticity, rheological behavior of the rocks and other materials that retards the elastic response of the rock. This behavior, called in the present thesis as **Viscoelastic creep**, has been reported for rocks including sandstones (X. Li and Yin, 2021). Inelastic compaction of the rock in the apparent elastic region could also be time-dependent. However, there is no complete understanding at this time (Pijnenburg et al., 2018).

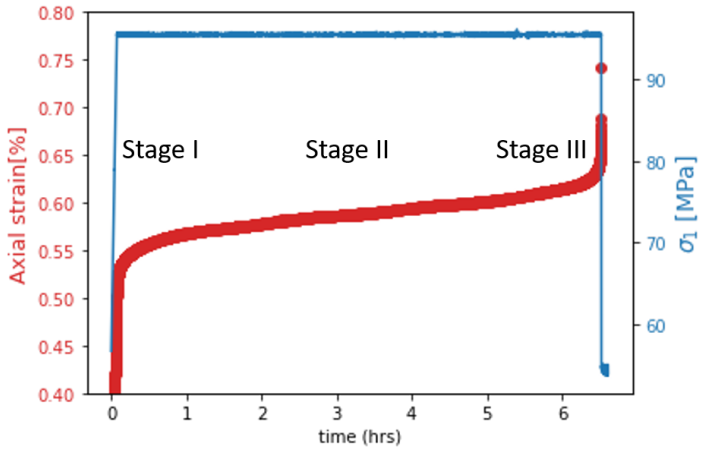


Figure 3.5: Time-dependent axial deformation during a triaxial brittle creep test. Early times (Stage I) are usually dominated by elasticity and viscoelasticity while the middle (Stage II) and late (Stage III) times are ruled by steady and accelerated brittle creep respectively. Data obtained during this thesis from Red Felser sandstone at confining stress of 10MPa.

On the other hand, if the stress is above the onset of dilatant cracking, brittle rocks could also show a time-depend irreversible deformation named **Brittle creep** (Brantut et al., 2013). This deformation is generated by sub-critical crack growth (cracks induced by stress intensity factor “KI” lower than fracture toughness ”KIC”) and grain sliding. The sub-critical crack growth depends on kinematic processes like stress corrosion, which makes it time-dependent. It can be affected by ambient conditions, such as temperature and pore fluid composition (Brantut et al., 2013). The evolution of brittle creep over time leads to failure of the rock (shear, cataclastic or compaction bands failure depending on the stress condition).

## 3.3. Constitutive models for instantaneous and time-dependent deformation

Constitutive models are equations that relate strain and stresses. These models are fundamental for the analytical and numerical modeling of rock deformation. These equations are functions of the mechanical rock properties and state conditions (stress, temperature).

### 3.3.1. Elastic model

The most popular of these equations is the one that describes the instantaneous linear elastic relationship between stress and strains. This model is called Hook model, after physics Robert Hook, and its simplest version is shown in equation 3.8, where E is Young’s modulus. This equation can be extended to 3 dimensions and isotropic conditions as shown in equation 3.9. This equation introduces the terms Poisson’s ratio ”$\upsilon$” (lateral to axial strain ratio) and lame’s constant ”$\lambda$” and ”$\mu$”.

$$\sigma_{11} = E\epsilon_{11}^{Elastic} \tag{3.8}$$

$$\sigma_{ij} = \lambda\delta_{ij}\epsilon_{ll} + 2\mu\epsilon_{ij} \tag{3.9}$$

Where: $\upsilon = \frac{\epsilon_{lateral}}{\epsilon_{axial}}$, $\lambda = \frac{\upsilon E}{(1+\upsilon)(1-2\upsilon)}$,$\mu = \frac{E}{2(1+\upsilon)}$

Alternative, equation 3.9 can be expressed in Voigt notation as:

$$\begin{pmatrix}\sigma_{1,1}\\ \sigma_{2,2}\\ \sigma_{3,3}\\ \sigma_{2,3}\\ \sigma_{1,3}\\ \sigma_{1,2}\end{pmatrix} = \begin{pmatrix}\lambda+2\mu & \lambda & \lambda & 0 & 0 & 0\\ \lambda & \lambda+2\mu & \lambda & 0 & 0 & 0\\ \lambda & \lambda & \lambda+2\mu & 0 & 0 & 0\\ 0 & 0 & 0 & \mu & 0 & 0\\ 0 & 0 & 0 & 0 & \mu & 0\\ 0 & 0 & 0 & 0 & 0 & \mu\end{pmatrix}\begin{pmatrix}\epsilon_{1,1}\\ \epsilon_{2,2}\\ \epsilon_{3,3}\\ \epsilon_{2,3}\\ \epsilon_{1,3}\\ \epsilon_{1,2}\end{pmatrix} \tag{3.10}$$

Equation 3.10 can be compressed to 3.11. Under the same concept, equation 3.12 relates small increments of strain and stress.

$$\sigma = D\epsilon^{Elastic} \tag{3.11}$$

$$\dot{\sigma} = D\dot{\epsilon}^{Elastic} \tag{3.12}$$

### 3.3.2. Plastic model

In general, plastic models for soil and rocks based on the flow theory of plasticity considered the existence of an initial yield and a subsequent yield surface (W. Chen and McCarron, 1983). Within this surface, deformations are elastic and beyond this surface deformations are elasto-plastic. The estimation of the plastic deformation is carried out with a flow rule. These models assumed that the total strain can be split in elastic and plastic strains (equation 3.13), such as stress is related to strain through equation 3.14.

$$\epsilon^{Total} = \epsilon^{Elastic} + \epsilon^{Plastic} \tag{3.13}$$

$$\dot{\sigma} = D(\dot{\epsilon}^{Total} - \dot{\epsilon}^{plastic}) \tag{3.14}$$

One of the most popular models for soils is the Modified Cambridge Clay 'MCC', which states that in the space formed by the stresses 'p' and 'q' and the void ratio 'e' there is a yield surface beyond which instantaneous inelastic strains are developed Carter et al., 1979. This is an associative model because the yield surface rules plastic flow. The critical state line indicates whether the rock will go through strain hardening (plastic strain and stress increases) or strain softening (plastic strain increases while stress decreases). For a detailed description of this model, the reader is referred to Carter et al., 1979. This model is of interest for the current research because it has been shown by Pijnenburg et al., 2019 that it can be used to model the inelastic strains of sandstone during compaction (i.e. when the stress is lower than the brittle yield point). In addition, it has the potential to model cyclic plastic strains as shown by Carter et al., 1979, who modified the MCC to predict the behavior of clay soils under cyclic loading.

For rocks, plastic compaction and dilation as well as hardening and softening behavior need to be modeled. One of the models that can reproduce this behavior is the Hardening - Softening model presented by Vermeer and de Borst, 1984. This model uses non-associative plasticity, which means that the yield surface (Mohr-Coulomb failure criteria) is different than the potential plastic flow surface. It is based on the evolution of the friction angle (increase) and cohesion (decrease) of the rock with respect to the inelastic strains. It has the capacity to forecast dilation hardening, which takes place after the onset of dilatant cracking.

Models based on similar plasticity theories that include a bounding surface in addition to the yield surface have been developed for cyclic loading of concrete and rocks (Vermeer and de Borst, 1984,Cerfontaine et al., 2017). These models are an option to model cyclic dilatant cracking.

### 3.3.3. Time-dependent inelastic model

As mentioned previously, rocks can exhibit more complex responses than instantaneous elastic strains, such as time-dependent elastic and inelastic deformations. One strategy for the development of constitutive models is assuming that the total strain can be decomposed as shown in equation

3.15. In this strategy, instantaneous and time-dependent elastic strains are represented by $\epsilon_{elastic}$ and $\epsilon_{viscoelasticCreep}$ respectively. While instantaneous and time-dependent inelastic strains are defined as $\epsilon_{plastic}$ and $\epsilon_{brittleCreep}$ respectively.

$$\epsilon_{total}(t) = \epsilon^{Elastic} + \epsilon^{ViscoelasticCreep} + \epsilon^{Plastic} + \epsilon^{BrittleCreep} \tag{3.15}$$

These complex strains can be modeled by deformation elements connected in series or parallel. These elements can be rheological-type like springs and dash-pots that also form higher order units like Kelvin and Maxwell units(Kelly, 2013). For example, the Nishihara model (X. Li and Yin, 2021; X. Wang et al., 2018) is able to model instantaneous and time-dependent elastic response as well as time-dependent inelastic response (Brittle creep for sandstones). The constitutive model solved for triaxial conditions is described by equation 3.16. It is comprised of an elastic unit, a Kelvin-Voigt unit and a Bingham unit connected in series as shown in figure 3.6. The latter unit models inelastic creep, assuming that the material behaves similar to a viscous liquid when the stress exceeds the strength of the material $S_{strength}$ (stress level at which the material's structure start to break). The strength of the material for rocks that show brittle creep is considered to be the onset of dilatant cracking or brittle yield point $\sigma_{yield}^{Brittle}$. It can be seen that in addition to elastic properties, a rheological property arises, called viscosity "$\eta$", which rules the time-dependent deformations. These types of models are useful to forecast the deformation of rocks under cyclic stresses, as shown by X. Li and Yin, 2021.

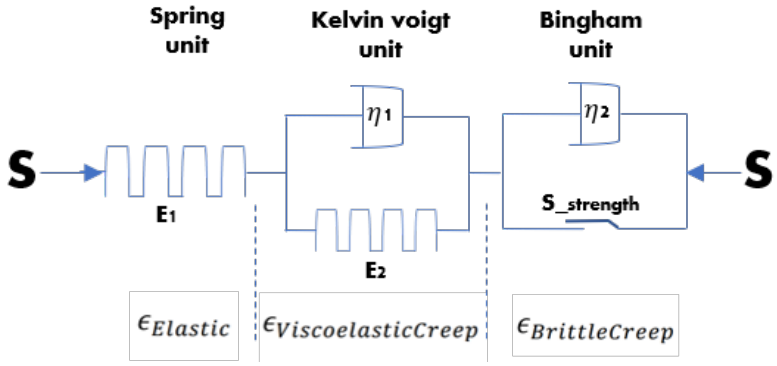


Figure 3.6: Nishihara rheological model from X. Li and Yin, 2021.

$$\epsilon_{total}(t) = \begin{cases} \frac{q}{E_1} + \frac{q}{E_2}(1 - \exp -\frac{E_2}{\eta_1}t) & \text{if } \sigma_1 < S_{strength} \\ \frac{q}{E_1} + \frac{q}{E_2}(1 - \exp -\frac{E_2}{\eta_1}t) + \frac{\sigma_1 - S_{strength}}{\eta_2}t & \text{if } \sigma_1 > S_{strength} \end{cases} \tag{3.16}$$

Where:

$q = \sigma_1 - \sigma_3$
$S_{strength}$= Brittle yield point for rocks.
$E_1$= Young's modulus of the spring unit.
$E_2$= Young's modulus of the Kelvin-Voigt unit.
$\eta_1$= Viscosity of the Kelvin-Voigt unit.
$\eta_2$= Viscosity of the brittle creep unit.

In addition to the Bingham unit (figure 3.6), there are also other approaches to model brittle creep. For instance, the Norton-Bailey constitutive model, which is shown in equation 3.17 and after integration in equation 3.18 is a popular approach to take into account non-linear behaviors (Xu et al., 2018). In these functions, the brittle creep strain rate "$\dot{\epsilon}$" varies with the stress, temperature and time. In these equations, $q_e$ is the effective deviatoric stress, U is the creep activation energy, R universal gas constant and m and n are four material constants that depend on temperature.

$$\dot{\epsilon} = mAq_e^{n-1}t^{m-1}\exp\frac{-U}{RT} \tag{3.17}$$

$$\epsilon_{BrittleCreep}(t) = Aq^n t^m \exp\frac{-U}{RT} \tag{3.18}$$

## 3.4. Acoustic emissions

Acoustic emissions 'AE' is the release of elastic energy when a material undergoes irreversible deformation like crack formation (Lockner, 1993). Nevertheless, it can also be the result of non-failure deformation mechanisms like friction. In any case, it is an irreversible energy phenomenon. In figure 3.7 is illustrated the phenomena and detection hardware.

AE have been used as an indicator of inelastic strains. In fact, the evolution of the number of AE versus time prior to rock failure shows a correlation between AE rate and inelastic strain rate as mentioned by Lockner, 1993. To detect and register these elastic waves, piezometric sensors are used. The registered signal is usually amplified and filtered to finally count the number of AE events and their intensity. This technique will be used during experiments as an additional way to monitor indirectly inelastic deformations.

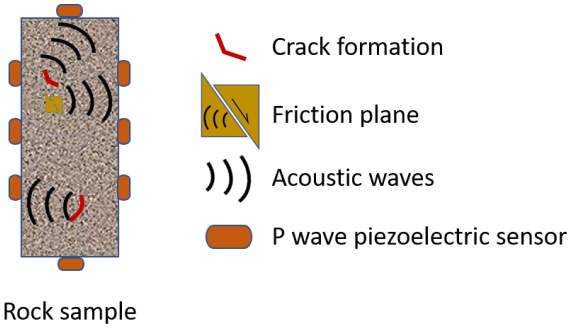


Figure 3.7: Illustration of acoustic emissions and sensing in a rock sample.

# 4

# Cyclic loading experiments

## 4.1. Material and equipment

### 4.1.1. Rock description

Red Felser sandstone, an early Permian rock from Germany, was selected as the reservoir rock for the cyclic experiments. A sample of this rock, used in the cyclic tests, is shown in figure 4.1.

Figure 4.1: Red Felser sample and tilting indicator equipment used to discard samples with ending surfaces that could lead to stress concentration areas during cyclic triaxial tests.

This rock was chosen based on:

- Its lithology and geological age, make it relevant for storage applications in the Slochteren sandstone in the Netherlands.
- Homogeneous properties.
- Available information from previous tests.

| Grain minerals | |
|---|---|
| Mineral | Volume(%) |
| Quartz | 89 |
| Orthoclase | 6 |

| Matrix minerals | |
|---|---|
| Mineral | Volume(%) |
| Kaolinite | 4 |
| Albite | 1 |
| Haematite | acc. |
| Chlorite | acc. |
| Ca-Apatite | acc. |
| Pyrite | acc. |
| Halite | acc. |

Table 4.1: Most likely mineral composition of Red Felser Sandstone, based on X-Ray Fluorescent ”XRF” and Scanning Electron Microscope ”SEM” studies from Eradus, 2019. acc stands for accessory

### Mineralogical composition

The mineralogical composition of Red Felser sandstone is shown in table 4.1. Quartz is the main grain mineral followed by Orthoclase. These grains are shown in figure 4.2. The main matrix mineral is Kaolinite.

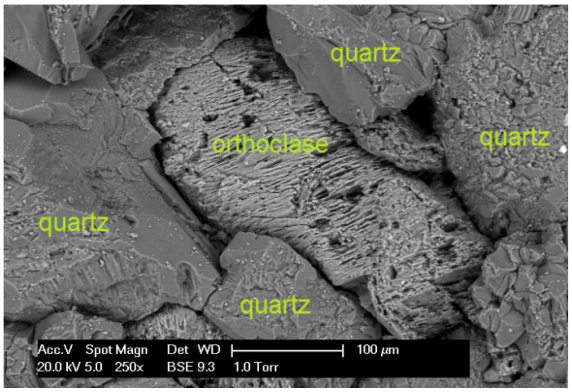


Figure 4.2: Image of quartz and orthoclase grains acquired through Scanning Electro Microscope ”SEM” for Red Felser sandstone from Eradus, 2019.

### Petrophysical and mechanical properties

The Red Felser sandstone has a medium porosity and a high permeability as shown in table 4.2. With respect to its mechanical properties, which are significant for this work, Young’s modulus and Poisson’s ratio of the rock are considered of normal magnitude for a consolidated sandstone. A resume of the properties can be seen in table 4.2.

| | | | |
|---|---|---|---|
| Porosity (frac.)* | 0.214 ± 0.007 | Young’s modulus (GPa) at $\sigma_3 = 10MPa$** | 20 |
| Permeability (Darcy)* | 1.27 ± 0.04 | Unconfined compressive stress (MPa)** | 45.5 |
| Color* | Red | Poisson’s ratio* | 0.125 |

Table 4.2: General petrophysical and mechanical characteristic of Red Felser sandstone from Eradus, 2019* and non-published data from the TUDelft-DeepNL project**

In addition, the design of the cyclic test program requires knowing the rock strength and brittle yield point at the corresponding selected confining stress. This information was estimated from TUDelft-DeepNL project data. For instance, figures 4.3 and 4.4 show that the rock strength and brittle yield point are approximately 120 MPa and 80 MPa respectively, for confining stress of 10 MPa. The brittle yield point was estimated graphically based on the change of the stress-strain derivative considering that the brittle yield point defines the end of the elastic deformation regime, which theoretical should show a linear strain-stress relationship (constant stress-strain derivative).

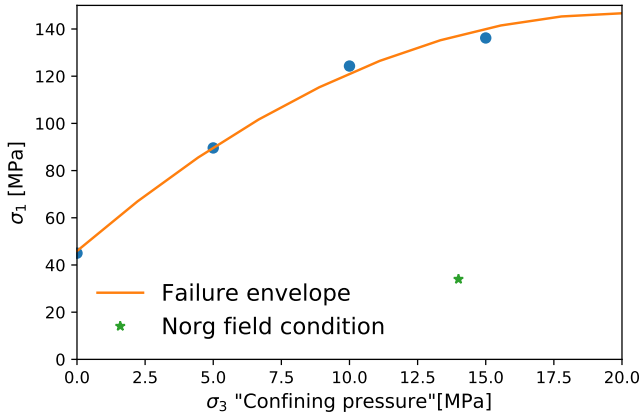


Figure 4.3: Red Felser sandstone failure envelop was obtained from triaxial tests at different confining pressure and room temperature. Interpreted from TUDelft-DeepNL project data. The Norg field average stress condition is also indicated.

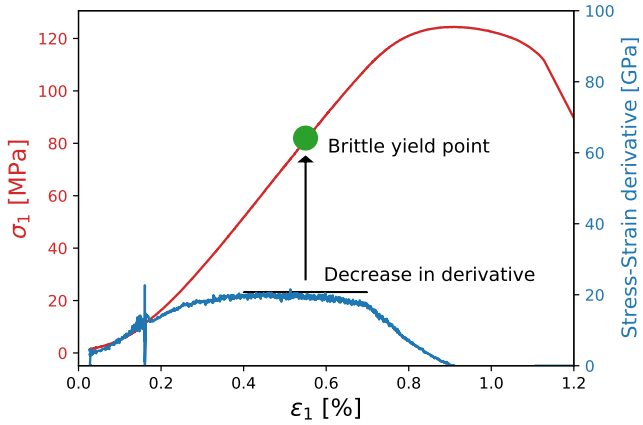


Figure 4.4: Definition of referential brittle yield point for Red Felser at confining stress of 10 MPa and machine temperature. Interpreted from TUDelft-DeepNL project data.

### 4.1.2. Rock sampling and geometry

All samples were obtained from a unique rock slab using drilling equipment. During drilling, zones with visible fractures were discarded. The samples have a cylindrical shape as shown in figure 4.1

Next, the samples were initially cut to a length of approximately 75mm and an average diameter of 29.5mm. Then, after sample selection based on porosity results, the samples were cut to their final length of 70mm for a corresponding length to diameter ratio of 2.37. It is important to mention that after cutting, the ending surface of the samples (top and bottom) were checked for flattening with a Mitutoyo tilt indicator as shown in figure 4.1. Samples with more than 0.15 mm difference along the border of the ending surfaces were discarded or cut again. This was performed to avoid stress concentration areas at the ending surfaces during cyclic tests. In addition, the ending surfaces of samples used in creep tests were also polished with a diamond disk.

### 4.1.3. 500 kNewton Equipment and triaxial cell

To carry out the triaxial cyclic test, also known as deviatoric cyclic tests, a displacement equipment of 500kN maximum force was used. This equipment is located at Gesteente mechanica (Geomechanic lab), CiTG, TUDelft. This is an important consideration when running long tests that require thermal stability of the system. It is relevant to mention that this equipment was not built for long tests like creep or low-frequency cyclic tests, where thermal-self regulation is needed. Thus, pre-heating of the cell and equipment was performed to reach thermal stability.

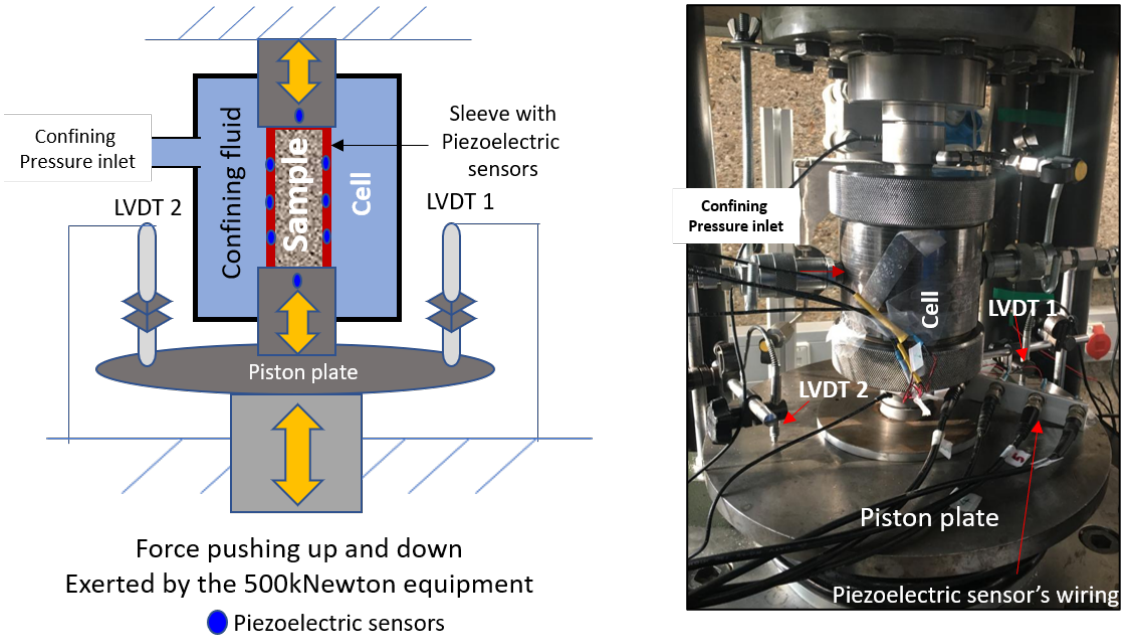


Figure 4.5: Triaxial cell schematic (left), 500 kN equipment and triaxial cell used during testing (right).

To conduct the deviatoric cyclic tests also known as triaxial cyclic tests, a triaxial cell was used together with the 500kN equipment as shown in figure 4.5. This cell allows the application of confining pressure thanks to a plastic sleeve that isolates the rock sample and the confining fluid. Furthermore, this sleeve has a total of 6 piezoelectric sensors embedded in it, which are used to record acoustic emissions "AE" coming from the rock. Two additional piezoelectric sensors are located in the pistons that transfer the force of the equipment to the sample.

**Equipment deformation**

The vertical displacement of the system is measured by two Linear Variable Displacement Transformer "LVDT", which are touching the 500kNewton equipment's piston plate as shown in figure 4.5. Then, a correction is needed to estimate the rock displacement and corresponding strain as shown in equation 4.2. This correction, called here Machine's correction, was estimated after running a deviatoric cyclic test with a cylindrical aluminum sample of known Young's modulus (70 GPa). The procedure was as follows: First, the strain of the aluminum sample was calculated using Hook's law and the deviatoric stress "q" was recorded in the first loading. Second, the machine strain was computed for every stress condition using equation 4.1. Third, a piecewise polynomial function was adjusted to the behavior of the machine strain versus the deviatoric stress. This resulted in equation 4.3, which is plotted in figure 4.6-left.

$$\epsilon_1 Machine = \epsilon_1 Total - \epsilon_1 aluminum \tag{4.1}$$

$$\epsilon_1 Rock = \epsilon_1 Total - \epsilon_1 Machine \tag{4.2}$$

$$\epsilon_{11} Machine = \begin{cases} 3.23 * 10^{-7} q^3 - 5.732 * 10^{-5} q^2 + 6.2453 * 10^{-3} q - 1.1277 * 10^{-3} & \text{if } q \leq 48 \text{ MPa} \\ 0.00299252 * q + 0.05786856 & \text{if } q > 48 \text{ MPa} \end{cases} \tag{4.3}$$

In addition, it was determined that the machine has inelastic axial deformation during cycling loading, as shown in figure 4.6-right. Then a second piecewise function for machine strain is considered

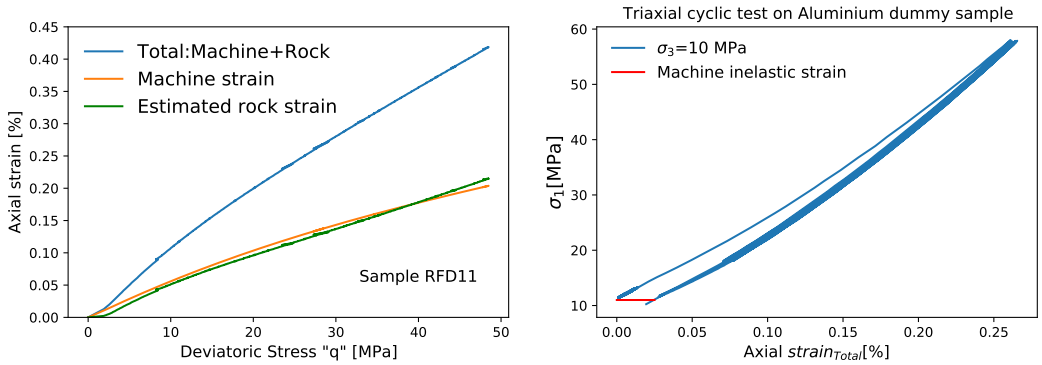


Figure 4.6: A graphic example of estimation of rock strain after subtraction of machine's strain from the total measured strain (left). Triaxial cyclic test result on the aluminum sample, where it can be seen that the machine has axial inelastic strain (right). A triangular deviatoric stress waveform was applied. Its characteristics were $\sigma_1 = 38MPa +/- 20MPa$, $\sigma_3 = 10MPa$ Frequency=0.014Hz.

for unloading and loading after the first cycle. It incorporates the machine inelastic strain. The inelastic strain of the machine depends on the maximum applied stress. It was derived two functions for maximum deviatoric stress '$q_{peak}$' lower and higher than 34MPa as shown in equations 4.4 and 4.5.

if $q_{peak} >$ 34 MPa

$$\epsilon_{11}Machine = \begin{cases} -4.3 * 10^{-9}q^4 + 7.6 * 10^{-7}q^3 - 7 * 10^{-5}q^2 + 5.7 * 10^{-3} * q + 0.026 & \text{if } q \leq 48 \text{ MPa} \\ 0.00299252 * q + 0.05786856 & \text{if } q > 48 \text{ MPa} \end{cases} \tag{4.4}$$

if $q_{peak} \leq$ 34 MPa

$$\epsilon_{11}Machine = -1.5 * 10^{-8}q^4 + 1.8 * 10^{-6}q^3 - 1.1 * 10^{-4}q^2 + 6.4 * 10^{-3}q + 2 * 10^{-2} \tag{4.5}$$

### 4.1.4. Acoustic emission monitoring and processing system

A Richter acoustic emission system was used to detect and record micro-seismic activities during various stress patterns and rates. The Richter is a multi-purpose, multi-channel, 16-bit ADC resolution and data acquisition and streaming system supplied by ITASCA. It provides a simultaneous and synchronous sampling of all input channels with sampling rates of up to 10Ms/s. This system was run in continuous mode. After the acquisition of the AE, they were filtered during the leaching step by applying the next conditions: The event must be detected by all piezoelectric sensors and the amplitude must be higher than 0.2 volts. With these filters is expected that noise caused by external factors, like rock-piston friction, is removed. The acquisition frequency used was 1 MHz.

### 4.1.5. What can be measured with the equipment

For the described experimental setup, the next variable can be measured or estimated:

- Axial displacement and the corresponding strain.
- The force applied and the corresponding stress.
- Acoustic emissions events and amplitude.
- The Young's modulus can be estimated as well as yield point and compressive rock strength.
- External temperature of the cell and equipment through a temperature gun.

Nevertheless, Poisson's ratio was not estimated because the radial displacement cannot be measured due to the limitations of the cell. This is an important parameter for stress evolution in lateral constraint systems.

### 4.1.6. Sources of error

Experimental measurement could be affected by errors related to the calibration and precision of the measuring tools. These errors can lead to misinterpretation of results. Here, it will be mentioned the possible sources of error and the strategies implemented to minimize them.

Strain estimation can be affected by errors during the geometrical characterization of the sample and the recording of the LVDT. For this situation, multiple measurements were performed in order to minimize the errors. For instance, two LVDT instead of one was used.

In addition, machine correction can also bring error to the estimation of the rock strain over time. It is recommended the use of polynomial functions to reproduce machine strain.

Nevertheless, it was noticed that the major error during cyclic test and creep test is the change of temperature because this leads to important deformation of the metal parts of the equipment and triaxial cell affecting the measured strain. This is especially important for tests lasting more than an hour. Thus, the equipment was left to warm up for approximately 8 hours to minimize this effect.

## 4.2. General test conditions

Conditions were defined to be relevant for underground energy storage. Thus, effective stress conditions from gas storage field application in NORG Field (N.A.M., 2016) were taken as the base case. Table 4.3 shows the general conditions and justification.

| Condition | Definition | Comment/Justification |
|---|---|---|
| Temperature | Machine temperature:<br>25°C - 30°C | The equipment does not have<br>a heating system to regulate temperature |
| Saturating Fluid | Water | Water is expected to be the wetting fluid in sandstone<br>storage systems. Water weakens the rocks |
| Water composition | Tap water | Easy access to the water source.<br>Nevertheless, its composition is unknown |
| Hydraulic condition | Drained | To capture the response of only the rock<br>and keep a constant pore pressure<br>equivalent to 1 atm |
| Referential effective stress | $\sigma_{1mean}$ = 38 MPa<br>$\sigma_3$ = 14 MPa ≈ 10MPa<br>Stress amplitude = 5.11 MPa | Biot coeficcient = 0.86<br>Data coming from NORG UGS project (N.A.M., 2016).<br>$\sigma_3$ was set to 10MPa due to creep equipment stress limit. |
| Cyclic loading<br>application | External loading | Easier to implement than pore pressure oscillations<br>but this assumes that grain compressibility is<br>negligible. Stress changes equal to pressure changes. |
| Type of cyclic<br>loading conditions | Deviatoric cyclic loading<br>Constant amplitude stress path | Deviatoric cyclic loading is the standard triaxial cyclic test<br>Cyclic pseudo-hydrostatic is closer to reservoir condition<br>but difficult to perform with the available equipment. |
| Stress waveform | Triangular | Relevant to underground energy storage |
| Maximum and minimum<br>frequencies | High 0.014Hz (1.2min/cycle)<br>Low 0.0002Hz (83min/cycle) | Test should have a minimum of 10 cycles and last 1 day. |
| Number of cycles | 8 | A total of 8 cycles is the maximum number<br>that can be done during 1 day for the lowest frequency |

Table 4.3: General conditions of the cyclic tests

### 4.2.1. Waveform

A triangular waveform was selected to approximate the cyclic stress behavior of underground storage field applications (N.A.M., 2016,Muntendam-Bos et al., 2008). Thus, the maximum stress of the waveform corresponds to the minimum pore pressure while the minimum stress refers to the maximum stored volume or pore pressure. A description of the main parameter that defines the waveform such

as mean axial stress, axial stress amplitude and frequency (period) are shown in figure 4.7. It is important to mention that the waveform considers constant stress rate during loading and unloading periods. Thus, the strain rate varies during these periods.

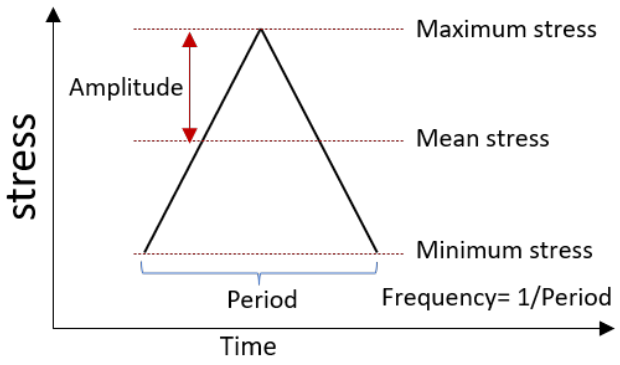


Figure 4.7: Selected waveform for cyclic loading experiments. Illustration of waveform parameters.

## 4.3. Test program

The test program aims to understand the deformation mechanisms involve during low-frequency cyclic loading in the regions above and below the onset of dilatant cracking (brittle yield point). Here, these regions are called brittle and elastic regimes respectively. The collected information should indicate and feed constitutive models relevant for sandstone deformation under cyclic loading. Therefore, the test program was defined to answer the next research questions:

**a)** Are the inelastic and elastic deformation during underground energy storage time-dependent or time-independent?

**b)** Does cyclic loading above and below the brittle yield point affect the deformation behavior?

**C)** How much does the stress amplitude affects the response of the rock?

The test program is shown in tables 4.5 and 4.6. It consists of a total of 12 deviatoric cyclic tests and 2 creep tests. Regarding the deviatoric cyclic test, two mean axial stresses were selected: one right above the brittle yield point "$\sigma_{1mean}1$" equal to 85MPa, in what is called brittle regime. The second mean stress was set below the brittle yield point "$\sigma_{1mean}2$" equal to 38MPa, defined here as elastic regime, because only elastic deformations were initially expected. For the frequencies, three scenarios were evaluated F1=0.014Hz (1.2 min/cycle),F2=0.0014Hz (12 min/cycle),F1=0.0002Hz (83 min/cycle). Finally, two axial stress amplitudes were tested A1=20MPa and A2=5.1MPa. The latter is equivalent to NORG field application. These conditions were permuted, leading to 12 cyclic tests with a maximum of 8 cycles.

Regarding brittle creep tests, that will provide the input parameters to model the cyclic test, two test were planned: the first one with a single stress level to evaluate if rock can creep and a second multi-stage creep test to calibrate a creep model. The latter consists of performing steps of increasing axial stress while keeping confining pressure constant (10MPa). Each step should last sufficient time for the rock to manifest creep (Heap and Faulkner, 2008).

## 4.4. Methodology

### 4.4.1. Sample characterization and selection

Porosity ($\phi$) of the samples was estimated using a pycnometer (ULTRAPYCNOMETER 1000). The pycnometer estimates the rock volume based on the expansion of a known gas (Helium) into the sample and using the Boyle law. It also estimates the density of the rock, which can be used to perform quality

| | F1 | F2 | F3 | |
|---|---|---|---|---|
| $\sigma_{1mean}1$ | RFD5 | RFD6 | RFD7 | A1 |
| $\sigma_{1mean}2$ | RFD8 | RFD10 | RFD18 | A1 |
| $\sigma_{1mean}1$ | RFD12 | RFD16 | RFD20 | A2 |
| $\sigma_{1mean}2$ | RFD14 | RFD17 | RFD21 | A2 |

Name of the sample

$\sigma_{1mean}1$= 85MPa, $\sigma_{1mean}2$=38MPa

F1=0.014Hz,F2=0.0014Hz,F3=0.0002Hz

A1=20MPa,A2=5.11MPa

Table 4.4: Deviatoric cyclic test program and cyclic imposed conditions. A total of 12 tests were executed, covering the possible combinations between the selected: 2 mean stress, 2 amplitudes and 3 frequencies at constant $\sigma_3 = 10MPa$

| Test | $\sigma_1$ [MPa] | Name of the sample |
|---|---|---|
| Creep | 95 | RFD22 |
| Multistage creep | 85<br>105<br>115 | RFD9 |

Table 4.5: Creep test program. A total of two creep tests were executed at constant $\sigma_3 = 10MPa$

control of the results. Finally, porosity is estimated based on the pore volume ($Volume_{pore}$) and the total volume ($Volume_{total}$) of the sample, using equation 4.6. For every sample, a total of 10 runs were performed to obtain an average value.

$$\phi = \frac{Volume_{pore}}{Volume_{total}} * 100\% \tag{4.6}$$

Porosity magnitude affects the deformation of the rock. For instance, the higher the porosity the lower the compressive strength and brittle yield point (Bedford et al., 2018). Thus, only samples within the range defined by the average porosity and a standard deviation of 1 percent of the samples were selected for the tests.

### 4.4.2. Cyclic loading and creep test

Next, it is described in detail the steps performed for system conditioning, deviatoric cyclic tests and creep tests.

**Experimental protocol deviatoric cyclic tests:**

- Saturate the sample with water.
- Glue the acoustic sensors attached to the cell's sleeve to improve coupling with the rock.
- Place the sample in the cell and center it.
- Place the pistons of cell, so that they are touching the 2 axial faces of the sample.
- Open the drainage valve of the bottom piston to guarantee drain condition.
- Apply initial confining pressure of 0.1MPa.

- Turn on the 500kN equipment.
- Place the cell in the equipment together with the metal accessories.
- Set a hydraulic condition equivalent to the confining pressure (10MPa) by increasing simultaneously the radial and axial stress.
- Leave the system (equipment and cell) heating up for at least 8 hours for low-frequency test (≤0.0014Hz). The equipment can be left warming up overnight and the test can be executed during the day.
- Increase the axial stress until the minimum stress of the waveform using a constant strain rate of 0.005sec-1. The control software must be in strain control. This step is called initial uploading.
- Switch the control software to stress control and use the built-in function to generate triangular waveforms. Introduce the mean stress, amplitude and frequency.
- Turn on the acoustic emission acquisition system and start the cyclic test.

**Creep tests:**

- After heating up the system for at least 8 hours, increase the stress until the desired level and hold it until at least secondary creep behavior or maximum allowed test time is reached.
- Record axial strain.
- For safety, it is recommended to set the maximum displacement and strain of the equipment to a value equivalent to the failure of the rock. Then, the piston will not move indefinitely, which could lead to cell's sleeve failure.

## 4.5. Data processing and estimation procedures

The data acquired during the tests needs to be corrected as well as treated to obtain the information of interest. In the case of the current tests, this information corresponds to strain behavior over time, inelastic strain, Young's modulus and acoustic events per cycle. For its estimation, the next main steps were followed:

- Strain data was corrected by machine deformation using equations 4.2 and 4.3.
- The total axial inelastic strain was computed by subtracting the strain of the initial loading from the strain at the final unloading at referential stress of 15 MPa as shown in equation 4.7. The stress was not decreased to exactly the confining pressure (10MPa) to avoid damage to the cell's sleeve.
- The cumulative apparent inelastic axial strain over cycle 'i' is estimated by subtracting the strains recorded every cycle and the first cycle at the minimum axial stress of the cyclic test (equation 4.8).
- It is necessary to remove the inelastic strain of the machine from the estimated strain of the rock.
- The Young's modulus was computed in the loading and unloading stress-strain trajectories of every cycle by adjusting a polynomial function of order 3 to every stress-strain interval and computing the derivative of this function at the axial mean stress of every test. For the initial loading, Young's modulus was always computed before the brittle yield point.
- To make the previous computations less time-consuming, a code written in python to detect the minimum (valleys) and maximum (peaks) stress points was developed. These peaks and valleys were used to compute the apparent inelastic strain per cycle as well as to define loading and unloading intervals require to estimate Young's modulus in every cycle.

$$\epsilon^{inelastic}_{Total_1} = \epsilon^{FinalUnloading}_{axial@\sigma_1=15MPa} - \epsilon^{InitialLoading}_{axial@\sigma_1=15MPa} \tag{4.7}$$

$$\epsilon^{inelastic}_{apparent_1} = \epsilon^{i}_{axial@\sigma_1=min.} - \epsilon^{InitialLoading}_{axial@\sigma_1=min.} \tag{4.8}$$

- For creep and cyclic tests in the brittle regime, the brittle yield point was estimated by identifying the decrease of the stress-strain derivative. The strain rate for the creep test was estimated by fitting a straight line to the points interpreted as part of steady-state stage.

# 4.6. Results

## 4.6.1. Porosity measurement and sample selection

A total of 18 samples were characterized in terms of porosity. Results are shown in table 4.6. It can be seen that the rock samples have similar porosity, with an average value of 19.65% and a standard deviation of 0.35%. Thus, all samples were accepted for conducting the cyclic test except sample RFD13, which porosity is more than 1% the average porosity.

| Sample | Diameter [cm] | Length [cm] | Porosity [%] |
|---|---|---|---|
| RFD4 | 2.947 | 7.017 | 19.171 |
| RFD5 | 2.951 | 7.033 | 19.706 |
| RFD6 | 2.956 | 7.026 | 19.785 |
| RFD7 | 2.97 | 7.013 | 19.606 |
| RFD8 | 2.971 | 6.977 | 19.833 |
| RFD9 | 2.96 | 7.021 | 20.568 |
| RFD10 | 2.97 | 7.028 | 19.78 |
| RFD11 | 2.962 | 7.013 | 19.166 |
| RFD12 | 2.972 | 7.018 | 19.631 |

| Sample | Diameter [cm] | Length [cm] | Porosity [%] |
|---|---|---|---|
| RFD13 | 2.97 | 7.004 | 20.638 |
| RFD14 | 2.958 | 7.022 | 19.241 |
| RFD15 | 2.964 | 7 | 19.469 |
| RFD16 | 2.96 | 7.009 | 19.724 |
| RFD17 | 2.972 | 7.006 | 19.204 |
| RFD18 | 2.952 | 7 | 19.036 |
| RFD20 | 2.967 | 7.018 | 19.849 |
| RFD21 | 2.953 | 6.998 | 19.648 |
| RFD22 | 2.96 | 7.009 | 19.916 |

| Average Porosity [%] | 19.635 |
|---|---|
| Lower limit [%] | 18.635 |
| Upper limi [%] | 20.635 |

Table 4.6: Estimated porosity for Red Felser samples. Also indicated the upper and lower limits used to accept a sample

## 4.6.2. Stress and strain behavior over time

The imposed stress and resulting axial strain were recorded for all 12 tests. Figures 4.8 and 4.9 show the strain behavior against time for the tests with the lowest frequency ”F3” and larger amplitude ”A1” in both regimes: Brittle and elastic. In these figures, it can be seen that the axial strain increases from one cycle to the other. This is more evident for the test in the brittle deformation regime (figure 4.8-left), where the peaks and valleys show a clear rising trend.

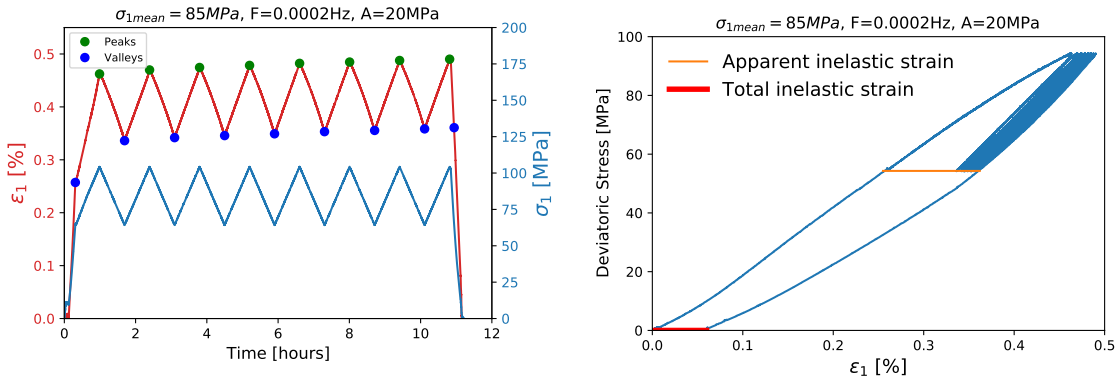


Figure 4.8: Imposed cyclic stress and strain response during time show that strain behavior changes from one cycle to the other (left). Cyclic Stress-strain response showing the total inelastic strain (right). ’Brittle regime’ and $\sigma_3$=10 MPa.

It can be also seen in the stress-strain curve (Figures 4.8-right and 4.9-right) that the final unloading curve has a concave shape that indicates visco-elasticity and it is the reason why the apparent inelastic

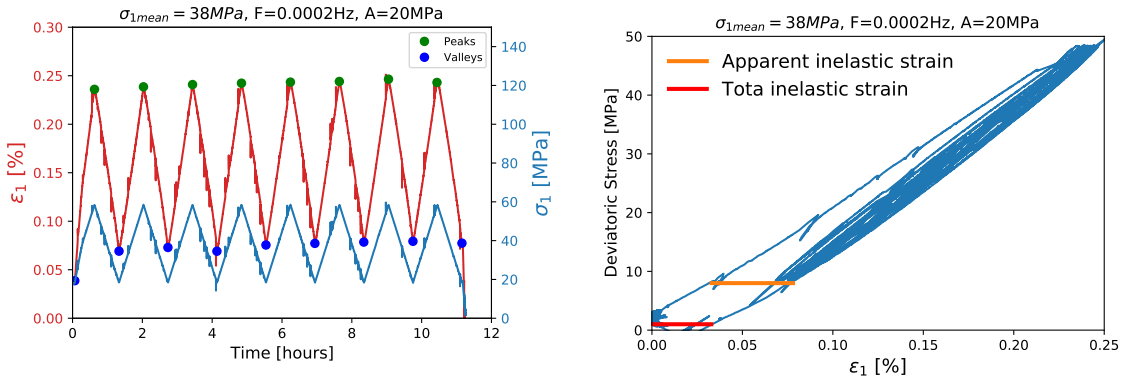


Figure 4.9: Imposed cyclic stress and strain response during time show that strain behavior changes from one cycle to the other (left). Cyclic Stress-strain response showing the total inelastic strain (right). 'Elastic regime' and $\sigma_3$=10 MPa.

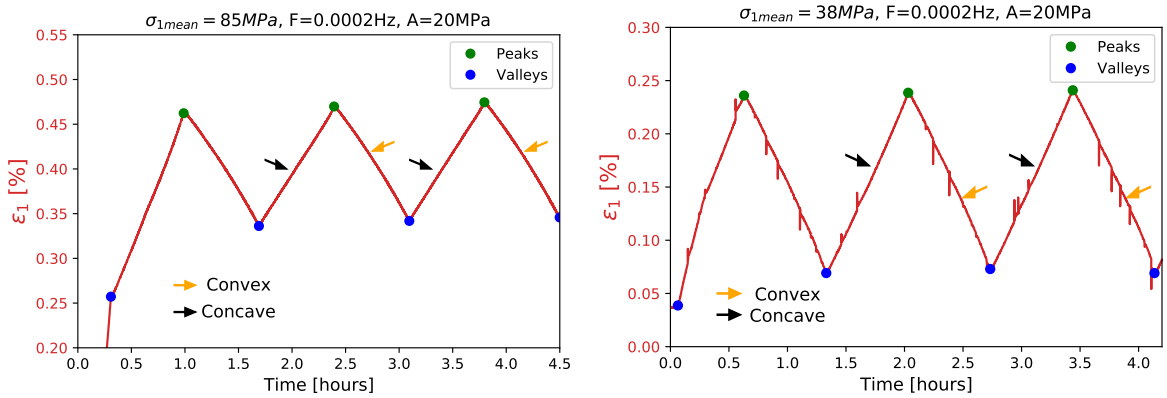


Figure 4.10: Strain behavior in the first three cycles for test $\sigma_{1mean}$1,F3,A1 and $\sigma_{1mean}$2,F3,A1.

strain is larger than the total inelastic strain. This behavior is more obvious for the test in the brittle regime. Figure 4.10 shows in more detail the strain response in the first three cycles of the mentioned tests. It can be seen that the unloading intervals show a convex shape while the loading intervals are concave or linear over time. It can also be seen that for the test with $\sigma_1$=38MPa there are some stress and strain spikes originated by instabilities in the control system.

### 4.6.3. Total inelastic axial strain

The total inelastic strain after 8 cycles was estimated following equation 4.7 for all the 12 cyclic tests. The results are shown in figure 4.11. The next observation can be done:

- As expected, there are inelastic strains when cyclic loading is applied in the brittle regime. ($\sigma_{1mean}$ > brittle yield point) but more interesting is that there are also inelastic deformations in what was expected to be the elastic regime ($\sigma_{1mean}$ < brittle yield point).
- Inelastic strains in the brittle regime are larger than in the elastic regime.
- Stress amplitude has also an impact on inelastic strain in both regimes. The larger the amplitude the larger the inelastic strain.
- Frequency affects the total inelastic strain in both deformation regimes: elastic and brittle. The effect of frequency is apparently more pronounced in the elastic regime, but this could be the effect of sample differences.

### 4.6.4. Cumulative apparent inelastic strain over cycle

Ideally, inelastic strain should be measured at deviatoric stress equal to zero. Nevertheless, during the cyclic tests the minimum stress level was higher than zero as shown in figure 4.8-left. Therefore,

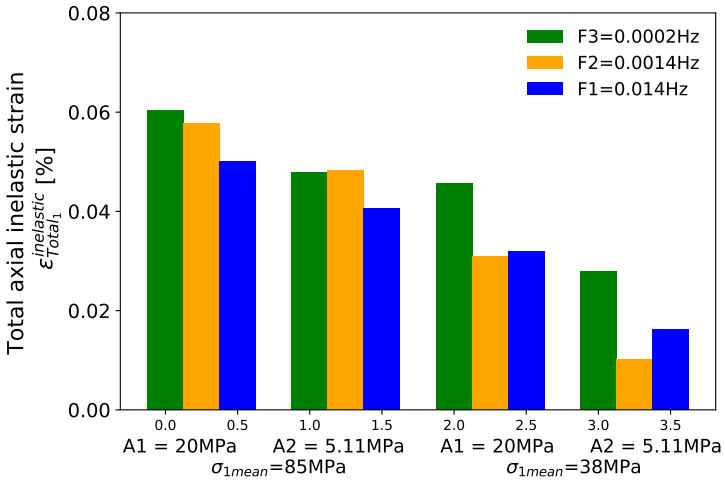


Figure 4.11: Effect of deformation regimes Brittle ($\sigma 1mean = 85MPa/$) and Elastic ($\sigma 1mean = 38MPa/$), Amplitude "A" and frequency "F" on total inelastic strain after 8 cycles.

when computing the inelastic strain at this stress level following equation 4.8, its value is apparent '$\epsilon^{inelastic}_{apparent_1}$'. This is because, it is affected by elastic deformations of the rock that could depend on time (viscoelasticity) and stress magnitude as shown in figure 4.8-right. Nevertheless, it is used as a qualitative estimation to understand the evolution of inelastic strain per cycle. Figures 4.12 and 4.13 show typical results obtained in every test. The main observation is that the largest $\epsilon^{inelastic}_{apparent_1}$ occurs in the first cycle. For the next cycles, the rate of $\epsilon^{inelastic}_{apparent_1}$ per cycle decreased, approaching zero either for tests in the 'elastic regime' or with lower amplitude.

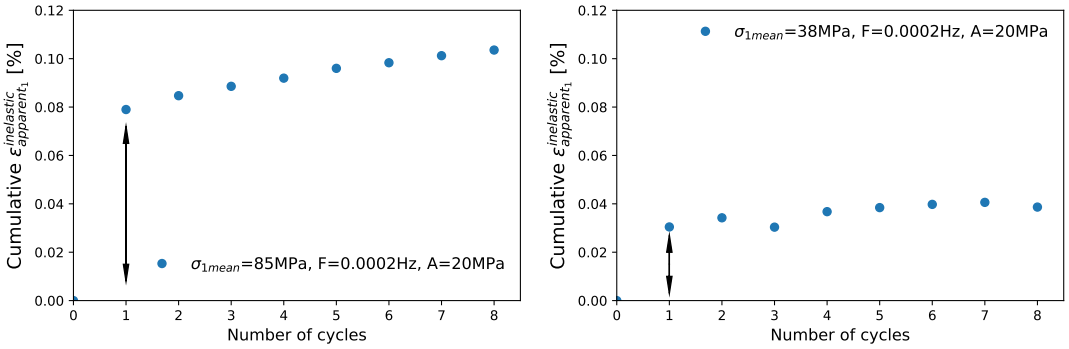


Figure 4.12: Apparent inelastic axial strain versus the number of cycles in both studied regime: Brittle regime (left) and supposed elastic regime (right), for the lowest frequency and maximum amplitude. Arrows indicate the major change.

To complement the analysis, results of the cumulative apparent inelastic strain of the 12 tests were plotted for the same amplitude and deformation regime. The apparent inelastic strain of the first cycle was removed, to improve the comparison and focus on strain evolution over the cycles. Figure 4.14-left shows that deformation in the brittle is time-dependent; the lowest the frequency the largest the deformation. This time-dependent deformation is interpreted to be caused by visco-elastic and/or brittle creep. For the tests in the elastic regime there is apparently no time-dependent deformation (figure 4.15 and 4.14). Results can be affected by heterogeneity between the samples, test duration, strain rate, sensor's resolution (1 µm) and test instabilities.

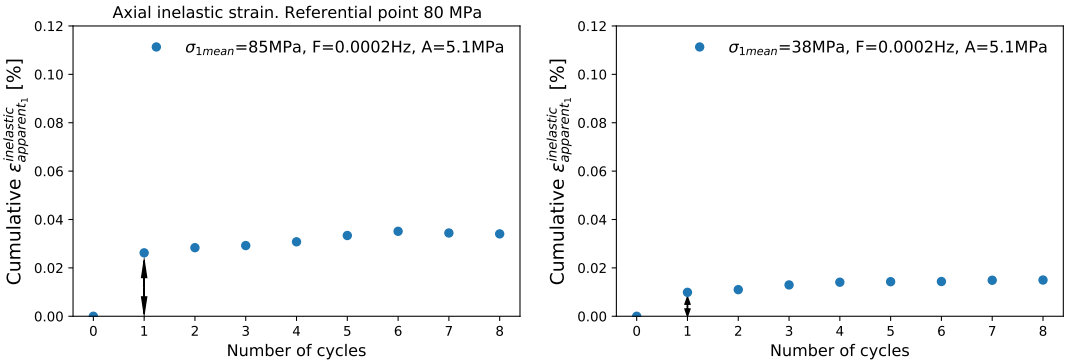


Figure 4.13: Apparent inelastic axial strain versus the number of cycles in both studied regime: Brittle regime (left) and supposed elastic regime (right), for the lowest frequency and amplitude. Arrows indicate the major change.

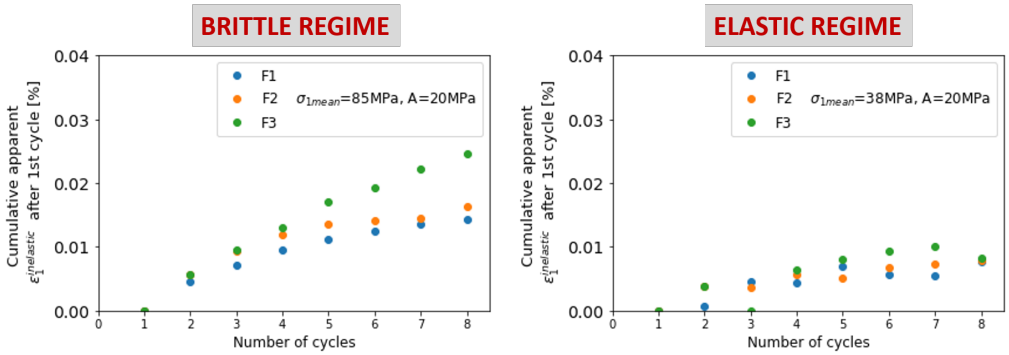


Figure 4.14: Comparison of cumulative apparent inelastic strain after removing the first cycle for the different tested frequencies (F1=0.014Hz, F2=0.0014Hz,F3=0.0002Hz) at amplitude of 20 MPa. Time-dependent deformation is prominent for the cases tested in the brittle region but it is not obvious in the elastic regime.

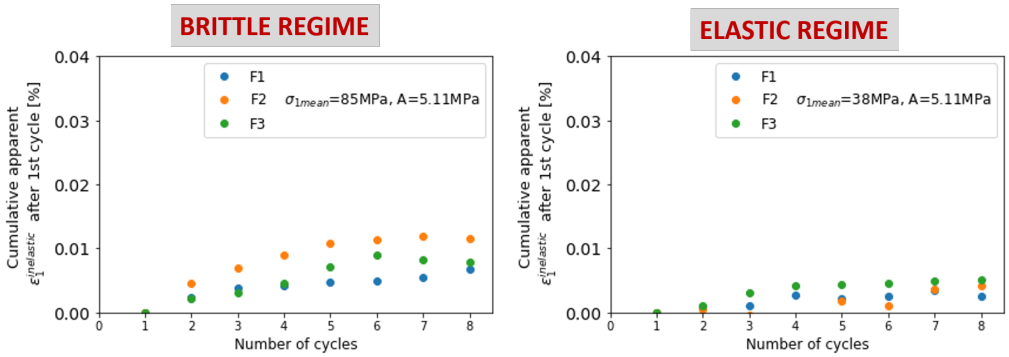


Figure 4.15: Comparison of cumulative apparent inelastic strain after removing the first cycle for the different tested frequencies (F1=0.014Hz, F2=0.0014Hz, F3=0.0002Hz) at an amplitude of 5.11 MPa. There is not a clear trend because the deformation is small making it sensible to instabilities.

### 4.6.5. Young's modulus behavior

The tangent Young's modulus E, also defined as apparent E because inelastic strains and other non-linear deformations are taking place, was estimated in the loading and unloading intervals as shown in figure 4.16-right. On one hand, it is seen that E from loading intervals showed an increase between the first to the second cycle similar to the increase in the apparent inelastic strain. On the other hand, E calculated from the unloading intervals is almost constant along the cycles, i.e. there is not an increase from the first to the second cycle as estimated in the loading intervals.

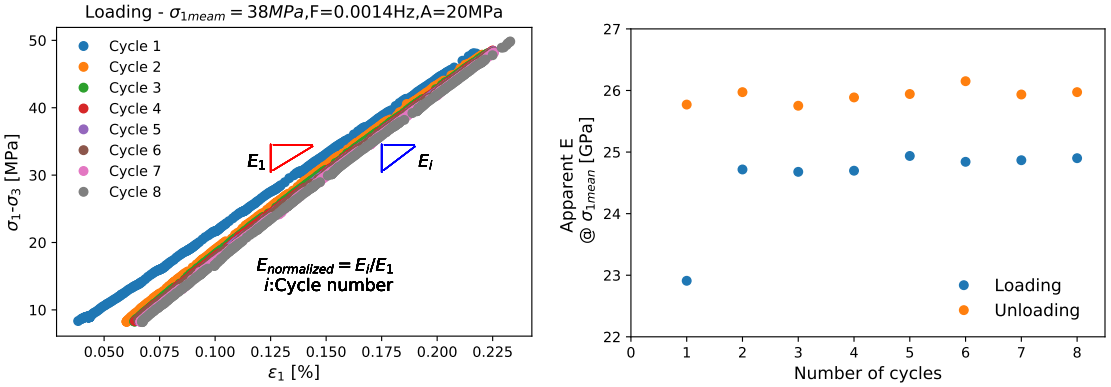


Figure 4.16: Illustration of estimation of Young's modulus in loading intervals (left). Comparison of Young's modulus estimated from loading and unloading intervals of each cycle(right).

Furthemore, the unloading E and normalized E were plotted for all experiments, as shown in figure 4.17. It can be seen that amplitude and deformation regime play an important role in apparent E behavior, especially for tests in the brittle regime where the larger the amplitude the lower the increase. In addition, the apparent E in brittle regimes is higher than in elastic regimes.

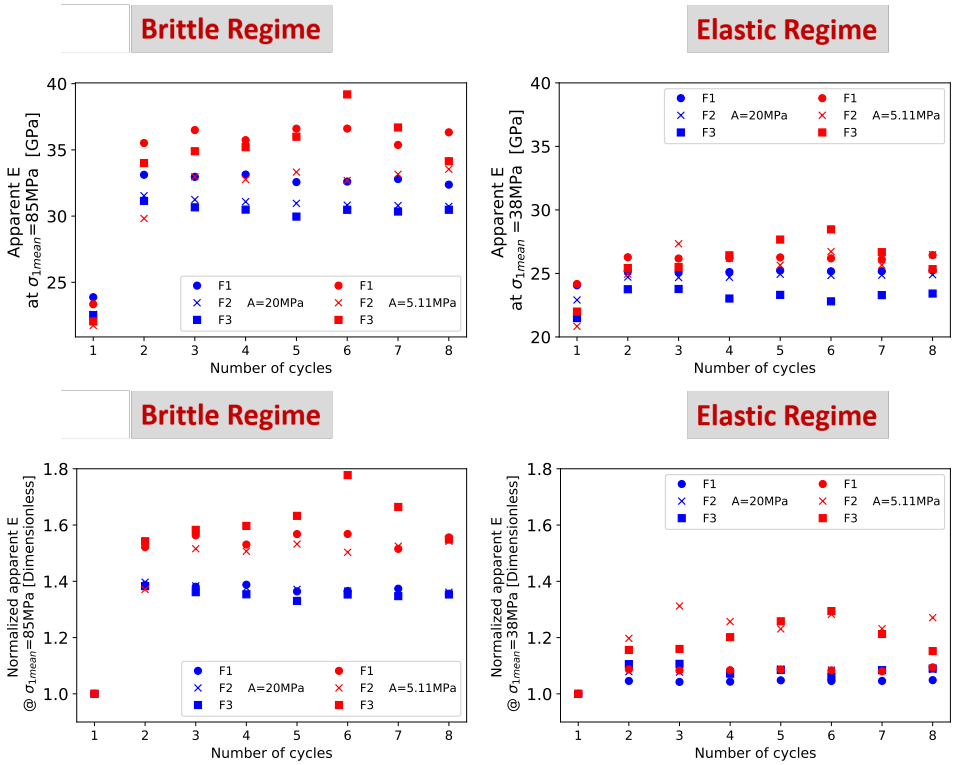


Figure 4.17: The behavior of loading Young's modulus (top) and its normalization (bottom) against frequency and amplitude during cyclic loading for both deformation regimes: Brittle (left) and Elastic(right).

### 4.6.6. Acoustic emissions

The acoustic emissions 'AE' were recorded only for the tests corresponding to the maximum stress amplitude because the waveform acquisition and processing was a memory-demanding and time-consuming task. For instance, low-frequency tests took 3 weeks for processing with the computer available at the laboratory. Nevertheless, important observations were made.

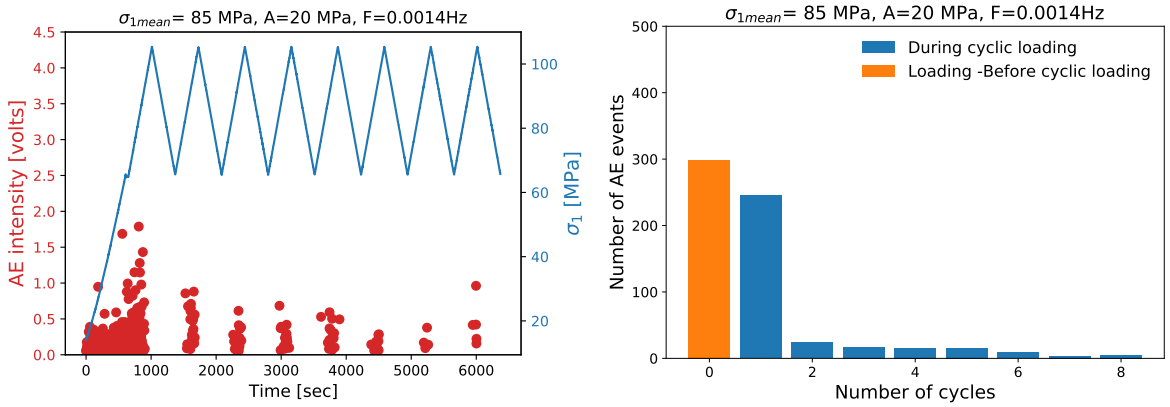


Figure 4.18: A typical result of acoustic emissions intensity (top) and number of acoustic events (bottom) obtained during deviatoric cyclic tests. Acoustic emissions were recorded right after increasing the deviatoric stress at the beginning of the test.

Considering the typical results of AE shown in figures 4.18 and 4.19, the main general observations for both studied regimes are:

- AE were recorded in both deformation regimes: Brittle and elastic.
- AE were recorded early in the first loading interval at axial stress slightly higher than the confining stress.
- In subsequent cycles, the AE started later but at a stress lower than the previous applied maximum stress, this is called Felicity effect. For instance, AE in in the brittle regime started at 90% of the maximum applied stress while in the elastic regime AE started at 77% of the maximum stress (figure 4.19-right).
- The maximum acoustic intensity and number of events were recorded in the first cycle.
- Subsequent cycles showed also AE events but with a much lower number of events and a decreasing trend.
- In general, the intensity decreased with the number of cycles. Nevertheless, isolated events with relatively high intensity were also recorded.

Results concerning the effect of deformation regime and frequency on intensity and number of AE events are shown in figures 4.20 and 4.21. With respect to AE's intensity, the brittle regime presents higher intensities than the elastic regime. This was the anticipated result, micro-fracturing in the brittle regime is expected to release larger amounts of elastic energy than any other mechanism presented at a stress lower than the brittle yield point, confirming that tests were run in different deformation regimes. Nevertheless, the release of acoustic emissions early in the elastic region was surprising because it was expected that inelastic deformations in this regime were able to trigger AE.

Regarding the effect of frequency on AE, the trend of AE events in the brittle regime is similar for frequencies F=0.014Hz and F=0.0014Hz while in the lowest frequency, the AE events concentrate in the first 4 cycles. For the elastic regime, the AE events are similar for the three tested frequencies. Nevertheless, the number of AE at the first cycle for the lowest frequency is smaller than in the other frequencies.

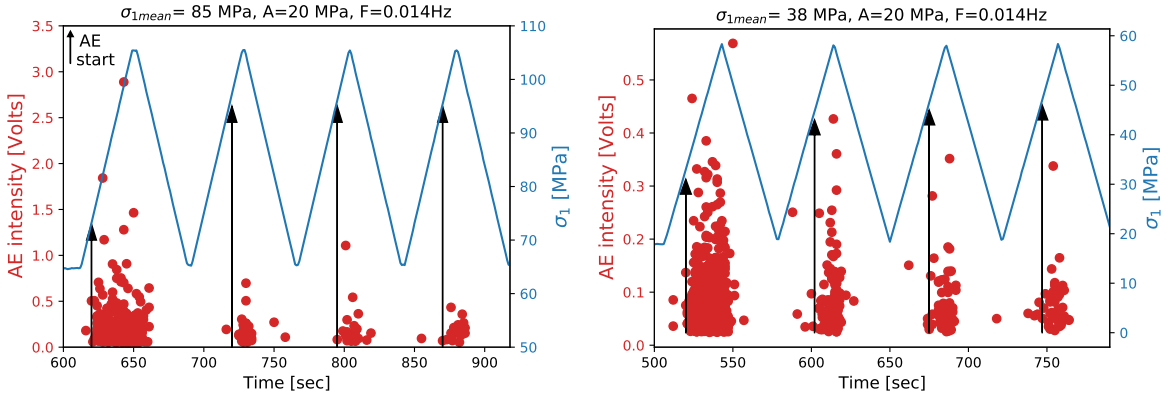


Figure 4.19: Approximated start of AE in every cycle for the first 4 cycles in high-frequency tests, for both deformation regimes: Brittle (left) and elastic (right). The start of AE are indicated with an arrow.

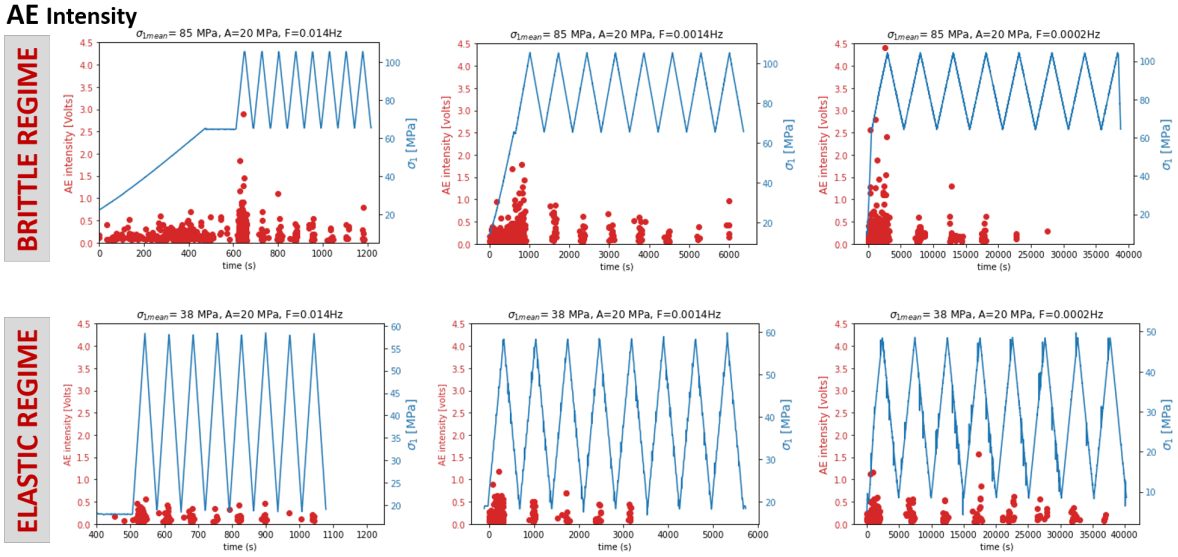


Figure 4.20: Comparison of AE's intensity for tests run in brittle (top) and elastic (bottom) regimes at different frequencies and fixed amplitude of 20MPa

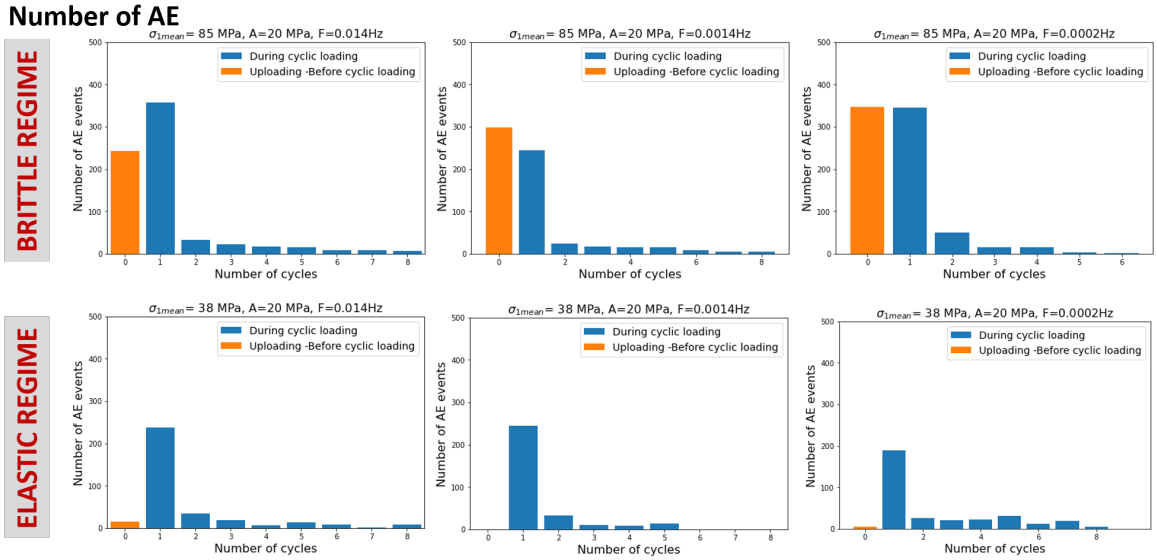


Figure 4.21: Comparison of the number of AE recorded for tests run in brittle (top) and elastic (bottom) regimes at different frequencies and fixed amplitude of 20MPa

### 4.6.7. Acoustic emissions and inelastic strains

Acoustic emissions are in most cases an indicator of inelastic strains as mentioned by Lockner, 1993. To validate this statement for Red Felser sandstone, an additional cyclic test was performed within the elastic regime. It consisted of a multilevel amplitude cyclic test, with fixed minimum deviatoric stress equal to zero, such as inelastic strain can be measured directly. A sequence of three amplitudes, with a decreasing-increasing trend, was imposed at a frequency of 0.014Hz.

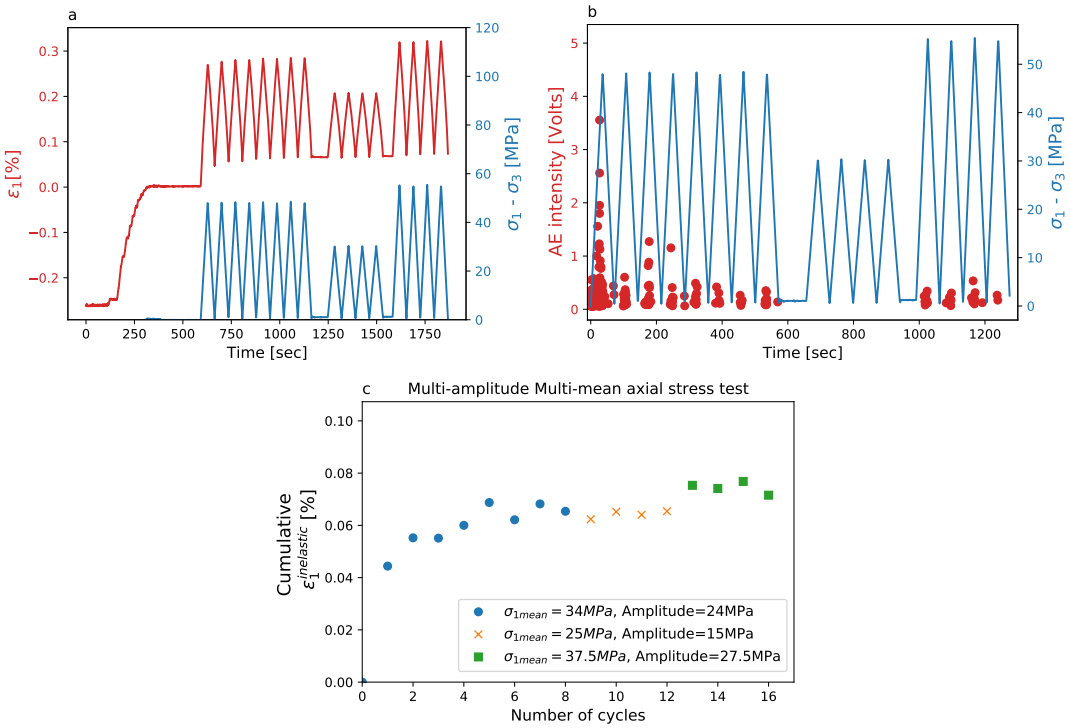


Figure 4.22: a. Stress and strain behavior for a deviatoric cyclic test under variable mean stress and amplitude at frequency 0.014Hz and $\sigma 3$=10MPa on Red Felser sandstone. b. Registered acoustic emission intensity. c. Cumulative inelastic strain versus the number of cycles. It can be seen that when the amplitude is reduced no inelastic strains or AE are generated.

Results are shown in figure 4.22. It can be seen that the initial cyclic loading, with a maximum deviatoric stress of 48MPa, generated inelastic strains and acoustic emission events just after increasing the deviatoric stress. Then, after 8 cycles the amplitude was reduced 1/3, during this condition no inelastic strain nor acoustic emissions were generated. Finally, the amplitude was increase 1.1 times the initial amplitude. The acoustic emissions were recorded once the deviatoric stress reached 40MPa. During this final cyclic condition more inelastic strains were generated. In addition, cumulative AE and inelastic strain show a linear correlation, as shown in figure 4.23, which indicates that there is a proportional relationship.

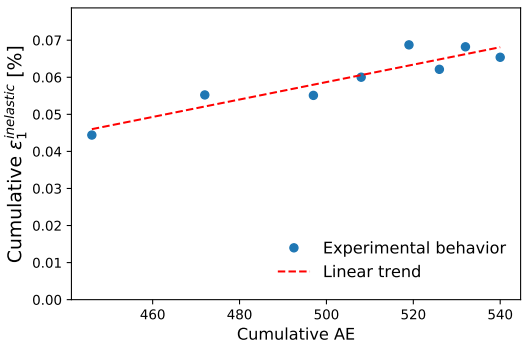


Figure 4.23: Cross plot of cumulative AE vs cumulative inelastic strain, which shows a linear correlation.

### 4.6.8. Brittle creep tests

A total of two creep tests were carried out above the brittle yield point ($\sigma_1$ upper elastic limit) to determine if the rock could experience brittle creep. The referential brittle yield point at 10 MPa confining pressure was 80MPa. The actual interpreted values for the 2 tested samples are described in table 4.7. It is essential to mention that for performing the tests; the equipment was left heating up for about 8 hours with a dummy sample and then 2 hours more with the rock sample. This was done in order to establish a steady temperature of the whole system. The resulting temperature of the cell's wall and bottom cell's piston was 26$C^\circ$ and 30$C^\circ$ respectively. In addition, switching the equipment off and on after the first 8 hours of heating resulted in better stress control (no stress spikes).

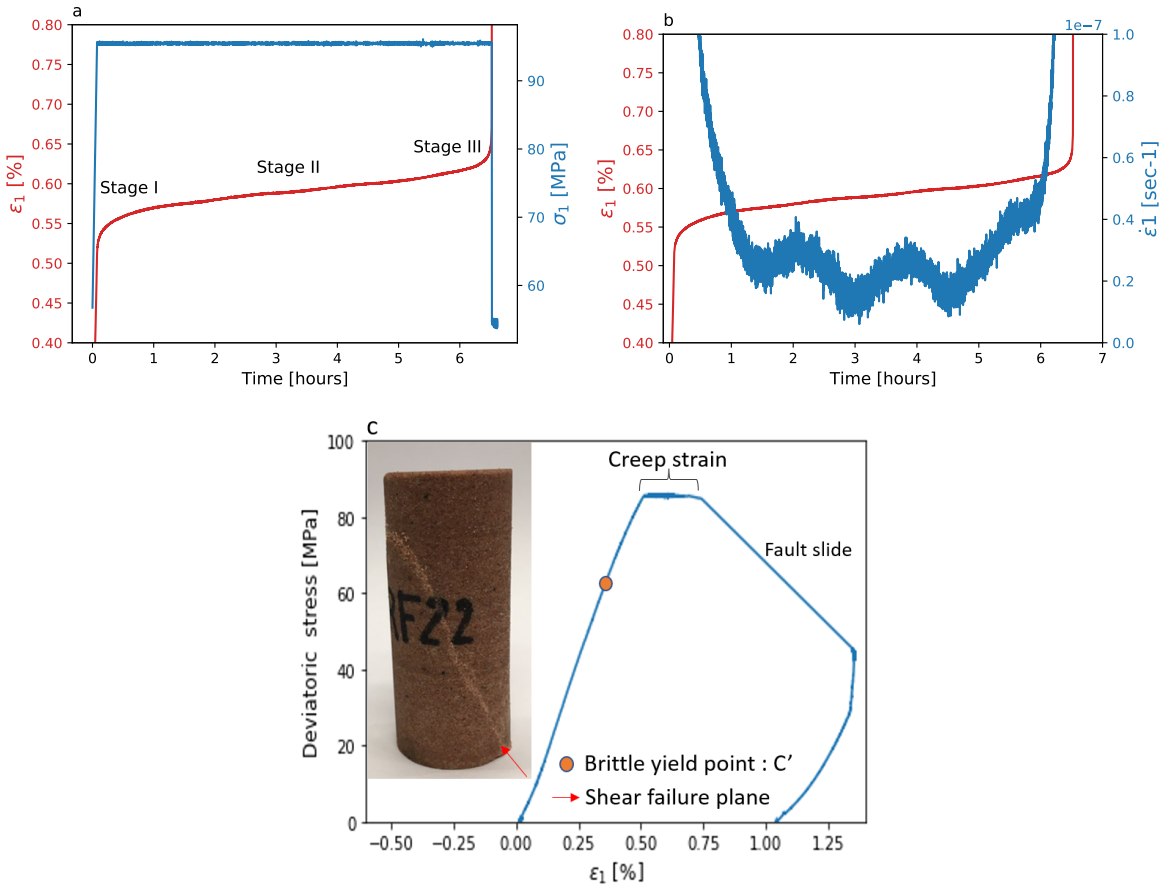


Figure 4.24: Result of single step brittle creep test at $\sigma_1$=95MPa and $\sigma_3$=10MPa. a: Stress and strain versus time indicating creep stages: decelerating (I), steady (II) and accelerating (III). b: Strain and strain rate versus time. c: Strain versus stress and sample photograph after creep failure

| Creep test | $\sigma_1$ steps [MPa] | Sample name | Temp. [$C^O$] | Brittle yield point [MPa] |
|---|---|---|---|---|
| 1 | 95 | RFD22 | 26 - 30 | 73 |
| 2 | 85 - 105 -115 | RFD9 | 26 - 30 | 83.4 |

Table 4.7: Brittle yield point ($\sigma_{yield}^{Brittle}$) for the samples tested under creep condition (Steps of constant loading). $\sigma_3 = 10MPa$

Results of the single-stage creep test for an axial stress of 95MPa, brittle yield point of 73MPa and constant confining pressure of 10MPa are shown in figure 4.24. It can be seen that the rock can de-

velop brittle creep. Indeed, it experienced the three phases of brittle creep: primary or deceleration, secondary or steady and tertiary or accelerating (Brantut et al., 2013). All these phases were covered during a period lower than 7 hours. Figure 4.24-c shows the rock sample after creep failure.

Based on the previous result, a multistage creep test was carried out following the next axial stress stages: 85.5MPa, 105.5 MPa and 115.5MPa. The test was switched to the next stage once secondary creep was reached in the current stage. Stress and strain results are shown in figure 4.25. It is quite remarkable that not all the creep strain is inelastic as can be seen in figure 4.25-right. The stress-strain curve determined a yield point of 83.4 MPa for the sample used in the multistage creep.

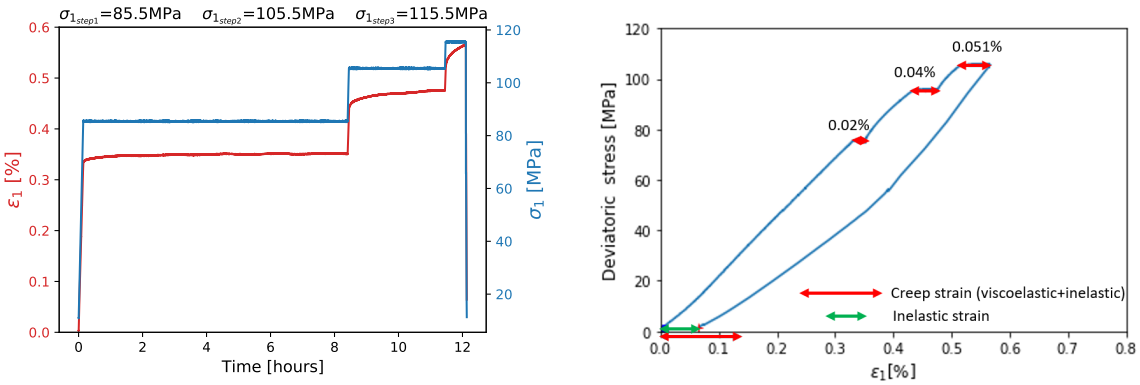


Figure 4.25: Axial strain behavior during multistage creep test: Strain versus time(left) and strain versus deviatoric stress (right). It can be seen that all creep strain is not inelastic.

Steady creep rates were plotted against deviatoric stress and effective brittle stress, as shown in figure 4.26. The effective brittle stress is the difference between the applied axial stress and the corresponding brittle yield point, which is used as a stress condition to model brittle creep using the Nishihara's model (see equation 3.16). It can be seen that when the strain rates from both tests are plotted against deviatoric stress, the two samples show different behavior. However, when strain rates are plotted versus effective brittle stress, the behavior of the two samples is more alike. The latter can be used to calibrate the brittle creep models.

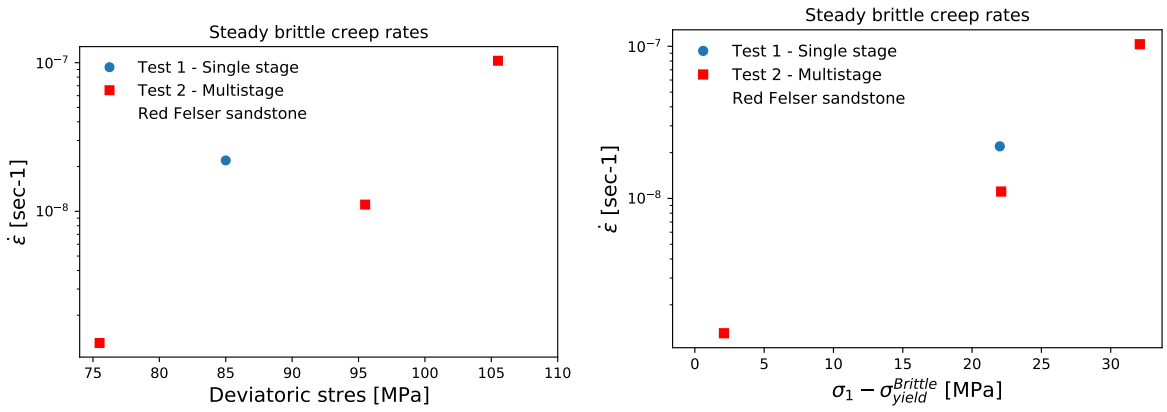


Figure 4.26: Steady creep rate results plotted versus deviatoric stress (left). Steady creep rate results plotted versus effective brittle stress "$\sigma_1$-$\sigma_{yield}^{Brittle}$" (right). Temperature 26$C^\circ$ - 30$C^\circ$ and $\sigma_3$=10MPa.

## 4.7. Discussion and interpretation of experimental results

The previous chapter reported experimental results regarding the effect of deformation regime (Elastic and Brittle), frequency and stress amplitude on the axial strain of Red Felser. Next, the possible reasons behind the obtained results is discussed.

### 4.7.1. Effect of deformation regime on inelastic strains

As expected, inelastic strains an AE were recorded when tests were carried out in the brittle regime (axial stresses higher than brittle yield point). This results from critical and/or sub-critical micro-cracks induced in the quartz grains, leading to irreversible changes in the rock micro-structure and the release of elastic waves. Interestingly, inelastic strain as well as AE were also recorded in the elastic regime (axial stresses lower than brittle yield point), where usually pure elastic strains are expected. Nevertheless, there is a difference in acoustic emission intensity and number of AE in between both regime at the same amplitude, as shown in figures 4.20 and 4.21. This indicates that different mechanisms are taking place. For instance, micro-cracking of quartz grains that take place above the brittle yield point is expected to release more energy than inter-granular cracking, clay crushing or grain sliding, which are the possible mechanisms below the brittle yield point.

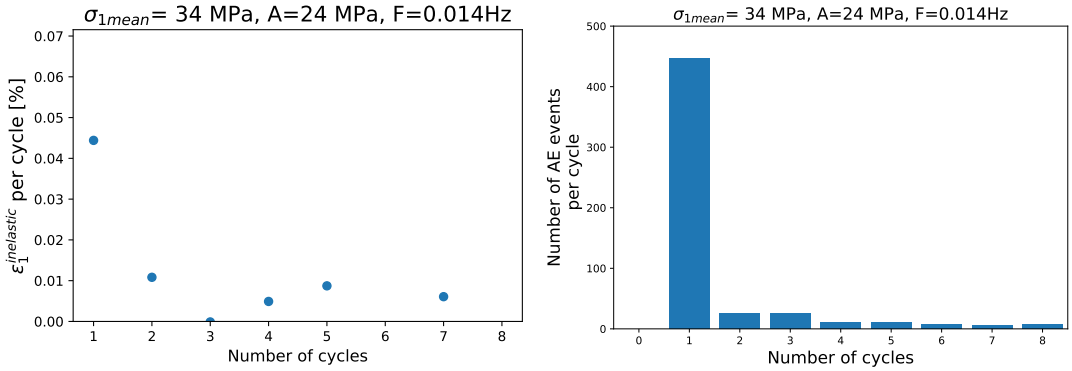


Figure 4.27: Inelastic strain (left) and number of AE (right) per cycle showing an exponential-like trend for constant amplitude tests.

**Elastic regime**

The inelastic strains were generated in every cycle and followed a decreasing rate per cycle as shown in figures 4.27-left, 4.12 and 4.13. This trend, that looks exponential, is also indicated by the number of AE per cycle as shown in figures 4.27-right and 4.21. This behavior means that the rock behaves more elastic as the number of cycles increases. AE also show that inelastic strains are taking place at very low deviatoric stresses in the first cycle, right above the initial hydrostatic condition of 10MPa as shown in figure 4.18. This could be considered a secondary yield point in addition to the brittle yield point.

The existence of inelastic deformations at low stress levels for sandstones has been also reported by Pijnenburg et al., 2019 and Gatelier et al., 2002. From the micro-structural point of view, inelastic strains in sandstones below the brittle yield point have been interpreted as irreversible rock compaction caused by crushing and slip of clay layers plus inter-granular cracking (Pijnenburg et al., 2018, Pijnenburg and Spiers, 2020 and Vermeer and de Borst, 1984). Red Felser sandstone is comprised of low volumetric proportions of clay and orthoclase grains that could crush or brake at stress levels lower than the onset for intra-granular cracking of quartz grains. Regarding, the cyclic inelastic strains, it has been related with the irreversible closure of induced and existing cracks (Cerfontaine et al., 2017). Nevertheless, additional inter-granular cracking is not discarded given the recording of AE, which are usually caused by brittle deformations.

From the macroscopic point of view, the inelastic deformation mechanism for sandstones at stresses below the brittle yield point has been explained by Pijnenburg et al., 2019 using the modified CAM-CLAY model (Roscoe and Burland, 1968). Within this framework, the inelastic strains were associated with isotropic plastic volumetric deformations (Inelastic compaction) induced after the stress state (q and p), reaches the yield surface. It is interpreted that a similar mechanism could be also taking place in Red Felser sandstone.

Nevertheless, plastic models like the standard modified CAM-CLAY model, do not explain the cyclic-inelastic strains and their exponential decrease with the number of cycles during constant cyclic loading. Because, these models consider that once the rock has been yielded, a new yield surface equivalent to the maximum applied stress state is defined. Thus, if the stress does not exceed the previous maximum stress, inelastic strains are not accumulated. Instead, it is interpreted within the plastic framework, that the yield surface does not fully spread until the maximum stress state in the first loading. Rather, the yield surface increases cycle after cycle, until eventually reaching the maximum applied stress. This is supported by the observation that AE during reloading intervals were triggered at a stress lower than the maximum stress (figure 4.19) as well as by the decreasing behavior of inelastic stress with respect to the cycles (figure 4.27).

**Brittle regime**

In the case of the tests performed in the brittle regime ($\sigma_{1meam}$=85 MPa), the main inelastic deformation during the first loading is related to dilatant cracking because the maximum axial stress was higher than the brittle yield point. A resume of the brittle yield points interpreted for the samples is shown in table 4.8. This stress condition triggers critical crack growth. Sub-critical cracking could be also taking place in low-frequency test (F=0.002Hz) because the sand grain could have been weakened by the water and there was sufficient time for the development of this mechanism (Brantut et al., 2013).

In addition, cyclic loading itself is inducing inelastic deformations as shown by both: the apparent inelastic strain and the acoustic emissions recorded cycle after cycle (figures 4.13 and 4.21 respectively). The mechanisms that could be playing a role in cyclic inelastic strains in the brittle regime are:

- Brittle creep, which is a time-dependent irreversible deformation caused by sub-critical micro-cracking, was recorded for Red Felser sandstone. In fact, this rock showed the three deformations stages that characterize creep, including creep rock failure (see figure 4.24). This mechanism is expected to be important as the frequency of the cyclic loading decreases.
- Irreversible closure of existing and induced micro-cracks due to grain sliding (Cerfontaine et al., 2017).

The importance of the mentioned cyclic inelastic mechanisms will be addressed during the evaluation of the constitutive models through simulation of the tests.

| Test condition | Sample name | Brittle Yield point [MPa] |
|---|---|---|
| $\sigma_{1mean}$1-F1-A1 | RFD5 | 77.5 |
| $\sigma_{1mean}$1-F2-A1 | RFD6 | 80 |
| $\sigma_{1mean}$1-F3-A1 | RFD7 | 81 |

| Test condition | Sample name | Brittle Yield point [MPa] |
|---|---|---|
| $\sigma_{1mean}$1-F1-A2 | RFD12 | 87.5 |
| $\sigma_{1mean}$1-F2-A2 | RFD16 | 85 |
| $\sigma_{1mean}$1-F3-A2 | RFD20 | no identified |

Table 4.8: Brittle yield point ($\sigma_{Yield}^{Brittle}$) for the samples tested under deviatoric cyclic stress in the brittle regime. $\sigma_3 = 10MPa$

## 4.7.2. Effect of Amplitude

It was noticed from experiments that the higher the amplitude the higher the inelastic axial strain as shown in figure 4.11, given that axial mean stress and frequency are constant. This result was as expected because the higher the amplitude the higher the maximum stress, which means that more inter-granular and intra-granular cracks are induced.

As was described in the chapter 4, one additional test was performed to study the effect of varying amplitude along a test in the elastic regime. Its results, shown in figure 4.22, indicated that if the amplitude is reduced then inelastic deformations are not accumulated and AE are not generated. This can be explained within the framework of plasticity previously discussed. For instance, if the amplitude

of a cyclic test is decreased, such as the maximum stress condition is within the pre-established yield function, then the rock will behave purely elastic as a result of the previous cyclic compaction condition. Inelastic deformation will be triggered again, once the amplitude is increased and the corresponding stress path reaches the pre-established yield surface. Then, depending on the stress history, changes in stress amplitude could or could not induce inelastic strains.

### 4.7.3. Young's modulus behavior

It was shown that Young's modulus computed in the loading ramps of the cycles increased significantly from the first cycle to the second cycle independently of the regime (see figures 4.16, 4.17). This is the result of the important inelastic strains accumulated in the first loading, which also match the behavior of AE and strain rate in the loading interval as shown in figure 4.28. Thus, the Young's modulus measured in the first ramp or loading is an apparent value because its estimation includes the inelastic strains. This was also pointed out by Pijnenburg et al., 2018. Accordingly, the estimated Young's modulus from reloading and unloading intervals is expected to be closer to the real value, because inelastic strains are small (reloading) or null (unloading).

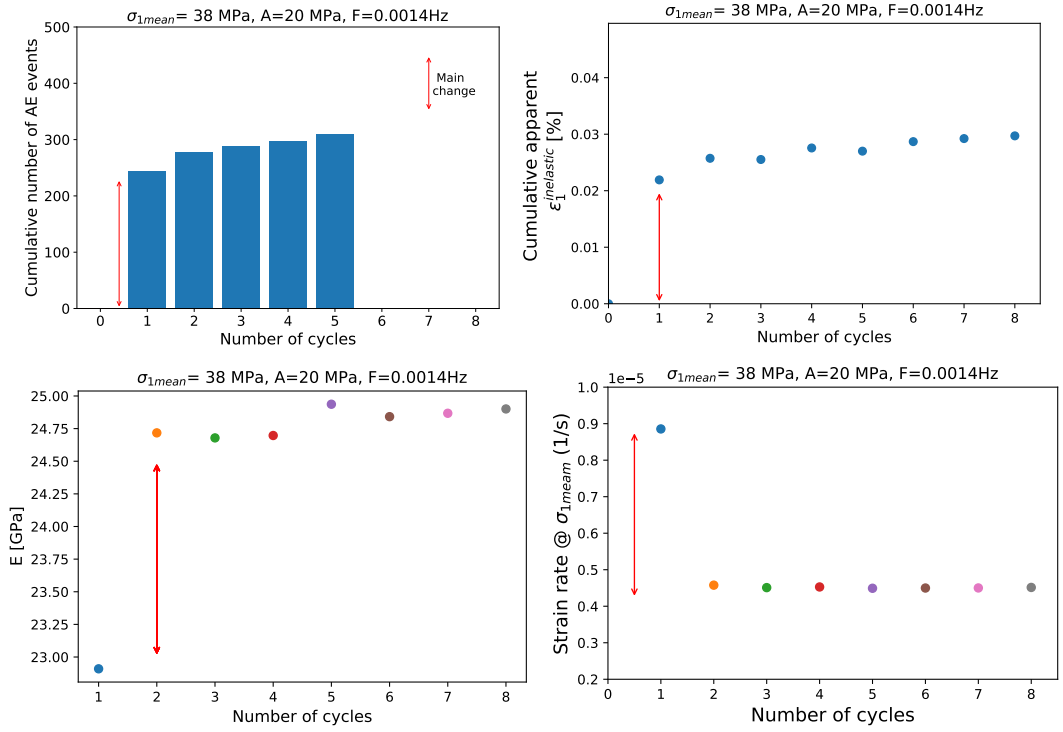


Figure 4.28: Relationship between acoustic emission (top-left), apparent inelastic strain (top-right), Young's modulus (bottom-left) and strain rate at the mean stress of loading and reloading intervals (bottom-right) for a test in the 'elastic regime'. The red arrow indicates the main jump in every response.

In addition, Young's modulus estimation in loading and reloading intervals could be also influenced by time-dependent deformation, like visco-elasticity. Evidence, to be discussed in the next point, suggest that this deformation mechanism is operating during Red Felser triaxial and cyclic tests. This mechanism delays the elastic deformation, making the rock appear stiffer. This can be interpreted from the Kelvin-Voigt unit model represented in equation 4.9. For instance, when time t is lower than the ratio between viscosity $\eta_1$ and Young's modulus E, then the strain is smaller than total elastic strain. On top of that, the apparent Young's modulus estimated in the reloading intervals of the tests in the brittle regime are higher than those in the elastic regime as shown in figure 4.17. This is probably because visco-elastic viscosity is a function of differential stress. The higher the stress the higher the friction the lower the viscosity as happens with creep viscosity (Z. Chen et al., 2022).

$$\epsilon_1 = \frac{q}{E}(1 - e^{-\frac{t}{\frac{\eta_1}{E}}}) \tag{4.9}$$

### 4.7.4. Time dependent strains and frequency

Next, it will be discussed if elastic and inelastic deformations were affected by time and subsequently by frequency during the execution of deviatoric cyclic tests.

**Elastic strains**

Several deformation features suggest that visco-elasticity is one of the time-dependent mechanisms presented in Red Felser sandstone, independent of the deformation regime (brittle or elastic). These features are:

- Not all the creep deformation in brittle creep tests were inelastic as shown in figure 4.25-right.
- Loading and unloading stress-strain curves have hysteresis with convex unloading curves as shown in figure 4.29.
- Strain versus time curves in cyclic loading tests shown non-linear behavior as shown in figure 4.10.

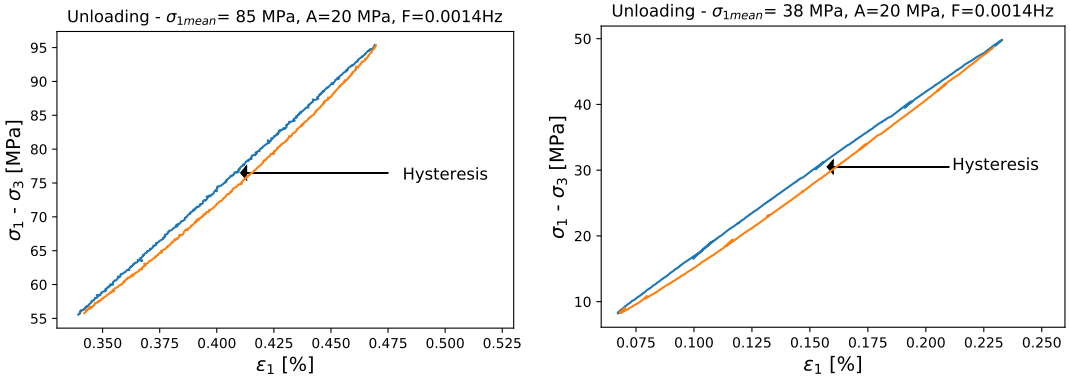


Figure 4.29: Loading and unloading strain-stress curves for the 8th cycle in 2 cyclic test corresponding to both regimes: Brittle (left) and elastic(right).

**Inelastic strains**

For the Red Felser sandstone, it is clear that the rock can experience time dependent inelastic deformations when the stress is above the brittle yield point. This was proven by the results of the creep tests (see figures 4.24 and 4.24) and by the effect of frequency on apparent inelastic strain during deviatoric cyclic tests (see figure 4.14-left). This deformation mechanism is called **brittle creep** (Brantut et al., 2013).

It was shown in figure 4.11, that inelastic deformation in the elastic regime was also affected by frequency (the smaller the frequency the larger the inelastic strain). Then, there could be a time-dependent deformation mechanism playing a role. However, when the apparent strain of the first cycle was removed from the cumulative apparent inelastic strain, the effect of frequency is not obvious (figures 4.14 and 4.15). This suggests that the time-dependent deformation in the elastic regime could be relevant for short times (minutes time scale). It is recommended to perform longer tests to validate this interpretation.

# 5

# Modeling of cyclic loading experiments

## 5.1. Proposed constitutive model for cyclic loading

Based on the interpretation and stress conditions of the experimental test, the next deformation mechanisms were identified or are expected to be taking place during cyclic deformation of Red Felser sandstone:

- Elastic deformation.
- Visco-elastic deformation (also known as elastic creep).
- Compacting plastic and cyclic-plastic deformation (below the brittle yield point).
- Dilating plastic deformation (above the brittle yield point).
- Brittle creep.

A constitutive model that could take into account some of the described mechanisms is Nishihara's constitutive model (equation 3.16). Nevertheless, it may require a modification to account for plastic and cyclic plastic deformation. Here, it is proposed the inclusion of plastic models into the Nishihara constitutive model, under the premise that the strains can be decomposed into elastic and inelastic strains (equation 5.1) and those inelastic strains are independent of each other. The general integrated model, solved for axial strains under triaxial conditions, is presented in equation 5.1.1 and illustrated in figure 5.1. In this model, only steady creep is considered.

$$\epsilon^{total} = \epsilon^{elastic} + \epsilon^{plastic} + \epsilon^{BrittleCreep} \tag{5.1}$$

$$\epsilon_{total}(t) = \begin{cases} \frac{q}{E_1} + \frac{q}{E_2}(1 - \exp -\frac{E_2}{\eta_1}t) + f_1(q, \alpha_i)] & \text{if } \sigma_1 < \text{Brittle yield point} \\ \frac{q}{E_1} + \frac{q}{E_2}(1 - \exp -\frac{E_2}{\eta_1}t) + f_2(q, \beta_i) + \frac{\sigma_1 - \sigma_{yield}^{Brittle}}{\eta_2}\Delta t_{creep} & \text{if } \sigma_1 > \text{Brittle yield point} \end{cases} \tag{5.2}$$

Where:

- $q = \sigma_1 - \sigma_3$
- $\Delta t_{creep}$:Brittle creep effective time $\sigma_{yield}^{Brittle}$:Brittle yield point
- $E_1$= Young's modulus of the spring unit. $E_2$= Young's modulus of the Kelvin-Voigt unit.
- $\eta_1$= Viscosity of the Kelvin-Voigt unit. $\eta_2$= Viscosity of the brittle creep unit.
- $f_1(q, \alpha_i)$ and $f_2(q, \beta_i)$: General representation of the so far unknown plastic functions
- $\alpha_i, \beta_i$: inelastic cyclic parameters for cycle 'i'

The average Young's modulus of the model is described by equation 5.3, after considering infinite time.

$$E_{avg} = \frac{E_1 E_2}{E_1 + E_2} \tag{5.3}$$

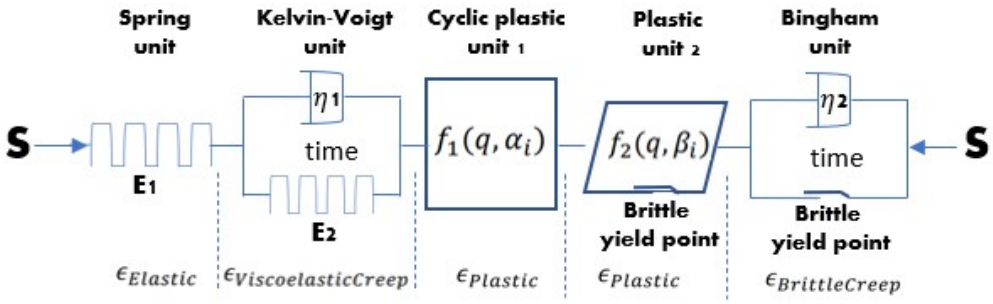


Figure 5.1: Graphical representation of proposed deformation model for cyclic loading in sandstones.

To complete the model, it is required to define the functions $f_1(\sigma_1, \alpha_i)$ and $f_2(q, \beta_i)$ of equation 5.1.1. The function $f_1(\sigma_1, \alpha_i)$ is intended to model rock inelastic cyclic compaction below the brittle yield point while the function $f_2(q, \beta_i)$ takes into account only dilatant inelastic strains above the brittle yield point in the first loading, i.e. cyclic inelastic strains due to dilation are not considered in this work. Nevertheless, there are models for dilatant cyclic loading (Cerfontaine et al., 2017 and Vermeer and de Borst, 1984) but were found too complex for implementation. Thus, the total plastic strain when the rock is subjected to a stress condition above the brittle yield point is described with equation 5.4. It is important to mention that compaction refers to the reduction of the rock pore volume while dilation means the increase in pore volume due to shear cracks generation and aperture.

$$\epsilon^{plastic} = \epsilon^{plastic_{compaction}} + \epsilon^{plastic_{dilation}} \tag{5.4}$$

### 5.1.1. Modified Cambridge-Clay 'MCC' model for cyclic loading

The modified Cambridge-clay model, also known as **MCC**, was developed during the '60s for modeling plastic strains in wet clays (Roscoe and Burland, 1968). The model is based on both: a yield surface that determines whether the solids behave elastic or inelastic and a critical state line (CSL) that defines the failure of the material and the corresponding softening or hardening behavior, as shown in figure 5.2. The MCC has been proposed to model isotropic inelastic compaction of sandstones, caused by intergranular cracking, clay crushing and grain sliding (Pijnenburg et al., 2019). These mechanisms mainly take place below the brittle yield point. Here, this proposal is also adopted. In addition, it is proposed an extension of the MCC to account for cyclic inelastic strain inspired by the work done by (Carter et al., 1979). Thus, the MCC model corresponds to the function $f_1(\sigma_1, \alpha_i)$ in equation 5.1.1 and accounts for cyclic inelastic compaction.

The mathematical representation of the yield surface in 'p' and 'q' space is shown in equation 5.5 when 'f' is equal to zero. Here, $p_c$ is the pre-consolidation parameter, which is equivalent to the yield point in hydro-static stress path and $M$ is the slope of the critical state line. When the stress state is increased such as 'f' is equal to or higher than zero, then there is generation of inelastic strain. If 'f' is lower than zero, only elastic strains take place.

$$f = q^2 - M^2(p(p_c - p)) \tag{5.5}$$

$$f \geq 0 \rightarrow \text{plastic strains}$$

$$f < 0 \rightarrow \text{elastic strains}$$

While yielding the rock, a new yield surface is created, which happens to be the same as the maximum applied loading surface ($p_c^{new} = p_l^{maximum}$), following equation 5.6 (Carter et al., 1979). A loading

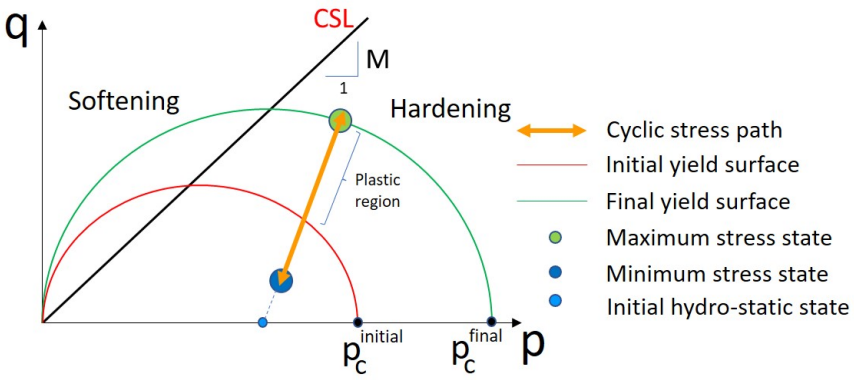


Figure 5.2: Graphical representation of MCC model in the q - p space. It is also shown that under constant amplitude cyclic loading, a new yield surface that contains the maximum applied stress state, is established in the first unloading. Thus, the subsequent constant stress amplitude cycle will not generate further inelastic strains.

surface is a mathematical representation of the stress state using the yield surface framework, where $p_l$, defined with equation 5.7, is the loading parameter that allows the construction of the loading surface described in equation 5.8.

$$\frac{\delta p_c}{p_c} = \frac{\delta p_l}{p_l} \tag{5.6}$$

$$p_l = p^{state} + \frac{{q^{state}}^2}{M}\frac{1}{p^{state}} \tag{5.7}$$

$$0 = q^2 - M^2(p(p_l - p)) \tag{5.8}$$

Where $p^{state}$ and $q^{state}$ define the applied stress state.

The changes in volumetric and shear plastic strains and void ratio 'e', described by equations 5.9,5.10 and equation 5.11 respectively, are computed based on the changes of stresses p and q right above the yield surface, as shown in equation 5.12. For the MCC formulation, compression is considered positive.

$$dV^{plastic} = \epsilon_1^{plastic} + 2\epsilon_3^{plastic} \tag{5.9}$$

$$d\epsilon_{shear}^{plastic} = \epsilon_1^{plastic} - \epsilon_3^{plastic} \tag{5.10}$$

$$de = -(1+e) * dV^{plastic} \tag{5.11}$$

$$\begin{bmatrix} dV^{plastic} \\ d\epsilon_{shear}^{plastic} \end{bmatrix} = \Omega * \begin{bmatrix} M^2 - \eta & 2\eta \\ 2\eta & \frac{2\eta}{M^2 - \eta^2} \end{bmatrix} * \begin{bmatrix} dp \\ dq \end{bmatrix} \tag{5.12}$$

Where:

$$\Omega = \frac{\lambda_{MCC} - \kappa}{(1+e)p(M^2+\eta^2)}, \kappa = \frac{1+e}{\mathrm{K}}, \mathrm{K} = \frac{E_{avg}}{3(1-2v)}$$

$$\eta = \frac{q}{p}, e = \frac{\phi}{1-\phi}, \phi\text{:porosity, } e\text{:void ratio}$$

Based on the MCC model, inelastic strains during cyclic loading will only generate if the stress state goes beyond the maximum already applied stress state '$p_l^{max}$'. Nevertheless, it was seen in the constant amplitude cyclic experiments that inelastic strains are generated cycle after cycle (figures 4.28

and 4.22). On top of that, the amount of inelastic strain reduces as the number of cycles increases, which means that the rock behaves more elastic. This trend is expected to continue for cyclic conditions below the brittle yield point at least. Thus, to model this behavior with the MCC model, here it is proposed that during the loading periods, a new pre-consolidation parameter $p_c^{new}$ is established cycle after cycle. The evolution of the pre-consolidation parameter is ruled by equation 5.13 and equation 5.14 after integration. This $p_c^{new}$ is lower than $p_l^{max}$ but as the number of cycles increases $p_c^{new}$ tends to the value of $p_l^{max}$. In equations 5.13 and 5.14, $\theta$ is the cyclic parameter that depends on the cyclic inelastic strain response of the sandstone under constant amplitude cyclic loading. Its value can be equal to or lower than 1. If $\theta$ is equal to 1, the model reduces to the standard MCC. $p_c^{new}$ is equivalent $\alpha_i$ define in equation . This proposal is inspired by the work of Carter et al., 1979 et al., which dealt with the deformation of clays under cyclic loadings. In their case, the amount of inelastic strain increases cycle after cycle, thus the yield function shrinks. Which is the opposite behavior to that observed for the Red Felser sandstone.

$$\frac{\delta p_c}{p_c} = \theta \frac{\delta p_l}{p_l} \tag{5.13}$$

$$p_c^{new} = p_c^{old} \left( \frac{p_l^{max}}{p_c^{old}} \right)^{\theta} \tag{5.14}$$

where $p_l^{max} > p_l^{old} = p_c^{old}$ (point where plasticity takes place).

The main characteristics of the proposed modification of the MCC model are:

- If $\theta$ is equal to 1, the model reduces to the standard MCC model.
- if $\theta$ is lower than 1 cyclic inelastic strains are generated.
- As the number of cycles increases $p_c^{new}$ becomes closer to $p_l^{max}$. Thus, cyclic inelastic strains reduce cycle after cycle.
- Unloading behaves elastically.
- The shape of the yield function remains the same (an ellipse).

### 5.1.2. Hardening softening model

To model the plastic strains induced by the fracturing of the sand grains, the hardening-softening model, developed by Vermeer and de Borst, 1984 was adopted. It follows the general rule that during plasticity the total strain rate '$\dot{\epsilon}$' can be decoupled in an elastic '$\dot{\epsilon}^{elastic}$' and plastic '$\dot{\epsilon}^{plastic}$' contribution. This model is intended to partially cover the proposed function $f_2(q, \beta_i)$ in equation 5.1.1. Nevertheless, there was not devised modification to this model to account for possible cyclic inelastic strains caused by intra-granular cracking. Vermeer and de Borst, 1984 suggested a special framework for cyclic loading based on the bonding surface concept that could be explored in future research projects. It is worth to mention, that the hardening-softening model is able to forecast the rock peak strain and after peak stress behavior.

Here, a brief explanation of the model will be given. For a deeper understanding, the reader is referred to Vermeer and de Borst, 1984 and de Borst, 1987 articles. The model for triaxial conditions ($\sigma_3 = \sigma_2$) is based on Coulomb-Mohrs yield surfaces $f_1$ and $f_2$ (equations 5.15 and 5.16), which dictate when inelastic strains take place. These surfaces, which vanish simultaneously when the stress state reaches them, are a function of the friction angle $\phi_{friction}$ and cohesion of the rock $c$. The friction angle is the average inclination of shear fracture planes with respect to its normal while cohesion is the shear force required to reach failure of the rock when normal stress is zero. Here, compression is considered negative.

$$f_1 = \frac{1}{2}(\sigma_3 - \sigma_1) + \frac{1}{2}(\sigma_1 + \sigma_3) sin(\phi_{friction}) - c * cos(\phi_{friction}) = 0 \tag{5.15}$$

$$f_2 = \frac{1}{2}(\sigma_2 - \sigma_1) + \frac{1}{2}(\sigma_1 + \sigma_2)sin(\phi_{friction}) - c * cos(\phi_{friction}) = 0 \tag{5.16}$$

Similar surfaces are defined for the plastic potential flow, as can be seen in equations 5.17 and 5.18. In these plastic potential surfaces, $\psi$ is the dilation angle. When the dilation angle is equal to the friction angle, it is said that there is associated plasticity. If the dilation angle is lower than the friction angle, then there is non-associated plasticity. The latter behavior is adopted in this formulation.

$$g_1 = \frac{1}{2}(\sigma_3 - \sigma_1) + \frac{1}{2}(\sigma_1 + \sigma_3)sin(\psi) + constant \tag{5.17}$$

$$g_2 = \frac{1}{2}(\sigma_2 - \sigma_1) + \frac{1}{2}(\sigma_1 + \sigma_2)sin(\psi) + constant \tag{5.18}$$

These plastic potential functions ($g_1$ and $g_2$) are responsible of the magnitude of the plastic strains increments '$\dot{\epsilon}^{plastic}$', as can be seen in the general plasticity rule depicted by equation 5.19 as well as in equations 5.20 and 5.21 for axial and volumetric plastic strains respectively.

$$\dot{\epsilon}^{plastic} = \lambda_1 \frac{\delta g_1}{\sigma} + \lambda_2 \frac{\delta g_2}{\sigma} \tag{5.19}$$

$$\dot{\epsilon}_1^{plastic} = \frac{1}{2}(\lambda_1 + \lambda_2)(-1 + sin(\psi)) \tag{5.20}$$

$$\dot{\epsilon}_v^{plastic} = (\lambda_1 + \lambda_2)sin(\psi) \tag{5.21}$$

In the previous equations, $\lambda_1$ and $\lambda_2$ are the plastic multipliers. These parameters will be defined after introducing the rules for hardening and softening. These rules are: The rock is considered to start with a friction angle of zero, the dilation angle is lower than the friction angle and the initial cohesion is higher than zero. Then, as plastic strains are accumulated, the friction and dilation angle increase and cohesion decreases following equations 5.22,5.23 and 5.24 respectively. These variable angles and cohesion are known as mobilised friction angle '$\phi^*_{friction}$',mobilised dilation angle '$\psi^*_{friction}$' and mobilised cohesion '$c^*$'.

$$sin(\phi^*_{friction}) = \frac{\sqrt{\bar{\epsilon}^{plastic}\epsilon^f}}{\bar{\epsilon}^{plastic} + \epsilon^f} sin(\phi_{friction}) \tag{5.22}$$

$$sin(\psi^*_{friction}) = \frac{sin(\phi^*_{friction} - sin(\phi_{CV}))}{1 - sin(\phi^*_{friction} * sin(\phi_{CV})} \tag{5.23}$$

$$c^* = c \exp - \left(\frac{\bar{\epsilon}^{plastic}}{\epsilon^c}\right)^2 \tag{5.24}$$

Where '$\bar{\epsilon}^{plastic}$', which is the hardening parameter, is defined by equation 5.25 and indicates plastic strain accumulation. $\epsilon^f$ is a constant that defines when the mobilised friction angle becomes equal to the friction angle,$\epsilon^c$ controls the loss of cohesion and $\phi_{CV}$ is a constant called 'friction angle of constant volume' defined by equation 5.26.

$$\bar{\epsilon}^{plastic} = \int \sqrt{\frac{2}{3}(\dot{\epsilon}_1^{plastic}\dot{\epsilon}_1^{plastic} + \dot{\epsilon}_2^{plastic}\dot{\epsilon}_2^{plastic} + \dot{\epsilon}_3^{plastic}\dot{\epsilon}_3^{plastic})}dt \tag{5.25}$$

$$sin(\phi_{CV}) = \frac{sin(\phi) - sin(\psi)}{1 - sin(\phi)sin(\psi)} \tag{5.26}$$

After the previous definitions, it is possible to present the plastic multipliers $\lambda_1$ and $\lambda_2$ through the equations 5.27 and 5.28. As can be seen, it is not a trivial task to compute these numbers, because most of the terms are derivatives expressed in scalar, vector and matrix formats. In order to ease its implementation for future works, a description of these terms can be found in the appendix B.

$$\lambda_1 = \frac{\mu_4 \left(\frac{\delta f_1}{\delta \sigma}\right)^T D\dot{\epsilon} - \mu_2 \left(\frac{\delta f_2}{\delta \sigma}\right)^T D\dot{\epsilon}}{\mu_1\mu_4 - \mu_2\mu_3} \tag{5.27}$$

$$\lambda_2 = \frac{\mu_1 \left(\frac{\delta f_2}{\delta \sigma}\right)^T D\dot{\epsilon} - \mu_3 \left(\frac{\delta f_1}{\delta \sigma}\right)^T D\dot{\epsilon}}{\mu_1\mu_4 - \mu_2\mu_3} \tag{5.28}$$

Where $\mu_1$,$\mu_2$,$\mu_3$ and $\mu_4$ are define as:

$$\mu_1 = \left(-\frac{\delta f_1}{\delta \bar{\epsilon}^{plastic}} \frac{\delta \bar{\epsilon}^{plastic}}{\delta \epsilon^{plastic}} + D\frac{\delta f_1}{\delta \sigma}\right)^T \frac{\delta g_1}{\delta \sigma} \tag{5.29}$$

$$\mu_2 = \left(-\frac{\delta f_1}{\delta \bar{\epsilon}^{plastic}} \frac{\delta \bar{\epsilon}^{plastic}}{\delta \epsilon^{plastic}} + D\frac{\delta f_1}{\delta \sigma}\right)^T \frac{\delta g_2}{\delta \sigma} \tag{5.30}$$

$$\mu_3 = \left(-\frac{\delta f_2}{\delta \bar{\epsilon}^{plastic}} \frac{\delta \bar{\epsilon}^{plastic}}{\delta \epsilon^{plastic}} + D\frac{\delta f_2}{\delta \sigma}\right)^T \frac{\delta g_1}{\delta \sigma} \tag{5.31}$$

$$\mu_4 = \left(-\frac{\delta f_2}{\delta \bar{\epsilon}^{plastic}} \frac{\delta \bar{\epsilon}^{plastic}}{\delta \epsilon^{plastic}} + D\frac{\delta f_2}{\delta \sigma}\right)^T \frac{\delta g_2}{\delta \sigma} \tag{5.32}$$

To finish, it is important to mention the next comments: If the model is solved in strain steps, it is possible to model the hardening and softening behaviors but if stress steps are used, only hardening can be modeled. The latter is the scheme used in this thesis. In addition, the use of this model is intended to calculate plastic dilation because compaction is modeled with the MCC model. Then, it was only considered the strains generated when the friction angle is larger than the friction angle of constant volume ($\phi^*_{friction} > \phi_{CV}$), which is equivalent to a positive mobilised dilation angle. This condition defines the beginning of dilatant behavior in this model (Vermeer and de Borst, 1984).

## 5.2. Modeling the constitutive equations

Modeling of the deviatoric cyclic tests was carried out through the use of the analytical solution of the modified Nishahara's constitutive model proposed in equation 5.1.1. The model was implemented in python. It counts with four modules for the estimation of visco-elastic, brittle creep and plastic strains. Plastic strains are estimated through modified Cam-Clay model for stresses below the yield point and the hardening-softening model is used for stress above the brittle yield point. The inelastic strains are considered independent of each other in the proposed model. Failure due to fatigue or/and creep is not modeled.

Given that the analytical solutions for visco-elasticy and creep for triaxial conditions are developed for constant deviatoric stresses 'q', the principle of superposition (depicted in equation 5.33) was applied to account for the cyclic variation of 'q' during the tests (Kelly, 2013). This can be done because these analytical solutions are linear. Here, 'n' is the total number of stress steps, 'i' is a certain stress step, $\tau_i$ is the time when a stress step 'i' is applied and J(t) is the compliance of the rock. For example, the compliance of linear creep is $\frac{t}{\eta_2}$. A sample of the code is provided in appendix C.

$$\epsilon_1(t) = q(0)J(t) + \sum_{i=1}^{n} \Delta q J(t - \tau_i) \tag{5.33}$$

The mentioned modules are controlled by deviatoric stress stepping scheme, while $\sigma_2$ and $\sigma_3$ are considered constant and equal (triaxial conditions). For the hardening model, derivative and multiplier parameters at stress step 'n' were based on data on step 'n-1'. It was found that the model shows instabilities for a certain group of input parameters. This was partially overcome by reducing the stress step size. Probably, an iterative process around total strain rate '$\dot{\epsilon}$' could improve stability.

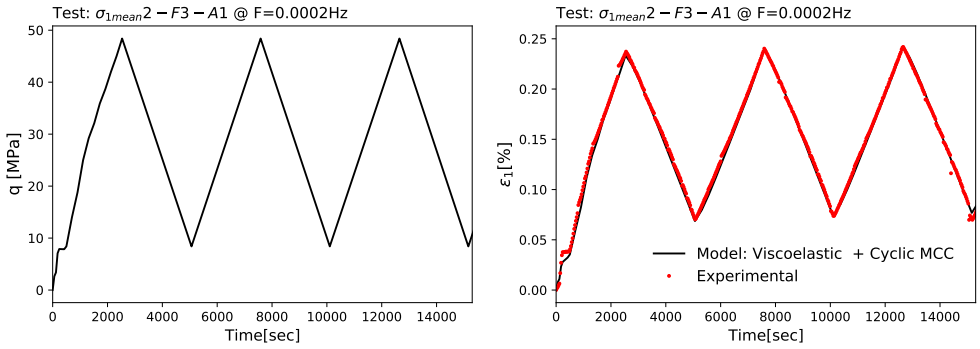


Figure 5.3: Imposed deviatoric stress condition for the first three cycles (left) and corresponding model versus experiment strain results. Test: $\sigma_{1mean}2 - F3 - A1$ at $\sigma_3$ = 10 MPa.

### 5.2.1. Modeling elastic regime cyclic tests

The process of fitting the model against experimental tests was as follows:

- First, an initial estimation of the Young's modulus was carried out using data from the first loading.
- Then, the total experimental inelastic strains after 8 cycles was reproduced using the Cyclic MCC model. For this step, the plastic multiplier ($\lambda_{MCC}$) and cyclic ($\theta$) parameters were fine tuned. As a reference for the fine-tuning process, the model results were also compared with experimental inelastic axial strain computed for every cycle. The latter was estimated based on the number of acoustic events per cycle ($AEevents_i$) and the measured total inelastic strain after 8 cycles ($\epsilon_{Total}^{Inelastic}$), under the premise that the number of AE correlates with the amount of inelastic strains as shown in chapter 4 and stated by Lockner, 1993.
- Finally, the viscoelastic plus Cyclic model is run and the Young's modulus and viscoelastic viscosity are fine-tuned. If Young's modulus is updated, the process is repeated again.

$$\epsilon_1^{Inelastic_i} = \frac{AEevents_i}{AEevents_{Total}} * \epsilon_{Total}^{Inelastic} \tag{5.34}$$

**General model response**

Tests with the highest amplitude (A1 = 20 MPa) were modeled. Figures 5.3 and 5.4-left show the response of the model versus experimental results, which corresponds to the longest test (lowest frequency) named as: $\sigma_{1mean}2 - F3 - A1$. The remaining simulated tests are shown in appendix D. In these figures, it can be seen that the model captures the increasing trend of the minimum strain cycle after cycle, as well as the non-linear loading and unloading intervals. The latter trend is justified by visco-elasticity and a small contribution of plastic strains.

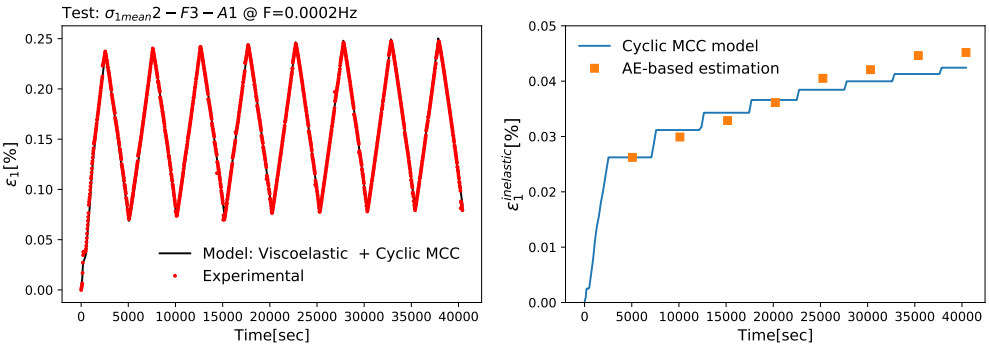


Figure 5.4: Model versus experimental result (left). Evolution of inelastic axial strain versus estimated inelastic strain from acoustic emissions 'AE' (right). Test: $\sigma_{1mean}2 - F3 - A1$ at $\sigma_3$ = 10 MPa.

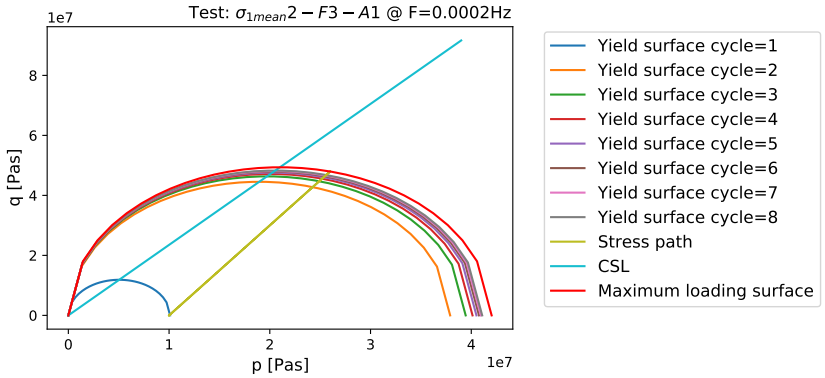


Figure 5.5: Evolution of the yield surface cycle after cycle based on the proposed model assumptions. Test: $\sigma_{1mean}2 - F3 - A1$ at $\sigma_3$ = 10 MPa.

In figure 5.4-right, it is shown how the inelastic strain increases cycle after cycle, based on the proposed model. This prediction follows the same trend that the experimental inelastic strain. As can be inferred from these results, the increment of inelastic strain per cycle will tend to zero as the number of cycles increase, which means that the rock will not accumulate any plastic strains due to cyclic loading. This is the result of assuming a spreading yield surface that eventually will be equal to the maximum loading surface when constant amplitude cyclic conditions are applied. Figure 5.5 shows the evolution of these yield surfaces, where the initial surface corresponds to a pre-consolidation parameter '$p_c$' equivalent to the initial hydro-static condition of 10 MPa. The latter is based on the experimental fact that acoustic emissions, a response of brittle inelastic strains, were recorded from the beginnings of the tests (figure 4.21).

For all the tests in the elastic regime, the Cyclic MCC model forecasts a reduction of porosity per cycle equivalent to a variation of 0.1% after 8 cycles, as shown in figure 5.7. In addition, the model

is able to reproduce the experimental trend of the Young's modulus as shown in figure **??**. It can be seen that the model can forecast the increase in Young's modulus from the first to the second cycle as estimated from the experiments. Then, the Young's modulus remains almost constant in the model with a value close to the real input Young's modulus. The experimental results are unstable due to experimental errors and instabilities.

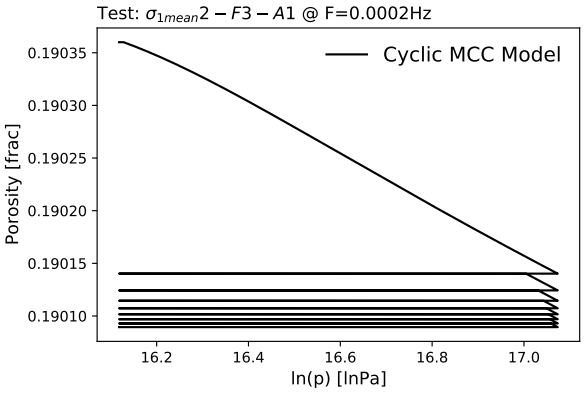


Figure 5.6: Forecast of porosity behavior versus pressure based on the proposed Cyclic MCC model. Test: $\sigma_{1mean}2-F3-A1$.

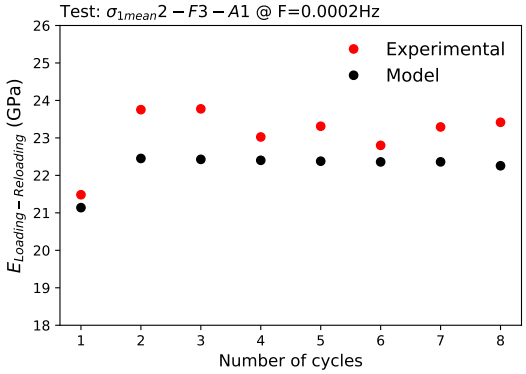


Figure 5.7: Comparison of experimental and model Young modulus for loading and reloading intervals versus the number of cycles. These Young's modulus are apparent numbers affected by inelastic strains and visco-elasticity.

**Effect of frequency**

It is of particular interest for up-scaling purposes (from lab to storage field conditions), to understand what properties could change with frequency. Table 5.1 presents the magnitudes of the final parameters used to fit the experimental data for tests carried out in the 'elastic regime'. For these simulations, 'M' was defined as 2.35, based on Pijnenburg et al., 2019 estimation for Slochteren sandstones. This table as well as figure 5.8 show that visco-elastic viscosity $\eta_1$ is apparently a strong function of frequency, which increases as frequency decreases. It is interpreted that this viscosity could be also a function of strain rate as creep viscosity is (B. van der Pluijm, 2004 and R. Weijermars, 1997). Thus, as frequency decreases, the mean strain rate decreases and viscosity increases, suggesting a strain rate thinning-like behavior. In terms of the constitutive model, it is like the Nishihara's model were comprised by a non-newtonian Kelving-Voigt dash-pot. Even though, it was not found referential information about this behavior, visco-elastic viscosity estimated for Bergermeer's sandstone reservoir during the modeling of gas storage (Fenix-Consulting-Delft-BV, 2018) support the estimated experimental trend of viscosity against frequency as shown in figure 5.8.

Given that the test in the elastic regime showed an apparently time-dependent inelastic behavior (figure 4.11) but the model does not account for this, the plastic multiplier ($\lambda_{MCC}$) was slightly increased as the frequency of the experiments decreases (as shown in table 5.1) to reproduce the inelastic strain

| Test | F [Hz] | $\lambda_{MCC}$ $[GPa^{-1}]$ | $\theta$ | $\eta_1$ [GPa.s] | E1 [GPa] | E2 [GPa] | Eavg. [GPa] | $p_c^{initial}$ [MPa] | $\epsilon^{inelastic}$ Model/Lab [%] |
|---|---|---|---|---|---|---|---|---|---|
| $\sigma_{1mean}2-F1-A1$ | 0.014 | 1.50E-04 | 0.004 | 250 | 45 | 48 | 23.3 | 10 | 0.0314 / 0.0319 |
| $\sigma_{1mean}2-F2-A1$ | 0.0014 | 1.85E-04 | 0.006 | 1900 | 46 | 49 | 23.7 | 10 | 0.031 / 0.031 |
| $\sigma_{1mean}2-F3-A1$ | 0.0002 | 2.30E-04 | 0.0045 | 13000 | 43 | 48 | 22.7 | 10 | 0.042 / 0.045 |

Table 5.1: Model input parameters and difference in total inelastic strain between the model and lab measurements for tests in the 'elastic regime' and amplitude of 20 MPa

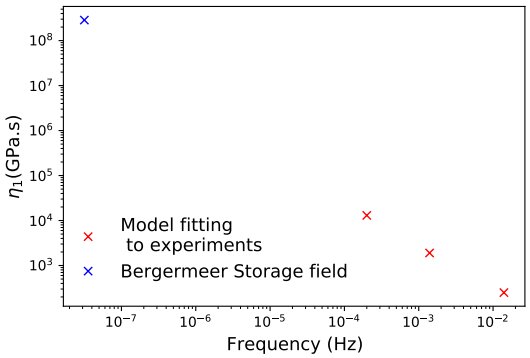


Figure 5.8: Behavior of visco-elastic viscosity versus frequency from fitting the model to experimental data and Bergermeer gas storage project (Fenix-Consulting-Delft-BV, 2018). Experimental conditions:$\sigma_{mean}$=38MPa A= 20MPa.

.

of the first cycle. Longer experiments may be required to determine if time-dependent behavior is of importance in the elastic regime.

## 5.2.2. Modeling brittle regime cyclic tests

For modeling the deviatoric cyclic experiments performed in the brittle regime, the first step was the definition of the parameters for the hardening-softening model and brittle creep model. These parameters remained constant in all simulated deviatoric cyclic and creep tests, i.e., they are considered independent of frequency and sample characteristics.

**Hardening-softening model**

For the calibration of the hardening-softening model, first the range for cohesion and friction angle were established. This was done through the use of monotonic test results for Red Felser sandstone at different confining pressures as shown in figure 5.9. It can be seen that cohesion could range between 12MPa and 32MPa while the friction angle could be between $25^o$ and $48^o$ for $\sigma_3 = 10MPa$.

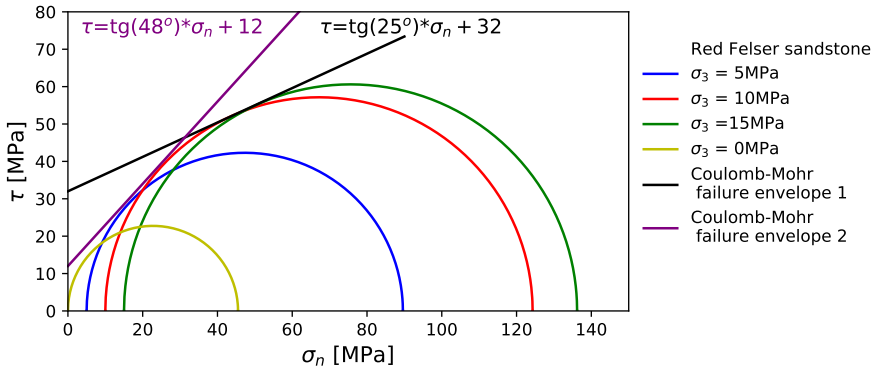


Figure 5.9: Possible Coulomb-Mohr failure envelopes and Mohr circles at different confining stress ($\sigma_3$) for Red Felser sandstones. Definition of limits for cohesion and friction angle for the hardening-softening model.

Next, the hardening-softening model was finally calibrated against the first loading of the test ($\sigma_{1mean} - F3 - A1$) and the expected peak strength of the rock (124 MPa at $\sigma_3 = 10MPa$ as shown in figure 4.3). The manual fitting of the experimental and simulated curves as well as the final values of the hardening model are shown in figure 5.10. These parameters will remain constant during modeling of cyclic tests.

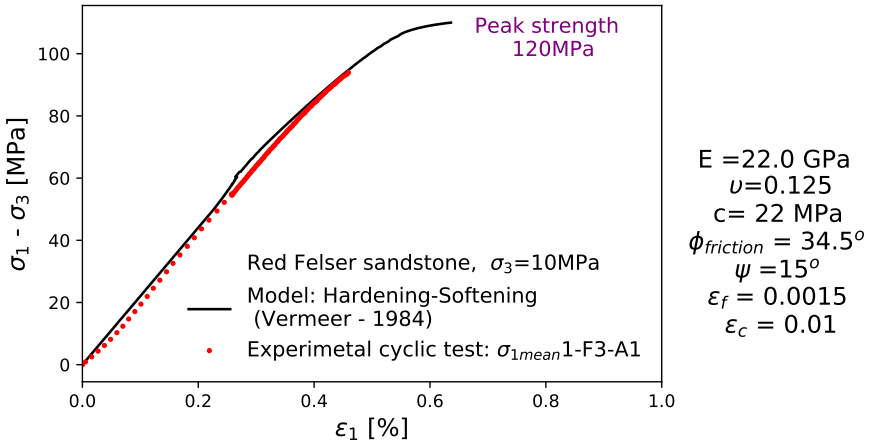


Figure 5.10: Calibration of hardening-softening model against first loading of test $\sigma_{1mean} - F3 - A1$ and peak strength referential data.

**Brittle creep model**

The second step was the calibration of the creep model as well as the whole proposed model (equation 5.1.1) against the multistage creep test. Thus, initial calibration of the viscoelastic and MCC model parameters also took place. Figure 5.11-left shows that it was possible to reproduce the strain of the first and second stress steps as well as the instantaneous strain jumps of every step. The latter was thanks to the hardening-softening model as shown in figure 5.11-right. The last stress step ($\sigma_1$=115.5MPa) was not reproduced completely. A higher strain rate than the simulated by the linear creep model is needed. This could be obtained by considering a non-linear creep model. Table **??** shows the fitted parameter. Referential 'M' was taken from Pijnenburg et al., 2019 and adjusted, such as the stress path at the brittle yield point (expressed in p and q) was right below the critical state line.

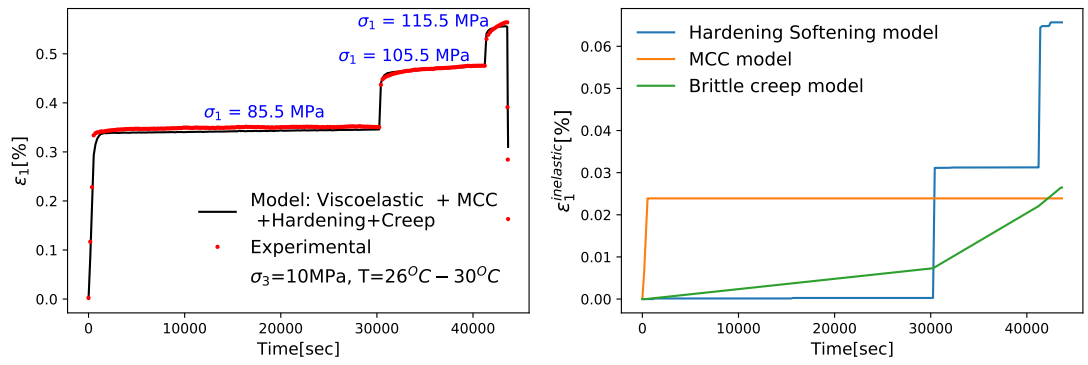


Figure 5.11: Fitting the proposed model against multistage creep test 2 (left). Estimated contribution of the different inelastic models along time after matching multistage creep test 2.

**Cyclic model**

Finally, the deviatoric cyclic tests performed in the brittle regime were reproduced with the proposed model (equation 5.1.1). It is important to mention that cyclic plasticity is modeled with the MCC model, following equation 5.14, which means that all cyclic plastic strains are modeled as inelastic compaction. During modeling, the parameters in table 5.2 were held constant for consistency. It was only adjusted the visco-elastic viscosity ($\eta_1$), Young's modulus and the cyclic parameter Theta '$\theta$' to match the strain

| | | |
|---|---|---|
| Viscoelastic | $E_1$ [GPa] | 46 |
| | $E_2$ [GPa] | 49 |
| | $\eta_1$ [Gpa.s] | 13000 |
| | $\upsilon$ | 0.125 |
| MCC | M | 2.35 |
| | $\lambda_{MCC}$ | 1.20E-04 |
| | $p_c^{initial}$ [MPa] | 10.1 |
| | $phi$ [frac.] | 0.2056 |

| | | |
|---|---|---|
| Hardening & softening | $E_{avg.}$ [GPa] | 23.726 |
| | $c$ [MPa] | 22 |
| | $\phi_{friction}$ [degree] | 34.5 |
| | $\psi$ | 15 |
| | $\epsilon_f$ | 0.0015 |
| | $\epsilon_c$ | 0.01 |
| Brittle creep | $\eta_2$ [GPa.s] | 1823253 |
| | $\sigma_{yield}^{Brittle}$ [GPa.s] | 81 |

Table 5.2: Model parameters used to reproduce experimental multistage creep test 2. 'M' was defined based on referential values for sandstones provided by Pijnenburg et al., 2019 and making sure the stress path does not reach the CSL. These parameters will remain constant during modeling brittle cyclic tests, except for viscosity of the visco-elastic unit and the corresponding Young's modulus and brittle yield point of every sample

profile.

Figure 5.12 shows the model result against brittle deviatoric cyclic tests after performing data fitting. It can be clearly seen that brittle creep plays an important role as the frequency decreases because there was more time for this type of deformation to become significant. In addition, cyclic plasticity was required to reproduce the experimental results of all the tests at the amplitude of 20 MPa (A1). Cyclic plasticity became more important for high-frequency tests, where creep contribution is negligible (Figure 5.12 - Top).

| Test | Frequency [Hz] | $\theta$ | $\eta_1$ [Gpa.s] | Eavg. [GPa] | $\epsilon^{inelastic}$[%] Lab / Model |
|---|---|---|---|---|---|
| $\sigma_{1mean}1-F1-A1$ | 0.014 | 0.003 | 650 | 23.25 | 0.05 / 0.07 |
| $\sigma_{1mean}1-F2-A1$ | 0.004 | 0.005 | 7800 | 21.8 | 0.058 / 0.065 |
| $\sigma_{1mean}1-F3-A1$ | 0.0002 | 0.005 | 40000 | 21.8 | 0.0604 / 0.079 |

Table 5.3: Model parameters: $\theta$ and visco-elastic viscosity $\eta_1$ against frequency for tests in the brittle regime. It is also mentioned the difference in total inelastic strain between the model and lab measurements. $F1 > F2 > F3$

As well as for the tests in the elastic regime, it was also required to increase visco-elastic viscosity as the frequency decreases while Theta cyclic parameter was in general similar. Only for the high frequency test, it was required a slightly lower Theta, which means that more contribution was required from the cyclic inelastic model. The description of the adjusted parameters is shown in table 5.3.

### 5.2.3. Effect of amplitude on cyclic model's parameters

The experimental tests with the lowest amplitude (5.11 MPa) and frequency (0.0002 Hz) for both regimes were also modeled. This amplitude is relevant for underground energy storage. The fitting of the model to experimental data for these tests are shown in appendix D. Figures 5.13 and 5.14 show a comparison of cyclic plasticity and creep contributions between high and low amplitude tests (A1 and A2 respectively). Regarding the tests in the elastic regime, the cyclic model suggests that cyclic plastic strains are proportional to the amplitude (figure 5.13).

In addition to the proportionality between cyclic plastic strains and amplitude (figure 5.14-left), there is an attenuation of the cyclic plasticity mechanism when amplitude is reduced for tests in the brittle regime. This is suggested by the need to increase the cyclic parameter ($\theta$) from a value of 0.005 at an amplitude of 20 MPa to a value of 0.1 at an amplitude of 5.11 MPa to match the model ($\theta$=1 means no cyclic plasticity). Thus, creep deformation, which is also proportional to amplitude (figure 5.14-right), becomes the main inelastic mechanism at low amplitudes. It is important to mention that during the matching of the low-amplitude test in the brittle regime, it was required a higher plastic multiplier parameter ($\lambda_{MCC}$=2.0e-4) than for the other samples. This can be noticed in the initial inelastic strain behavior shown in figure 5.14-left).

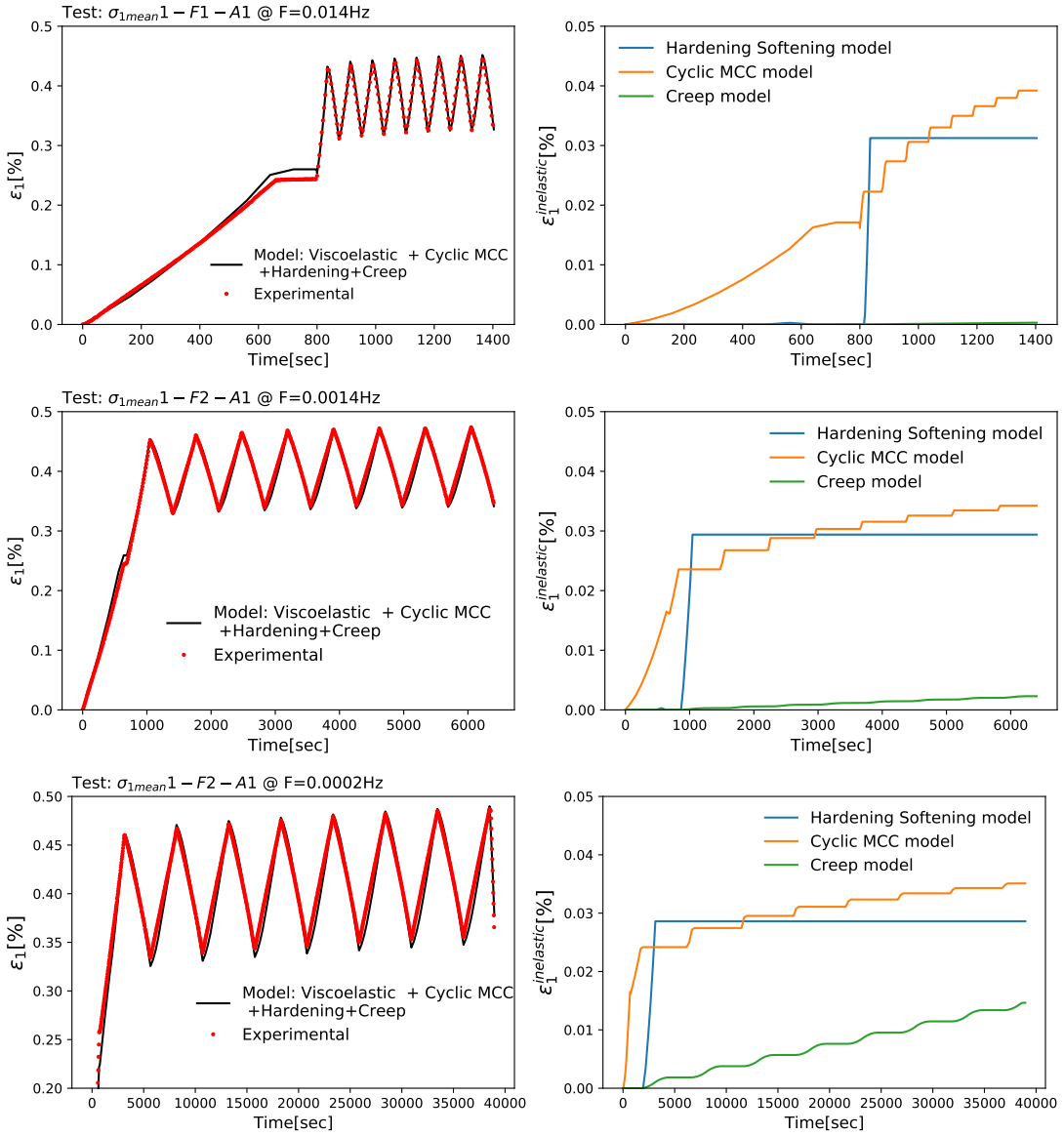


Figure 5.12: Fitting the proposed model against deviatoric cyclic tests (left). Inelastic strain contribution by the plastic and brittle creep mechanisms (right). $\sigma_{1mean}1-F1-A1$ (top), $\sigma_{1mean}1-F2-A1$ (center) and $\sigma_{1mean}1-F3-A1$ (bottom).

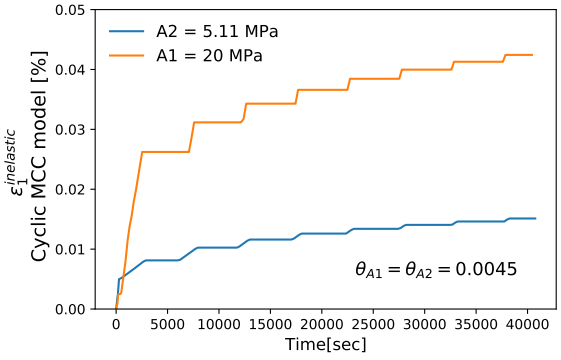


Figure 5.13: Comparison of cyclic plastic inelastic strains for two amplitudes: 5.11 MPa and 20 MPa. Every strain step is one cycle. Tests condition: F3=0.0002Hz, elastic regime ($\sigma_{1mean} = 38MPa$).

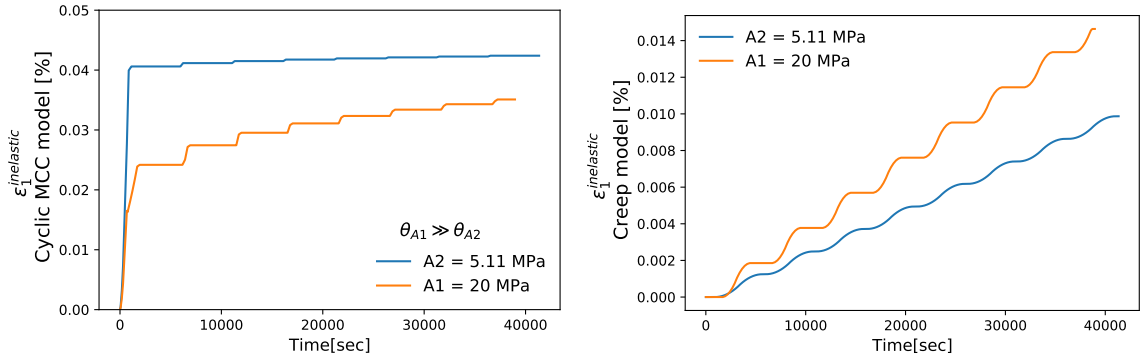


Figure 5.14: Comparison of cyclic plastic inelastic strains (left) and creep strain (right) for two amplitudes: 5.11 MPa and 20 MPa. Every strain step is one cycle. Tests condition: F3=0.0002Hz, brittle regime ($\sigma_{1mean} = 85MPa$)

# 6

# Possible implications on underground energy storage

In this chapter, it is discussed the possible implications of cyclic loading on underground energy storage field applications. This is based on the results obtained after performing the experimental tests, corresponding analytical modeling and referential works. For quantification of these implications, it is required to perform field simulations and additional experimental tests.

**Subsidence and uplifting** The vertical displacement of the surface, subsidence and uplifting, due to changes in reservoir pore pressure can be one of the most obvious consequences of underground energy storage. This depends on rock mechanical properties and stress paths but also on the inelastic strains, which together define the compaction of the reservoir. Based on the inelastic strains measured cycle after cycle during experiments, it can be forecasted that irreversible subsidence could take place during this type of storage. Its magnitude depends on the amplitude of the pore pressure and corresponding deviatoric stress. On top of that, the most severe subsidence could happen during the first depletion of the reservoir or first cycle of storage, where the inelastic contribution is the most. This has been already registered in field applications like the one in the NORG and Bergemeer fields (N.A.M., 2016 and Fenix-Consulting-Delft-BV, 2018 respectively). In the case of storage in a depleted gas reservoir, it is expected that the magnitude of subsidence during storage to be lower than during the depletion because the rock is expected to behave more elastic if deviatoric stress is not increased.

In addition, the possible visco-elastic behavior of the rock and/or brittle creep could lead to the pore pressure - subsidence behavior being out of phase. This means that subsidence could continue for a while even though fluid production has stopped. This has been also pointed out by other researchers (Pijnenburg et al., 2018).

**Cap rock flexure** The inelastic compaction of the reservoir generated cycle after cycle can promote the increase of tensional stresses in the corresponding caprock, a phenomenon called caprock flexure (Heinemann et al., 2021). Depending on the magnitude of the inelastic strains and caprock's mechanical properties, this could lead to fracturing (mode I fractures) and leakage of the stored fluid.

**Fault reactivation and seismicity**
The movement of faults is the result of induced changes in the stress conditions on the fault plane, such as the corresponding stress path hits the fault reactivation envelope. During storage operations, a severe increase or decrease in pore pressure can lead to fault reactivation. Thus, a pore pressure threshold, upon which fault reactivation is triggered, can be defined. This pore pressure dictates the maximum storage capacity, in the cases where seismic events want to be avoided.

The generation of inelastic stress can cause changes in the stress path during storage operations as can be deduced from equation 6.1, where $D$ and $D^{inelastic}$ are the elastic and inelastic matrices.

This was also experimentally shown by Dietl et al., 2019 and is shown in figure 2.10. This means that the pore pressure threshold for fault reactivation could change cycle after cycle. This could be positive or negative, depending on the direction of this change.

$$\dot{\sigma} = \left(D - D^{inelastic}\right)\dot{\epsilon} \tag{6.1}$$

In addition, the decreasing incremental rate shown by inelastic strains, leads to think that the rock will behave more elastic as the number of cycles increases for stress conditions below the brittle yield point. In term of energy, this means that the rock would store more elastic energy as the number of cycles is higher. Thus, if there is an interest in changing the pore pressure to increase storage capacity, it could be better to do it in early cycles to minimize the magnitude of the released energy, in the case the fault reactivation envelop is reached by the stress path.

**Storage capacity and flow** The porosity reduction anticipated by the cyclic MCC plastic model (shown in figure during inelastic compaction 5.4), means that the storage capacity could reduce cycle after cycle, being the major reduction in the first cycle. The magnitude would depend on the amount of inelastic strain experienced by the rock. In addition, as the permeability is a function of porosity, it is expected also a reduction of permeability during inelastic compaction. Nevertheless, if the cyclic loading is taking place above the brittle yield point, increases in porosity and permeability could be expected.

**Sand production** In sandstone reservoirs used for energy storage, largest stresses are found around the wells due to a phenomenon called stress concentration. Which means that this area is more prone to experience cyclic brittle deformation if stresses exceed the brittle yield point. Which could lead to cohesion reduction (Vermeer and de Borst, 1984) and sand grain size decrease, setting favorable conditions to sand grains movement if fluid velocity is sufficiently high.

# 7

# Conclusions and recommendations

A database was created regarding cyclic loading publications relevant to underground energy storage. It was seen that the most studied rock is the sandstone. It was also determined that there is a lack of cyclic loading experimental studies under low frequency condition, which are pertinent for understanding underground energy storage.

Red Felser sandstone under constant amplitude cyclic loading conditions exhibited elastic and inelastic deformations cycle after cycle. These inelastic deformations took place at stress conditions above and below the brittle yield point (onset of dilatant cracking). The inelastic strain per cycle showed a decreasing trend as the number of cycles increases. Therefore, fatigue was not registered within the number of cycles tested.

The cyclic inelastic deformations were affected by the mean stress, amplitude and frequency of the stress waveform imposed during testing. On one hand, the higher the mean stress or the higher the amplitude, then the higher the total inelastic strains. On the other hand, the lower the frequency the higher the total inelastic strain.

There are time-dependent deformations for stress conditions below and above the brittle yield point. Nevertheless, those deformations below the brittle yield point were only significant in the first cycle.

The interpreted deformations for Red Felser sandstone were: Elastic, plastic, cyclic-plastic, viscoelastic and brittle creep. The two latter mechanisms represent time-dependent elastic and inelastic deformations respectively while the three formers are instantaneous deformations.

The recorded acoustic emissions indicated that inelastic strains were generated almost right after the hydrostatic condition was exceeded. This means that the samples do not behave purely elastic in any section of the first loading strain-stress curve. As a consequence, the Young's modulus estimated in the first loading is an apparent number affected by inelastic strains. Contrary, subsequent cycles showed acoustic emissions at stress close to the maximum applied stress (felicity effect) and lower inelastic strains. This suggests that the yield point could have moved closer to the maximum applied stress condition, making the rock behave more elastic.

A deformation model, that combines Nishihara's constitutive model plus plastic and cyclic-plastic models, was proposed. Elastic, viscoelastic and steady creep were modeled by the Nishihara's constitutive model, while inelastic compaction was computed with Modified Cam-clay model (Roscoe and Burland, 1968) and dilatant inelastic deformations were modeled with a Hardening-Softening model (Vermeer and de Borst, 1984). To model the cyclic inelastic compaction, an extension of the Modified Cam-clay model was proposed. This proposal was inspired by the work of Carter et al., 1979 and considers a yield surface that spreads with the number of cycles. It has as upper limit, the maximum applied loading surface. This model is able to capture the decrease of inelastic strains cycle after cycle recorded during experimental tests. The model depends on a material parameter defined as $\theta$ that can

be obtained from deviatoric cyclic tests. A model for cyclic inelastic strains induced by dilatant behavior was not considered due to complexity.

Axial strains from cyclic loading tests were reproduced with the proposed model. Analytical modeling results suggested that visco-elastic viscosity is a function of frequency: the lower the frequency, the higher the viscosity. Thus, it could be a parameter to take into account during upscaling from lab to field conditions.

Modeling indicated that the contribution of brittle creep in Red Felser sandstone becomes important for frequencies equal to or higher than 0.0002Hz while it is negligible for high frequencies (>0.0014 Hz). In addition, a sandstone may develop cyclic-inelastic strains only if the stress reaches the previously established yield surface. Otherwise, the rock would behave fully elastic. Finally, the magnitude of the cyclic inelastic strains is a function of amplitude and the mean stress.

Based on the experimental and theoretical results, as well as the literature, it was identified that cyclic inelastic deformation could have implications on several processes, such as subsidence, fault reactivation and seismicity, caprock flexure, reduction of pore volume and flow capacity and possible sand production. Fatigue of the reservoir rock could be also experienced if the stress state is beyond the brittle yield surface. Consequently, it is not expected fatigue for cyclic stress states within the brittle yield surface because dilatant cracking, that could lead to localization and failure, is not induced.

Running long-term cyclic tests requires temperature steady conditions, such as the LVDT measurement are not affected by the machine's accessories expansion a contraction cause by thermal effects. Thus, it is recommended to carry out these tests in a thermal regulated equipment, where the cell is inside an oven. Nevertheless, if only triaxial standard equipment is available, it is recommended to heat up the equipment and cell for sufficient time before performing long-term cyclic or brittle creep tests.

It is recommended to explore other constitutive models or improved the one proposed here to determine if it is possible to model only with one plastic model the early compaction and dilation and the corresponding cyclic instantaneous inelastic strains.

# List of Symbols and Abbreviations

| | |
|---|---|
| $A$ | amplitude |
| $D$ | elastic matrix |
| $E$ | Young's modulus |
| $E_1$ | Young's modulus of Nishahara's elastic unit |
| $E_2$ | Young's modulus of Nishahara's visco-elastic unit |
| $F$ | frequency |
| $M$ | slope of critical state line |
| $q$ | deviatoric effective stress |
| $p$ | pressure effective stress |
| $p_c$ | pre-consolidation parameter |
| $p_l$ | loading parameter |
| $S_1$ | maximum principal total stress |
| $S_3$ | minimum principal total stress |
| $t$ | time |
| $\alpha$ | Biot coefficient |
| $\epsilon_1$ | axial strain in triaxial convention |
| $\epsilon$ | strain vector voigt notation |
| $dot\epsilon$ | strain rate vector voigt notation |
| $\sigma_1$ | maximum principal effective stress |
| $\sigma_{1mean}$ | mean stress of the loading waveform |
| $\sigma_3$ | minimum principal effective stress |
| $\sigma_{yield}^{Brittle}$ | brittle yield point |
| $\delta_{ij}$ | Kronecker delta |
| $\upsilon$ | poisson's ratio |
| $\eta_1$ | visco-elastic viscosity |
| $\eta_2$ | brittle creep viscosity |
| $AE$ | acoustic emissions |
| $ATES$ | aquifer thermal energy storage |
| $CSL$ | critical state line |
| $LVDT$ | linear variable differential transformer |
| $MCC$ | modified Cam-Clay model for plastic strains |
| $UES$ | underground energy storage |

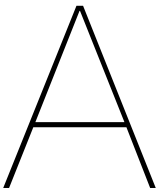

# Appendix

| Authors | year | Title | Learning outcome | Rock | Type of cyclic test | Main objetive |
|---|---|---|---|---|---|---|
| Arora K. et al. | 2019 | Experimental Study on Stiffness Degradation of Rock Under Uniaxial Cyclic Sinusoidal Compression Loading | Fatigue of sandstone is a function of peak stress. Tangent E modulus didn't change over cycle but inelastic strain accumulates which make the Secant modulus decrease with the cycles. | sandstone | Deviatoric cyclic test | Elastic properties variation |
| Bagde M. et al. | 2005 | Fatigue properties of intact sandstone samples subjected to dynamic uniaxial cyclical loading | Frequency and strain amplitudes affects rock behavior. Tangent E increases over cycles. Secant and tangent E calculations are explained. | sandstone | Deviatoric cyclic test | Fatigue |
| Burdine N. | 1963 | Rock failure under dynamic loading conditions | The number of cycles to reach Fatigue increases as the confining pressure is increased in triaxial cyclic tests | sandstone | Deviatoric cyclic test | Fatigue |
| Chen et al. | 2020a | Prediction of Fracture Damage of Sandstone Using Digital Image Correlation | Digital image correlation (DIC) method can be used to follow fracture propagation | sandstone | Deviatoric cyclic test | Damage |
| Chen Y. et al. | 2020b | Experimental investigation on the crack propagation behaviors of sandstone under different loading and unloading condition | Crack propagates faster as the confining pressure is reduced faster | sandstone | Deviatoric cyclic test | Crack propagation |
| Gatelier et | 2002 | Mechanical damage of an anisotropic porous rock in cyclic triaxial tests | Compaction and micro-cracking, which form Damage, are the main inelastic mechanism, with higher variations in the first cycles. "Damage can be quantified by changes in mechanical properties" | sandstone | Deviatoric cyclic test | Damage |
| Heap M. et al. | 2009 | Elastic moduli evolution and accompanying stress changes with increasing crack damage: Implications for stress changes around fault zones and volcanoes during deformation | Micro-craking damage can be present near the faults, which can affect stress path as the elastic properties change. Demonstrated with cyclic damage tests. | sandstone and volcanic rock | Deviatoric cyclic test | Elastic properties variation |
| Heap M. et al. | 2007 | Quantifying the evolution of static elastic properties as crystalline rock approaches failure | Tangent elastic modulus in damage cyclic test decreases as the number of cycles and amplitudes increases | sandstone and volcanic rock | Deviatoric cyclic test | Elastic properties variation |
| Jia et al. | 2018 | Characterization of the deformation behavior of fine-grained sandstone by triaxial cyclic loading | The evolution mode of E and v depends on the deviatoric stress magnitude. It is explain a method to estimate tangent E and v that discount inelastic strain. | sandstone | Deviatoric cyclic test | Elastic properties variation |
| Kou et al. | 2019 | Experimental study of the prepeak cyclic shear mechanical behaviors of artificial rock joints with multiscale asperities | Joint can undergone shear cyclic loading which causes degradation of joint asperities. | Cracked sandstone | Shear cyclic test | shear mechanical behaviors of artificial rock joints |
| Le J. et al. | 2014 | Scaling of fatigue crack growth in rock | The propagation of existing fracture is also affected by cyclic loading and is a function of the sample size | sandstone | Deviatoric cyclic test | Fatigue |
| Li G. et al. | 1992 | Fatigue crack growth in brittle sandstones | Variation of the crack-tip stress intensity factor affect crack propagation | sandstone | Tension cyclic test | Crack propagation |
| Li N. et al. | 2003 | Fatigue properties of cracked, saturated and frozen sandstone samples under cyclic loading | The cracked samples have more obvious fatigue effects than the non-cracked samples | Cracked sandstone | Deviatoric cyclic test | Fatigue |
| Liu E. et al. | 2011 | Dynamic Properties of Intact Rock Samples Subjected to Cyclic Loading under Confining Pressure Conditions | as the confining pressure is higher the change of tangent E is lower. | sandstone | Deviatoric cyclic test | Fatigue |
| Liu Y. et al. | 2017 | Experimental Investigation of the Influence of Joint Geometric Configurations on the Mechanical Properties of Intermittent Jointed Rock Models Under Cyclic Uniaxial Compression | Using artifitial cracks, it was found that crack geometry affects the fatigue of initially cracked rocks | Cracked sandstone | Deviatoric cyclic test | Fatigue |
| Liu X. et al. | 2018 | An experimental investigation on the shear mechanism of fatigue damage in rock joints under pre-peak cyclic loading condition | Shear strength of jointed rocks is affected by the generation of damage in the joint asperities | Cracked sandstone | Shear cyclic test | Fatigue |
| Meng Q. et al. | 2016 | Effects of Acoustic Emission and Energy Evolution of Rock Specimens Under the Uniaxial Cyclic Loading and Unloading Compression | Acoustic emissions can help to understand the balance between stored and released energy during cyclic loading. | sandstone | Deviatoric cyclic test | Damage - Acoustic Emissions |
| Nejati H. et al. | 2014 | Brittleness Effect on Rock Fatigue Damage Evolution | The brittleness (Lithology) of the rock affects micro-cracking density, thus damage evolution. The more ductile the rock the larger the number of cycles needed to reach fatigue. | sandstone, Marble, Limestone | Deviatoric cyclic test | Damage - Acoustic Emissions |
| Peng et al. | 2019 | Effects of stress lower limit during cyclic loading and unloading on deformation characteristics of sandstones | Large amplitudes do not necessarily induces larger changes in elastic properties and damage. If mean stress are higher more damage could be induced. | sandstone | Deviatoric cyclic test | Elastic properties variation |

Table A.1: Publication database on Cyclic loading experiments in rocks and cement samples. Part I

| Authors | year | Title | Learning outcome | Rock | Type of cyclic test | Main objetive |
|---|---|---|---|---|---|---|
| Prost G. | 1988 | Jointing at rock contacts in cyclic loading | Lateral cyclic loading can induce mode I fractures if the axial load is lower than 59 perc. of the rock strength | Cracked sandstone | Deviatoric cyclic test | Crack propagation |
| Ray S. et al | 1999 | Effect of cyclic loading and strain rate on the mechanical behaviour of sandstone | There is a fatigue stress level below which the rock will not fail. UCS decreases in rocks subjected to cyclic loading that did'nt experience fatigue. The Higher the amplitude the higher the UCS's drop. | sandstone | Deviatoric cyclic test | Fatigue |
| Song et al. | 2016 | Experimental analysis and characterization of damage evolution in rock under cyclic loading | Similar to Ray S. et al 1999. UCS decreases in rocks subjected to cyclic loading that did'nt experience fatigue. The Higher the amplitude the higher the UCS's drop. Deformation can be captured with Digital image correlation. | sandstone | Deviatoric cyclic test | Damage |
| Taheri et al. | 2016 | Study on variations of peak strength of a sandstone during cyclic loading | Method to predict compressive strength without failing the rock. Useful to define the real maximum stress-compressive strength ratio. But there is still concern about its effect on deformation during subsequent cyclic loading | sandstone | Deviatoric cyclic test | Fatigue |
| Zhenyu T. | 1990 | An experimental study and analysis of the behaviour of rock under cyclic loading | Waveform shape impact deformation (Sinusoidal larger than triangle). Static , Creep and damage deformation are present in cyclic loading. Viscoplasticity was introduced to model cyclic loading. | sandstone | Deviatoric cyclic test | Fatigue |
| Tien Y. et al. | 1990 | Strain, pore pressure and fatigue characteristics of sandstone under various load conditions | Strain in the first cycle give information of the number of cycles to reach fatigue. Frequency the higher the higher the number of cycles for low confining pressures. Undrained pore pressure indicate volumetric deformation stage. | sandstone | Deviatoric cyclic test | Fatigue |
| Xu J. et al. | 2009 | Acoustic emission characteristic during rock fatigue damage and failure | Damage expression can be derived from acoustic emissions | sandstone | Deviatoric cyclic test | Damage - Acoustic Emissions |
| Zhang H. et al. | 2013 | Experimental Analysis on Deformation Evolution and Crack Propagation of Rock Under Cyclic Indentation | Crack initiates when the indentation load achieves a critical value. Closure and opening of cracks is seen during unloading and loading | sandstone | Flexural cyclic test | Crack propagation |
| Bastian T. et al. | 2014 | Progressive damage of hawkesbury sandstone subjected to systematic cyclic loading | The higher the peak stress,mean stress and amplitude the higher the damage. From damage evolution, tangent Young modulus is expected to decrease. | sandstone | Deviatoric cyclic test | Damage |
| Karakus M. et al. | 2016 | Rock fatigue damage assessment by acoustic emission | Acoustic emission can be used to follow damage evolution and generate models for damage. Poisson ration increases. | sandstone | Deviatoric cyclic test | Damage - Acoustic Emissions |
| Li N. et al. | 2003 | Fatigue properties of cracked, saturated and frozen sandstone samples under cyclic loading | Rocks with cracks are more prone to reach fatigue than intact rocks | Cracked sandstone | Deviatoric cyclic test | Fatigue |
| Munoz H. et al. | 2017 | Local Damage and Progressive Localisation in Porous Sandstone During Cyclic Loading | Cyclic loading in post-peak regime (no other test in this regime) allows analysis crack localization. Damage equation based on Young is presented | sandstone | Deviatoric cyclic test | Damage |
| Singh S. et al. | 1989 | Fatigue and strain hardening behaviour of graywacke from the flagstaff formation | "If the maximun applied stress level in cyclic loading does not cause rock failure up to an infinite number of cycles, the rock gets "strain hardened", i.e. its uniaxial".Mean and peak stress affects fatigue. compressive strength increases. | sandstone | Deviatoric cyclic test | Fatigue |
| Wang H. et al. | 2017 | Gas Permeability and Porosity Evolution of a Porous Sandstone Under Repeated Loading and Unloading Conditions | Porosity and permeability reduced with the cycles. Nevertheless there is not report on what happens upon Fatigue | sandstone | Lateral constraint pore pressure cyclic test | Porosity-Permeability |
| Yamashita S. et al. | 1999 | The relationship between the failure process of the creep or fatigue test and of the conventional compression test on rock | Effect of damage induced with cycling loading on post peak behavior | sandstone | Deviatoric cyclic test | Fatigue |
| Yang S. et al. | 2015 | Experimental investigation on mechanical damage characteristics of sandstone under triaxial cyclic loading | Opposed to most of the tests, the sandstones shows strain hardening during damage test (increasing amplitude) at low confining stress. | sandstone | Deviatoric cyclic test | Fatigue |
| de Kloe K.P. et al. | 2008 | Cyclic Compaction Experiments on Samples from Norg-5. | Lateral Constraint test (fixed Axial stress) with cyclic pressure are possible to performed. To keep the radial strain zero the lateral stress is adjusted. Variation of the lateral stresses with cycles is an indication o Poisson's ratio | sandstone | Lateral constraint pore pressure cyclic test | Elastic properties variation |
| Present work | | | | | | |
| Dietl C. et al. | 2019 | Poroelasticity of a Porous Underground Gas Storage System: Is there Material Fatigue? | Lateral Constraint test (fixed Axial stress) with cyclic pressure are possible to performed. Volumetric strains are experienced. Sligth decrease of the compaction coefficient was recorded. Poisson's ratio was not estimated. | sandstone | Lateral constraint pore pressure cyclic test | Elastic properties variation |
| Present work | | | | | | |

Table A.2: Publication database on Cyclic loading experiments in rocks and cement samples. Part II

| Authors | year | Title | Learning outcome | Rock | Type of cyclic test | Main objetive |
|---|---|---|---|---|---|---|
| Ghamgosar M. et al. | 2016 | Experimental Investigation of Fracture Process Zone in Rocks Damaged Under Cyclic Loadings | The density of fractures increases with the cyclic tensile loading | sandstone | Tension cyclic test | Crack propagation |
| Hu C. et al. | 2017 | Poro-mechanical properties evolution under hydrostatic stress after induced damage | Biot coefficient could also change during cyclic loading but still more prominent the Poisson's ratio variation | sandstone | Deviatoric cyclic test | Elastic properties variation |
| Jiqiang L. et al. | 2021 | Stress sensitivity of formation during multi-cycle gas injection and production in an underground gas storage rebuilt from gas reservoirs | Cyclic loading can affect storage capacity by reducing permeability and porosity | sandstone | Lateral constraint pore pressure cyclic test | Porosity-Permeability |
| Pijnenburg R. et al. | 2019 | Inelastic Deformation of the Slochteren Sandstone:Stress□Strain Relations and Implications for Induced Seismicity in the Groningen Gas Field | Cyclic damage tests (increasing amplitude every cycle) are used to describe the inelastic deformation undergone by the rock during monotonic triaxial test, they claim, no additional damage is induced with this cycles. This method includes hydrostatic cyclic tests. | sandstone | Hydrostatic cyclic test | Damage |
| Zhao Y. et al. | 2021 | Effect of Unloading Rate on the Mechanical Behavior and Fracture Characteristics of Sandstones Under Complex Triaxial Stress Conditions | Cyclic confining pressure while keeping constant vertical stress can be also studied. A method is provided to calculate secant and tangent E and Poisson's ratio.The highest the amplitude the highest the change of elastic properties. | sandstone | Deviatoric cyclic test | Elastic properties variation |
| Wichtmann T. | 2005 | Explicit accumulation model for non-cohesive soils under cyclic loading | Cyclic test can be performed with variation of all principal stresses. This changes can be induced simultaneously in or off synchronization. This thesis have a extended description of the cyclic loading field, specially for soil or unconsolidated rocks | sandstone | Simultaneous S1 and S2 cyclic test | Inelastic accumulation |
| Fuenkajorn K. et al. | 2010 | Effects of cyclic loading on mechanical properties of Maha Sarakham salt | Introduced the problem of field frequency. A higher loading frequency results in a lower visco-plasticity of the salt. There is an equation (10) that relates viscoplastic coefficient with frequency that it is used for Upscaling. Strain curves show transient, steady-state and tertiary phases as in creep. Static (creep) tests can under-estimate the cavern deformation. | Rock salt | Deviatoric cyclic test | ViscoElasticPlastic properties variation |
| Guo Y. et al. | 2012 | Mechanical properties of Jintan mine rock salt under complex stress paths | The necessity of cyclic accumulated deformation for fatigue damage would be reduced as mean and peak stress are increased, which translates to fatigue life decrease. | Rock salt | Deviatoric cyclic test | Fatigue |
| Ma L. et al. | 2013 | Experimental investigation of the mechanical properties of rock salt under triaxial cyclic loading | The axial strain rate and decrease nonlinearly with increasing loading frequency. There is method for calculating E and v modulus. Higher frequency appears to result in a lower viscoplasticity of the salt | Rock salt | Deviatoric cyclic test | ViscoElasticPlastic properties variation |
| Song R. et al. | 2013 | Experimental investigation of the fatigue properties of salt rock | Storage caverns are influenced by gas injection and production, and the surrounding salt rock may experience fatigue damage.Fatigue life increases with higher confining pressures. | Rock salt | Deviatoric cyclic test | Fatigue |
| Trippetta F. et al. | 2013 | Evolution of the elastic moduli of seismogenic Triassic Evaporites subjected to cyclic stressing | Method for elastic properties: Stress–strain curves were first fitted with a third-order polynomial according to the method proposed by Heap and Faulkner (2008), and then differentiated so that tangent moduli could be calculated for any given value of stress. Elastic properties calculated by this method were higher than dynamic method (seismic waves) | Evaporites | Deviatoric cyclic test | Elastic properties variation |
| Liu J. et al. | 2014 | Damage evolution of rock salt under cyclic loading in unixial tests | Damage evolution equation coupled with plastic deformation can be used to describe the damage evolution characteristics of rock salt cavern under cyclic loading process | Rock salt | Deviatoric cyclic test | damage |
| Wang W. et al. | 2016 | Study on Mechanical Features of Brazilian Splitting Fatigue Tests of Salt Rock | Tensile fatigue strength is lso important for storage in salt caverns. | Rock salt | Tension cyclic test | Fatigue |
| Jiang D. et al. | 2016 | A mechanism of fatigue in salt under discontinuous cycle loading | Intervals of constant pressure in storage in salt caverns contribute with inelastic deformation, shortening the fatigue life. | Rock salt | Deviatoric cyclic test | Fatigue |
| Fan J. et al. | 2017 | Fatigue properties of rock salt subjected to interval cyclic pressure | Intervals of constant pressure in storage in salt caverns contribute with inelastic deformation, shortening the fatigue life. Residual stress and Bauschinger effect are the reason for decreasing fatigue life. | Rock salt | Deviatoric cyclic test | Fatigue |
| Voznesenskii et al. | 2017 | Features of interrelations between acoustic quality factor and strength of rock salt during fatigue cyclic loadings | The acoustic quality factor Q is a sign of strength in a non-destructive way. For certain loading rock salt have strain hardening. Salt cavern study. | Rock salt | Deviatoric cyclic test | Fatigue |

Table A.3: Publication database on Cyclic loading experiments in rocks and cement samples. Part III

| Authors | year | Title | Learning outcome | Rock | Type of cyclic test | Main objetive |
|---|---|---|---|---|---|---|
| Fan J. et al. | 2016 | Discontinuous cyclic loading tests of salt with acoustic emission monitoring | Salt cavern study. AE events allow to track the origin of damage micro-fracture initiation and propagation, sliding of the walls of micro-cracks and dislocations. | Rock salt | Deviatoric cyclic test | Fatigue |
| Chen J. et al. | 2016 | The mechanical properties of rock salt under cyclic loading-unloading experiments | Salt cavern study. It was develop a model for damage evolution versus confining pressure. This is the sa,e research group of Fan J. and Jiang D.. | Rock salt | Deviatoric cyclic test | damage |
| Bauer S. et al. | 2010 | Experimental Deformation of Salt in Cyclic Loading. Report Number SAND2010-1805C | mean and amplitue stresses far from failure also lead to fatigue The change from compaction to dilation indicate the failure. Moisture content affects results, wall of salt caverns could be wetted. | Rock salt | Deviatoric cyclic test | Fatigue |
| Liang W. | 2011 | Experiments on mechanical properties of salt rocks under cyclic loading | Salt cavern study. Thenardite, glauberite and gypsum show more fatigue than Halite. Halite behave in a ductile manner during cyclic loading while elastoplastic behavior is seen in monotonic tests. | Rock salt | Deviatoric cyclic test | Fatigue |
| Yang H. | 2013 | The influence of cyclic loading on deformation of rock salt | Salt cavern study. Elastic behavior is seen during uploading and unloading at high confining pressures. | Rock salt | Deviatoric cyclic test | Fatigue |
| Zhao B. | 2017 | Mechanical Behavior of Shale Rock under Uniaxial Cyclic Loading and Unloading Condition | Shale are prone to experience creep. This article introduce a viscoelastic plus plastic deformation as a function of damage. Calculation of energy:accumulated and dissipated | Shale | Deviatoric cyclic test | ViscoElasticPlastic properties variation |
| Li C. | 2020 | Experimental investigation of anisotropic fatigue characteristics of shale under uniaxial cyclic loading | yo aprendi | Shale | Deviatoric cyclic test | Fatigue |
| Rassouli F. | 2015 | Comparison of Short□Term and Long□Term Creep Experiments in Shales and Carbonates from Unconventional Gas Reservoirs | Short term results allow forecast of long term behavior. Shale anysotropy is important. No comment on strain rate. Good explanation of elastic,plastic and viscoplastic (creep). | Shale | Deviatoric cyclic test | ViscoElasticPlastic properties variation |
| Attewell et al. | 1973 | Fatigue behaviour of rock | Dolomite sensitive to frequency."Elapsed time devoted to stress reversal, rather than the actual number of stress reversals, is the significant parameter to accompany the applied stress in determining the fatigue strength of rock" | dolomite | Deviatoric cyclic test | Fatigue |
| Royer-Carfagni | 2000 | Characterization of marble by cyclic compression loading: experimental results | Grain detachment and microcraking are part of damage, being the former very important for Marbles | Marble | Deviatoric cyclic test | Damage |
| Lavrov | 2001 | Kaiser effect observation in brittle rock cyclically loaded with different loading rates | Kaisser effect can be used to understand the previous stress stage of a rock. Nevertheless, some condition related with displacement rate must be met. | Limestone | Tension cyclic test | Kaisser effect |
| Yang et al. | 2018 | Fatigue Characteristics of Limestone under Triaxial Compression with Cyclic Loading | Method for calculation of dissipated energy based on strains. Various definitions of damage. | Limestone | Tension cyclic test | Fatigue |
| Li et al. | 2019a | Damage precursor of construction rocks under uniaxial cyclic loading tests analyzed by acoustic emission | Indicators based on acoustic emissions could be used for fatigue forecast | Marble | Deviatoric cyclic test | Damage-Acoustic Emissions |
| Fu et al. | 2020 | Experimental and numerical investigations on crack development and mechanical behavior of marble under uniaxial cyclic loading compression | Cyclic loading affects threshold of crack closure, crack initiation and crack damage. These thresholds are explain in the paper. From Young modulus first strengthening followed by damage | Marble | Deviatoric cyclic test | Crack propagation |
| Cardani G. et al. | 2004 | Marble behaviour under monotonic and cyclic loading in tension | Damage test can be used to capture plastic strains experienced during monotonic tests | Marble | Tension cyclic test | Damage |
| Cattaneo S. et al. | 2001 | Damage of Marble from Cyclic Loading | Failure surface difference between monotonic and cyclic test were found. The latter shows powder that reveals de-cohesion process. | Marble | Tension cyclic test | Damage |
| Voznesenski A. et al. | 2015 | Predicting fatigue strength of rocks by its interrelation with the acoustic quality factor | Correlation of acoustic quality factor and residual rock strength were obtained. | Limestone | Deviatoric cyclic test | Fatigue |
| Yang S. et al. | 2017 | Experimental Investigation on Deformation Failure Characteristics of Crystalline Marble Under Triaxial Cyclic Loading | Captured the variation of Young modules before and after failure. The cycles were based on strain changes and not stress changes. Depending of the confining pressure post failure behavior can be strain softening or hardening | Marble | Deviatoric cyclic test | Fatigue |
| Yang S. et al. | 2014 | Evaluation of creep mechanical behavior of deep-buried marble under triaxial cyclic loading | It is possible to visco-elasto-plastic Burger model for reproducing stress-strain data until from damge cyclic test. Definition of elastic and plastic young modulus. | Marble | Deviatoric cyclic test | ViscoElasticPlastic properties variation |

Table A.4: Publication database on Cyclic loading experiments in rocks and cement samples. Part IV

| Authors | year | Title | Learning outcome | Rock | Type of cyclic test | Main objetive |
|---|---|---|---|---|---|---|
| Ji Y. | 2021 | Cyclic Water Injection Potentially Mitigates Seismic Risks by Promoting Slow and Stable Slip of a Natural Fracture in Granite | Pressure cycling during fracking fractured and faulted rocks could mitigate the seismic response. This is caused by transient pressure distribution. | Fault | Cycle pressure loading | Mitigation of injection-induced seismicity |
| Ji Y. | 2021 | Mitigation of injection-induced seismicity on undrained faults in granite using cyclic fluid injection: A laboratory study | Maximum injection pressure and frequency are influencing factor on the seismic response during stimulation of fractures and faults. | Fault | Cycle pressure loading | Mitigation of injection-induced seismicity |
| Arash S. | 2014 | HPHT cement sheath integrity evaluation method for unconventional wells | Tubular cement samples were used to evaluate the expansion and contraction experimented by the well cement sheath during storage. Even for the smallest delta pressure evaluated, the sample reached fatigue in a number of cycles lower than 20. | Well cement Sheath | Tension cyclic test | Fatigue |
| He Te | 2021 | Fatigue Damage of Wellbore Cement Sheath in Gas Storage Salt Cavern Under Alternating Internal Pressure | Damage was included in constitutive models implemented in ANSYS and was tuned using experimental results from Uniaxial cyclic tests. | Well cement Sheath | Tension cyclic test | Fatigue |
| Li J | 2021 | Deformation and damage of cement sheath in gas storage wells under cyclic loading | It was possible to reproduce the casing-cement-rock formation configuration."microcracks and micropores caused damage and led to axial cracking and isolation failure" | Well cement Sheath | Deviatoric cyclic test | Damage |
| Li X. | 2019 | Effect of Cyclic Loading on Cement Sheath During Staged Fracturing | Nuclear magnetic resonance was used to study the cement plugs. No major damage was observed under the tested deviatoric stress. | Well cement Sheath | Deviatoric cyclic test | Fatigue |

Table A.5: Publication database on Cyclic loading experiments in rocks and cement samples. Part V

# B

# Appendix

Next, it will be presented in detail the variables used to calculate the plastic multipliers in equations 5.27 and 5.28 for the hardening-softening plastic model. The nomenclature is from Vermeer and de Borst, 1984 will be used.

The stress-strain rate elastic relationship is expressed in matrix and abbreviated forms as follow:

$$\begin{pmatrix} \dot{\sigma_{1,1}} \\ \dot{\sigma_{2,2}} \\ \dot{\sigma_{1,2}} \\ \dot{\sigma_{3,3}} \end{pmatrix} = \begin{pmatrix} \lambda+2\mu & \lambda & \lambda & 0 \\ \lambda & \lambda+2\mu & \lambda & 0 \\ 0 & 0 & 0 & \mu \\ \lambda & \lambda & \lambda+2\mu & 0 \end{pmatrix} \begin{pmatrix} \dot{\epsilon_{1,1}} \\ \dot{\epsilon_{2,2}} \\ \dot{\epsilon_{1,2}} \\ \dot{\epsilon_{3,3}} \end{pmatrix} \tag{B.1}$$

$$\dot{\sigma} = D\dot{\epsilon}^{elastic} \tag{B.2}$$

The variation of the yield and potential flow surfaces with respect to stress are vectors:

$$\frac{\delta f_1}{\delta \sigma}^T = [-\frac{1}{2} + \frac{1}{2}sin(\phi^*_{friction}), 0, 0, \frac{1}{2} + \frac{1}{2}sin(\phi^*_{friction})] \tag{B.3}$$

$$\frac{\delta f_2}{\delta \sigma}^T = [-\frac{1}{2} + \frac{1}{2}sin(\phi^*_{friction}), \frac{1}{2} + \frac{1}{2}sin(\phi^*_{friction}), 0, 0] \tag{B.4}$$

$$\frac{\delta g_1}{\delta \sigma}^T = [-\frac{1}{2} + \frac{1}{2}sin(\psi^*), 0, 0, \frac{1}{2} + \frac{1}{2}sin(\psi^*)] \tag{B.5}$$

$$\frac{\delta g_2}{\delta \sigma}^T = [-\frac{1}{2} + \frac{1}{2}sin(\psi^*), \frac{1}{2} + \frac{1}{2}sin(\psi^*), 0, 0] \tag{B.6}$$

The variation of the yield surfaces with respect to the hardening parameter '$\bar{\epsilon}^{plastic}$' are:

$$\frac{\delta f_1}{\delta \bar{\epsilon}^{plastic}} = \frac{\delta f_1}{\delta \phi^*_{friction}} \frac{\delta \phi^*_{friction}}{\delta \bar{\epsilon}^{plastic}} + \frac{\delta f_1}{\delta c^*} \frac{\delta c^*}{\delta \bar{\epsilon}^{plastic}} \tag{B.7}$$

Where:

$$\frac{\delta f_1}{\delta \phi^*_{friction}} = \frac{1}{2}(\sigma_3 + \sigma_1)cos(\phi^*_{friction}) + c^* sin(\phi^*_{friction}) \tag{B.8}$$

$$\frac{\delta f_1}{\delta c^*} = -cos(\phi^*_{friction}) \tag{B.9}$$

$$\frac{\delta \phi^*_{friction}}{\delta \bar{\epsilon}^{plastic}} = \frac{\epsilon^f * (\epsilon^f - \bar{\epsilon}^{plastic}) sin(\phi_{friction})}{(\epsilon^f \bar{\epsilon}^{plastic})^{0.5} (\epsilon^f + \bar{\epsilon}^{plastic})^2 \sqrt{1 - \frac{4\epsilon^f \bar{\epsilon}^{plastic} sin(\phi_{friction})^2}{(\epsilon^f + \bar{\epsilon}^{plastic})^2}}} ; \text{for } \bar{\epsilon}^{plastic} > 0 \tag{B.10}$$

$$\frac{\delta c^*}{\delta \bar{\epsilon}^{plastic}} = -\frac{2c\bar{\epsilon}^{plastic} \exp -\left(\frac{\bar{\epsilon}^{plastic}}{\epsilon^c}\right)^2}{\epsilon^c} \tag{B.11}$$

Finally, the variation of the hardening parameter with respect to the plastic strains was devised as:

$$\frac{\bar{\epsilon}^{plastic}}{\delta \epsilon^{plastic}} = (\sqrt{\frac{2}{3}}, \sqrt{\frac{2}{3}}, 0, \sqrt{\frac{2}{3}}) \tag{B.12}$$

# C

# Appendix

```
## Constant amplitude cyclic model for porous rocks
## Nishihara model,  Edgar Hernandez June, 2022
#Cyclic test S2_F1_A1
import numpy as np
import matplotlib.pyplot as plt

#### Introduce input parameters for viscoelastic model
E1 = 45                          # Young's modulus [GPa]
E2 = 48                          # Young's modulus [GPa]
n1 = 2500                         # Rock viscoelastic viscosity [GPa.s] from␣
 ↪multi-step creep test
E=(E1*E2)/(E1+E2)*1000   #22000   ## [MPa] Average Young modulus of viscoelastic␣
 ↪unit

#### Introduce input parameters for brittle creep model  (Bingham unit)
Brittle_yield_point= 67.5         # [MPa] Deviatoric Brittle Yield point␣
 ↪(S1_brittle - S3)
n2= 1823253                       # [GPa.sec] from multi-step creep test

## Deviatoric stress [Time[sec],Stress[Gpa]]
Stress = np.array([[0.00000000e+00,0.00000000e+00],
 [5.00000000e+00,1.09000000e-03],
 [1.60000000e+02,1.03659129e-02],
 [3.10000000e+02, 2.26000000e-02],
 [3.18000000e+02, 2.26000000e-02],
 [4.78000000e+02, 7.86000000e-03],
 [5.78000000e+02, 7.86000000e-03],
 [5.79000000e+02, 8.50000000e-03],
 [5.86600000e+02, 1.64000000e-02],
 [5.90400000e+02, 2.03500000e-02],
 [5.98000000e+02, 2.82500000e-02],
 [6.01800000e+02, 3.22000000e-02],
 [6.09400000e+02, 4.01000000e-02],
 [6.13200000e+02, 4.40500000e-02],
 [6.17000000e+02, 4.80000000e-02],
 [6.20600000e+02, 4.40500000e-02],
 [6.27800000e+02, 3.61500000e-02],
```

Figure C.1: Viscoelastic and creep python code based on Nishihara's model part a

```
 [6.31400000e+02, 3.22000000e-02],
 [6.38600000e+02, 2.43000000e-02],
 [6.42200000e+02, 2.03500000e-02],
 [6.49400000e+02, 1.24500000e-02],
 [6.53000000e+02, 8.50000000e-03]])

strain_viscoelastic=np.zeros(len(Stress[:,0]))                    # Viscoelastic␣
 ↪axial strain vector
strain_creep=np.zeros(len(Stress[:,0]))                           # Creep axial␣
 ↪strain vector

## Viscoelastic and Linear creep module
pseudoBrittle_yield_point=Brittle_yield_point
n=n1
### Superposition of solutions "Boltzmann"
for i in range(1,len(Stress[:,0])):
    for j in range(i,len(Stress[:,0])): # Viscoelastic loop
        ␣
 ↪strain_viscoelastic[j]=strain_viscoelastic[j]+(Stress[i,1]-Stress[i-1,1])*(1/
 ↪E1+\
        1/E2*(1-np.exp(-E2/n*(Stress[j,0]-Stress[i-1,0])))) # viscoelastic loop
        if Stress[i,1] >= Brittle_yield_point/1000:   # Creep loop, divided by␣
 ↪1000 to transform to GPa
            if Stress[i-1,1] < Brittle_yield_point/1000:
                referential_stress=Brittle_yield_point/1000

            else:
                referential_stress=Stress[i-1,1]
            strain_creep[j]=strain_creep[j]+(Stress[i,1]-referential_stress)\
            *(Stress[j,0]-Stress[i-1,0])/n2
        if Stress[i-1,1] >= Brittle_yield_point/1000: # To account for the last␣
 ↪step of every cycle
            if Stress[i,1] < Brittle_yield_point/1000:
                strain_creep[j]=strain_creep[j]+\
                (Brittle_yield_point/
 ↪1000-Stress[i-1,1])*(Stress[j,0]-Stress[i-1,0])/n2

Strain = strain_viscoelastic + strain_creep

# Boundary stress condition
plt.figure(1000)
plt.plot(Stress[:,0],Strain*100,label='Axial strain')
plt.xlabel('Time(sec)',fontsize=12)
plt.ylabel('$\epsilon_1$ [%]',fontsize=12)
plt.show
```

Figure C.2: Viscoelastic and creep python code based on Nishihara's model part b

# D

# Appendix

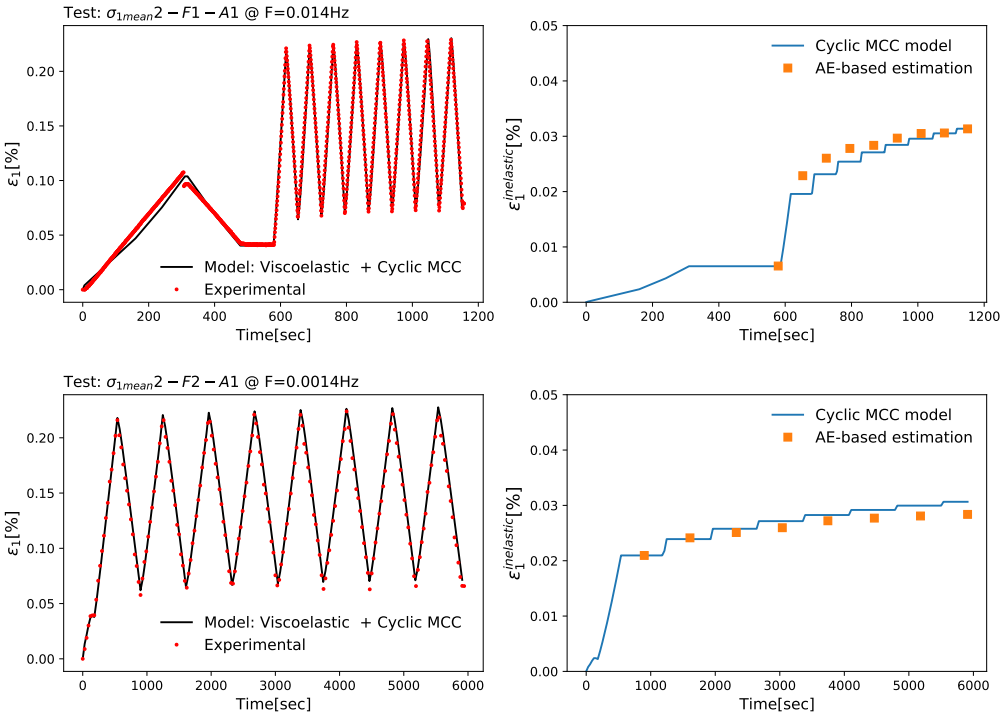


Figure D.1: Model versus experimental result for test in the elastic regime and amplitude of 20 MPa (left). Evolution of inelastic axial strain versus estimated inelastic strain from acoustic emissions 'AE' (right). Test: $\sigma_{1mean}2 - F1 - A1$ (top) and $\sigma_{1mean}2 - F2 - A1$ (bottom)

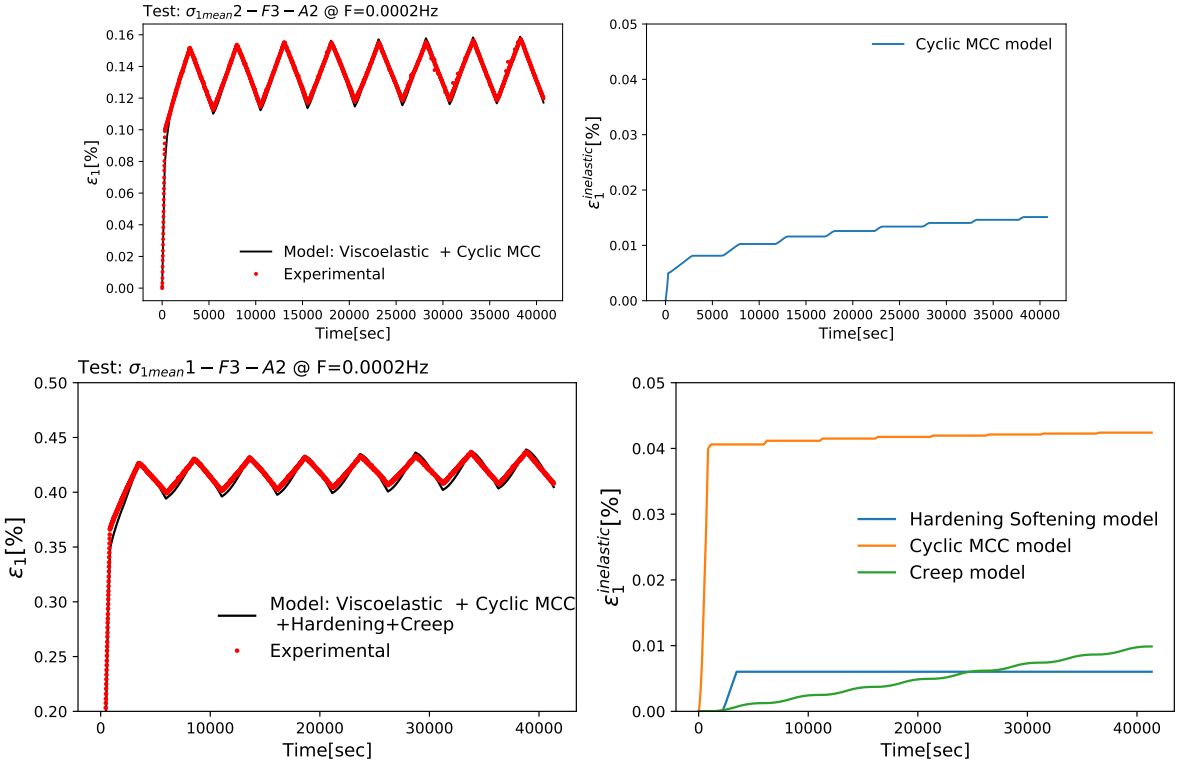


Figure D.2: Model versus experimental result for tests with amplitude of 5.11 MPa and frequency of 0.0002Hz (left). Contribution of inelastic mechanisms (right). Tests: $\sigma_{2mean}2-F3-A2$ (top) and $\sigma_{1mean}2-F3-A2$ (bottom)

# Bibliography


Allen, R., Doherty, T., Erickson, R., & Wiles, L. (1983). Factors affecting storage of caes in porous media. *U.S. Department of Energy - Pacific Northwest Laboratory, Report Number PNL-4707*. https://www.osti.gov/servlets/purl/6270908

Attewell, P. B., & Farmer, I. W. (1973). *Fatigue behaviour of rock*. Pergamon Press.

B. van der Pluijm. (2004). *Earth structure:an introduction to structural geology and tectonics* (2nd ed.). W. W. Norton Company, Inc.

Bauer, S. J., Broome, S. T., & Bronowski, D. (2010). Experimental deformation of salt in cyclic loading. *Sandia National Laboratories,Report Number SAND2010-1805C*. https://www.osti.gov/servlets/purl/1124284

Bedford, J. D., Faulkner, D. R., Leclère, H., & Wheeler, J. (2018). High-resolution mapping of yield curve shape and evolution for porous rock: The effect of inelastic compaction on porous bassanite. *Journal of Geophysical Research: Solid Earth*, *123*, 1217–1234. https://doi.org/10.1002/2017JB015250

Benetatos, C., Codegone, G., Ferraro, C., Mantegazzi, A., Rocca, V., Tango, G., & Trillo, F. (2020). Multidisciplinary analysis of ground movements: An underground gas storage case study. *Remote Sensing*, *12*, 1–19. https://doi.org/10.3390/rs12213487

Brantut, N., Heap, M. J., Baud, P., & Meredith, P. G. (2014). Rate- and strain-dependent brittle deformation of rocks. *Journal of Geophysical Research: Solid Earth*, *119*, 1818–1836. https://doi.org/10.1002/2013JB010448

Brantut, N., Heap, M. J., Meredith, P. G., & Baud, P. (2013). Time-dependent cracking and brittle creep in crustal rocks: A review. *Journal of Structural Geology*, *52*, 17–43. https://doi.org/10.1016/j.jsg.2013.03.007

Burdine, N. (1963). Rock failure under dynamic loading conditions. *Society of Petroleum Engineers, SPE-481*. https://onepetro.org/spejournal/article/3/01/1/160502/Rock-Failure-Under-Dynamic-Loading-Conditions

Carter, J. P., Booker, J., & Wroth, C. (1979). *A critical state model for cyclic loading*. Department of Civil Engineering, University of Queensland. https://espace.library.uq.edu.au/view/UQ:278783

Cerfontaine, B., Charlier, R., Collin, F., & Taiebat, M. (2017). Validation of a new elastoplastic constitutive model dedicated to the cyclic behaviour of brittle rock materials. *Rock Mechanics and Rock Engineering*, *50*, 2677–2694. https://doi.org/10.1007/s00603-017-1258-3

Cerfontaine, B., & Collin, F. (2018). Cyclic and fatigue behaviour of rock materials: Review, interpretation and research perspectives. *Rock Mechanics and Rock Engineering*, *51*, 391–414. https://doi.org/10.1007/s00603-017-1337-5

Chen, W., & McCarron, W. (1983). Modeling of soils and rocks based on concepts of plasticity. *Recent developments in laboratory and field tests and analysis of geotechnical problems*, 467–510.

Chen, Z., Li, X., Huang, X., & Jin, Z. (2022). A method for estimating the rheological properties of fractured rock inside a shear zone. *Pure and Applied Geophysics*. https://doi.org/10.1007/s00024-022-03007-x

de Borst, R. (1987). Integration of plasticity equations for singular yield functions. *Computes Structures*, *26*, 823, 829.

Dietl, C., Baumgartner, H., & Jahns, E. (2019). Poroelasticity of a porous underground gas storage system: Is there material fatigue? *DGMK/ÖGEW Spring Conference 2019 ISBN 978-3-941721-96-8*.

Dietl, C., Braun, R., Baumgartner, H., & Rudolph, E. J. T. (2018). Complex petrophysical studies to evaluate the safety of an underground gas storage in porous rocks. *AAPG Search and Discovery article 80642*. https://www.searchanddiscovery.com/documents/2018/80642dietl/ndx_dietl.pdf

Eradus, D. (2019). *Petrographical description and petrophysical measurements on the red felser sandstone* (Doctoral dissertation). TU Delft.

Fenix-Consulting-Delft-BV. (2018). 3d geomechanical model for gas storage bergermeer. *report for TAQA Energy BV*. https://nl.taqa.com/wp-content/uploads/sites/23/2021/04/PDF-19-3D-Geomechanical-Model-GSB-77-133-bar.pdf

Fuenkajorn, K., & Phueakphum, D. (2010). *Effects of cyclic loading on mechanical properties of maha sarakham salt* (2).

Gallo, A., Simões-Moreira, J., Costa, H., Santos, M., & Moutinho, E. (2016). A review of geothermal energy-driven hydrogen production systems. *Renewable and Sustainable Energy Reviews*. https://doi.org/10.1016/j.rser.2016.07.028

Gatelier, N., Pellet, F., & Loret, B. (2002). *Mechanical damage of an anisotropic porous rock in cyclic triaxial tests*.

Guo, Y., Yang, C., & Mao, H. (2012). Mechanical properties of jintan mine rock salt under complex stress paths. *International Journal of Rock Mechanics and Mining Sciences*, *56*, 54–61. https://doi.org/10.1016/j.ijrmms.2012.07.025

Haghighat, E., Rassouli, F. S., Zoback, M. D., & Juanes, R. (2020). A viscoplastic model of creep in shale. *Geophysics*, *85*, MR155–MR166. https://doi.org/10.1190/geo2018-0700.1

Haihong, T. Z. M. (1990). An experimental study and analysis of the behaviour of rock under cyclic loading. *International Journal of Rock Mechanics and Mining Sciences*, *27*, 51–56.

He, T., Wang, T., Shan, B., An, G., Yang, J., & Daemen, J. J. (2021). Fatigue damage of wellbore cement sheath in gas storage salt cavern under alternating internal pressure. *Rock Mechanics and Rock Engineering*. https://doi.org/10.1007/s00603-021-02686-7

Heap, M. J., & Faulkner, D. R. (2008). Quantifying the evolution of static elastic properties as crystalline rock approaches failure. *International Journal of Rock Mechanics and Mining Sciences*, *45*, 564–573. https://doi.org/10.1016/j.ijrmms.2007.07.018

Heinemann, N., Alcalde, J., Miocic, J., Hangx, S., Kallmayer, J., Ostertag-Henning, C., Hassanpouryouzband, A., Thaysen, E., Strobel, G., Schmidt, C., Edlmann, K., Wilkinson, M., Bentham, M., Haszeldine, S., Carbonell, R., & Rudloff, A. (2021). Enabling large-scale hydrogen storage in porous media – the scientific challenges. *Energy Environmental Science*, *14*, 853. https://doi.org/10.1039/d0ee03536j

Hemme, C., & van Berk, W. (2017). Potential risk of h2s generation and release in salt cavern gas storage. *Journal of Natural Gas Science and Engineering*, *47*, 114–123. https://doi.org/10.1016/j.jngse.2017.09.007

Ji, Y., Yoon, J. S., Zang, A., & Wu, W. (2021). Mitigation of injection-induced seismicity on undrained faults in granite using cyclic fluid injection: A laboratory study. *International Journal of Rock Mechanics and Mining Sciences*, *146*. https://doi.org/10.1016/j.ijrmms.2021.104881

Ji, Y., Zhuang, L., Wu, W., Hofmann, H., Zang, A., & Zimmermann, G. (2021). Cyclic water injection potentially mitigates seismic risks by promoting slow and stable slip of a natural fracture in granite. *Rock Mechanics and Rock Engineering*, *54*, 5389–5405. https://doi.org/10.1007/s00603-021-02438-7

Jiang, D., Fan, J., Chen, J., Li, L., & Cui, Y. (2016). A mechanism of fatigue in salt under discontinuous cycle loading. *International Journal of Rock Mechanics and Mining Sciences*, *86*, 255–260. https://doi.org/10.1016/j.ijrmms.2016.05.004

K. de-Kloe, J. D., A. van-der-Linden. (2008). Cyclic compaction experiments on samples from norg-5. *Shell, report EP2008-5189*. https://www.rvo.nl/sites/default/files/2020/02/Gasopslag-Norg-UGS-fault-reactivation-study-and-implications-for-seismic-threat.pdf

Kabuth, A., Dahmke, A., Beyer, C., Bilke, L., Dethlefsen, F., Duttmann, R., Ebbert, M., Feeser, V., Gorke, U., Kober, R., W., R., Schanz, T., Shafer, D., Wurdermann, H., & Bauer, S. (2017). Energy storage in the geological subsurface: Dimensioning, risk analysis and spatial planning: The angus+ project. *Environmental Earth Sciences*, *76*. https://doi.org/10.1007/s12665-016-6319-5

Kelly, P. (2013). *Solid mechanics lecture notes - an introduction to solid mechanics*. University of Auckland.

Kumar, K. R., & Hajibeygi, H. (2021). Multiscale simulation of inelastic creep deformation for geological rocks. *Journal of Computational Physics*, *440*. https://doi.org/10.1016/j.jcp.2021.110439

Lavrov, A. (2001). Kaiser eff□ect observation in brittle rock cyclically loaded with di□erent loading rates. *Mechanics of Materials*, *33*, 669–677. https://doi.org/10.1016/S0167-6636(01)00081-3

Le, J. L., Manning, J., & Labuz, J. F. (2014). Scaling of fatigue crack growth in rock. *International Journal of Rock Mechanics and Mining Sciences*, *72*, 71–79. https://doi.org/10.1016/j.ijrmms.2014.08.015

LI, J., ZHAO, G., QI, Z., YIN, B., XU, X., FANG, F., YANG, S., & QI, G. (2021). Stress sensitivity of formation during multi-cycle gas injection and production in an underground gas storage rebuilt from gas reservoirs. *Petroleum Exploration and Development*, *48*, 968–977. https://doi.org/10.1016/S1876-3804(21)60081-2

Li, J., Su, D., Tang, S., Li, Z., Wu, H., Huang, S., & Sun, J. (2021). Deformation and damage of cement sheath in gas storage wells under cyclic loading. *Energy Science and Engineering*, *9*, 483–501. https://doi.org/10.1002/ese3.869

Li, X., & Yin, Z. (2021). Study of creep mechanical properties and a rheological model of sandstone under disturbance loads. *Processes*, *9*. https://doi.org/10.3390/pr9081291

Liang, W., Zhang, C., Gao, H., Yang, X., Xu, S., & Zhao, Y. (2012). Experiments on mechanical properties of salt rocks under cyclic loading. *Journal of Rock Mechanics and Geotechnical Engineering*, *4*, 54–61. https://doi.org/10.3724/sp.j.1235.2012.00054

Liu, Y., & Dai, F. (2021). *A review of experimental and theoretical research on the deformation and failure behavior of rocks subjected to cyclic loading*. https://doi.org/10.1016/j.jrmge.2021.03.012

Lockner, D. (1993). The role of acoustic emission in the study of rock fracture. *International Journal of Rock Mechanics and Mining Sciences  Geomechanics Abstracts*, *30*(7), 883–899. https://doi.org/https://doi.org/10.1016/0148-9062(93)90041-B

Ma, H. L., Yang, C. H., Liu, J. F., & Chen, J. W. (2013a). The influence of cyclic loading on deformation of rock salt. *Rock Characterisation, Modelling and Engineering Design Methods - Proceedings of the 3rd ISRM SINOROCK 2013 Symposium*, 63–68. https://doi.org/10.1201/b14917-10

Ma, H. L., Yang, C. H., Liu, J. F., & Chen, J. W. (2013b). *The Influence of Cyclic Loading on Deformation of Rock Salt* (Vol. All Days) [ISRM-SINOROCK-2013-007].

Mahmoud, M., Ramadan, M., Naher, S., Pullen, K., & et al. (2021). A review of geothermal energy-driven hydrogen production systems. *Thermal Science and Engineering Progress*. https://doi.org/10.1016/j.tsep.2021.100854

Matos, C., Carneiro, J., & Silva, P. (2018). Overview of large-scale underground energy storage technologies for integration of renewable energies and criteria for reservoir identification. *Journal of Energy Storage*. https://doi.org/10.1016/j.est.2018.11.023

Muntendam-Bos, A., Wassing, B., Geel, C., Louh, M., & van Thienen-Visser, K. (2008). *Bergermeer seismicity study*.

N.A.M. (2016). Norg ugs fault reactivation study and implications for seismic threat. *NEDERLANDSE AARDOLIE MAATSCHAPPIJ B.V. ASSEN, Report Number EP201610208045*. https://www.rvo.nl/sites/default/files/2020/02/Gasopslag-Norg-UGS-fault-reactivation-study-and-implications-for-seismic-threat.pdf

Nejati, H. R., & Ghazvinian, A. (2014). Brittleness effect on rock fatigue damage evolution. *Rock Mechanics and Rock Engineering*, *47*, 1839–1848. https://doi.org/10.1007/s00603-013-0486-4

Orlic, B., Wassing, B., & Geel, C. (2013). Field scale geomechanical modeling for prediction of fault stability during underground gas storage operations in a depleted gas field in the netherlands. *American Rock Mechanics Association*, (ARMA-13-300). https://doi.org/10.1007/s12665-016-6319-5

Peng, K., Zhou, J., Zou, Q., Zhang, J., & Wu, F. (2019a). Effects of stress lower limit during cyclic loading and unloading on deformation characteristics of sandstones. *Construction and Building Materials*, *217*, 202–215. https://doi.org/10.1016/j.conbuildmat.2019.04.183

Peng, K., Zhou, J., Zou, Q., Zhang, J., & Wu, F. (2019b). Effects of stress lower limit during cyclic loading and unloading on deformation characteristics of sandstones. *Construction and Building Materials*, *217*, 202–215. https://doi.org/https://doi.org/10.1016/j.conbuildmat.2019.04.183

Pijnenburg, R. P., Verberne, B. A., Hangx, S. J., & Spiers, C. J. (2018). Deformation behavior of sandstones from the seismogenic groningen gas field: Role of inelastic versus elastic mechanisms. *Journal of Geophysical Research: Solid Earth*, *123*, 5532–5558. https://doi.org/10.1029/2018JB015673

Pijnenburg, R. P., Verberne, B. A., Hangx, S. J., & Spiers, C. J. (2019). Inelastic deformation of the slochteren sandstone: Stress-strain relations and implications for induced seismicity in the

groningen gas field. *Journal of Geophysical Research: Solid Earth*, *124*, 5254–5282. https://doi.org/10.1029/2019JB017366

Pijnenburg, R. P., & Spiers, C. J. (2020). Microphysics of inelastic deformation in reservoir sandstones from the seismogenic center of the groningen gas field. *Rock Mechanics and Rock Engineering*, *53*, 5301–5328. https://doi.org/10.1007/s00603-020-02215-y

Prinzhofer, A., Cissé, C. S. T., & Diallo, A. B. (2018). Discovery of a large accumulation of natural hydrogen in bourakebougou (mali). *International Journal of Hydrogen Energy*, *43*, 19315–19326. https://doi.org/10.1016/j.ijhydene.2018.08.193

R. Weijermars. (1997). *Principles of rock mechanics* (6th ed.). Alboran Science Pub.

Rassouli, F., & Zoback, M. (2015). 2015 long-term creep experiments on haynesville shale rocks. *ARMA - Number 15-532*.

Ray, S. K., Sarkar, M., & Singh, T. N. (1999). Effect of cyclic loading and strain rate on the mechanical behaviour of sandstone. *International Journal of Rock Mechanics and Mining Sciences*, *36*, 543–549. https://doi.org/10.1016/S0148-9062(99)00016-9

Rohde, R. (n.d.). *MS Windows NT kernel description*. https://commons.wikimedia.org/wiki/File:Ice_Age_Temperature.png#filelinks

Roscoe, K., & Burland, J. (1968). On the generalized stress-strain behavior of wet clays.

Royer-Carfagni, G., & Salvatore, W. (2000). Characterization of marble by cyclic compression loading: Experimental results. *Mech. Cohes.-Frict. Mater*, *5*, 535–563. https://doi.org/10.1002/1099-1484(200010)5:7<535::AID-CFM102>3.0.CO;2-D

Shadravan, A., Schubert, J., Amani, M., & Teodoriu, C. (2015). Using fatigue-failure envelope for cement-sheath-integrity evaluation. *SPE Drilling and Completion*, *30*, 68–75. https://doi.org/10.2118/168321-PA

Shuguang Song, Y. C. (2021). *Encyclopedia of geology* (Second, Vol. 2). Academic Press.

Silverii, F., Maccaferri, F., Richter, G., Cansado, B. G., Wang, R., Hainzl1, S., & Dahm, T. (2021). Poroelastic model in a vertically sealed gas storage: A case study from cyclic injection/production in a carbonate aquifer. *Geophysical Journal International*, *227*. https://doi.org/10.1093/gji/ggab268

Song, R., Yue-ming, B., Jing-Peng, Z., De-yi, J., & Chun-he, Y. (2013). Experimental investigation of the fatigue properties of salt rock. *International Journal of Rock Mechanics and Mining Sciences*, *64*, 68–72. https://doi.org/10.1016/j.ijrmms.2013.08.023

Taheri, A., Royle, A., Yang, Z., & Zhao, Y. (2016). Study on variations of peak strength of a sandstone during cyclic loading. *Geomechanics and Geophysics for Geo-Energy and Geo-Resources*, *2*, 1–10. https://doi.org/10.1007/s40948-015-0017-8

Teatini, P., Castelletto, N., Ferronato, M., Gambolati, G., Janna, C., Cairo, E., Marzorati, D., Colombo, D., Ferretti, A., Bagliani, A., & Bottazzi, F. (2011). Geomechanical response to seasonal gas storage in depleted reservoirs: A case study in the po river basin, italy. *Journal of Geophysical Research: Earth Surface*, *116*. https://doi.org/10.1029/2010JF001793

Tek, M. (1987). *Underground gas storage of natural gas* (First). Gulf publishing company.

Vermeer, P., & de Borst, R. (1984). Non-associated plasticity for soils, concrete and rocks. *HERON*, *124*.

Wang, H. L., Xu, W. Y., Cai, M., Xiang, Z. P., & Kong, Q. (2017). Gas permeability and porosity evolution of a porous sandstone under repeated loading and unloading conditions. *Rock Mechanics and Rock Engineering*, *50*, 2071–2083. https://doi.org/10.1007/s00603-017-1215-1

Wang, X., Huang, Q., Lian, B., Liu, N., & Zhang, J. (2018). Modified nishihara rheological model considering the effect of thermal-mechanical coupling and its experimental verification. *Advances in Materials Science and Engineering*, *2018*. https://doi.org/10.1155/2018/4947561

Wichtmann, T. (2005). *Explicit accumulation model for non-cohesive soils under cyclic loading* (Doctoral dissertation). Ruhr-Universität Bochum.

Xu, T., Zhou, G., Heap, M. J., Yang, S., Konietzky, H., & Baud, P. (2018). The modeling of time-dependent deformation and fracturing of brittle rocks under varying confining and pore pressures. *Rock Mechanics and Rock Engineering*, *51*, 3241–3263. https://doi.org/10.1007/s00603-018-1491-4

Yang, S. Q., & Hu, B. (2018). Creep and long-term permeability of a red sandstone subjected to cyclic loading after thermal treatments. *Rock Mechanics and Rock Engineering*, *51*, 2981–3004. https://doi.org/10.1007/s00603-018-1528-8

Yang, Y., Duan, H., Xing, L., Ning, S., & Lv, J. (2018). Fatigue characteristics of limestone under triaxial compression with cyclic loading. *Advances in Civil Engineering*, *2018*. https://doi.org/10.1155/2018/8681529